AN EIKONAL MODEL FOR MULTIPARTICLE PRODUCTION IN HADRON-HADRON SCATTERING

By

Ivan Borozan

Department of Physics and Astronomy

November 2002

Contents

List of Figures

Abstract

UNIVERSITY COLLEGE LONDON

ABSTRACT OF THESIS submitted by **Ivan Borozan** for the Degree of Doctor of Philosophy and entitled **An Eikonal Model for Multiparticle production in Hadron-Hadron Scattering**

Month and Year of Submission: November 2002

The purpose of this thesis is the introduction of a model for multiparticle production in hadron-hadron interactions.

An introduction to the broad issue of perturbative Quantum Chromodynamics (QCD) is presented in the first chapter with special emphasis on the concepts of renormalization, asymptotic freedom and scaling violation. In addition non-perturbative concepts such as Regge theory and Regge pole parametrisation of the total cross section are mentioned.

The second chapter is a broad introduction to the Monte Carlo techniques used in event generators and numerical integrators with special emphasis on the methods used in the HERWIG event generator.

The third chapter contains a brief overview of the main physics and methods used in HERWIG for simulation of large momentum transfer collisions between two

hadrons.

In Chapter 4 we introduce the physics of the underlying event and adopt a simple jet definition used by the CDF collaboration in the analysis of charged particle component of jets simulated by HERWIG in three different topological regions. For hard scattering proton-antiproton collisions we simulate the underlying event activity in each region using HERWIG's Underlying Event model and compare it to the experimental data. We thus independently confirm results obtained by the CDF collaboration.

In Chapter 5 we present the Multiparton Interaction model used as a substitute to the HERWIG Soft Underlying event model. We examine whether the addition of secondary hard scatters to the main hard interaction improves the simulated data on the underlying event. We propose to tune the value of the proton radius used in the Hard Multiparton Interaction model in order to obtain a good agreement with the experimental data.

In Chapter 6 we introduce a new Eikonal Monte Carlo model in order to simulate multiparticle production in hadron-hadron interactions. The model contains a single phenomenological input the total cross section for $p\overline{p}$ and pp scattering. We show a broad agreement between our model predictions and experimental data. We discuss its main advantages over the two underlying event models used in chapters 4 and 5. Finally we use the new Eikonal model to predict the underlying event activity which should be expected at the LHC.

Declaration

No portion of the work referred to in this thesis has been submitted in support of an application for another degree or qualification of this or any other university or other institution of learning.

Dedication

Dedicated to the memory of

Prof. Dragoljub Mihailovic

(1917 - 1994)

"...Iko moja diko"

Acknowledgements

I would first like to express my infinite gratitude to my grand-father for his encouragement and material help without which probably nothing of my initial resolve to study physics would have been realized and to CCLRC for funding my postgraduate studies.

My big thank goes to my family for all the love you have given to me (particularly to my mother Alexandra and my sister Maria).

During these three years of my PhD I have had the opportunity to work within three different research groups, I joined the HEP group of the University College London in October 1999 and started my work under the supervision of Dr. Jon Butterworth, who has introduced me to the interesting problem of the underlying event in lepton-hadron and hadron-hadron collisions, thanks Jon for all your help and encouragement.

After my first year at University College London I have moved and joined the RAL theory particle physics group under the supervision of Dr. Michael Seymour, Mike thank you for all your help, patience, encouragement and invaluable discussions during these past three years.

My special thank goes to Dr. Jeff Forshaw for his help and useful discussions and the Manchester Theory group for their hospitality and support during the final year of my thesis.

Thank you Alberto Ribon and Kosuke Odagiri for all your help and friendship.

The Author

Ivan Borozan graduated with an MSci in physics from *University College London*. In September 1999 he started this thesis at the Department of Physics and Astronomy as a member of the High Energy Physics Group of University College London.

"It is not certain that everything is uncertain."

Blaise Pascal

Chapter 1

Introduction

1.1 Introduction

In this chapter we present a brief overview of the main concepts used in Quantum Chromo Dynamics, the theory of strong interactions. Most of the concepts presented in the following sections are implemented in the HERWIG Monte Carlo Event generator, our principal tool for data simulation. Furthermore in this thesis we will propose and use a new model with HERWIG as its kernel. Thus it is essential that the main concepts and approximations used in HERWIG (as a "faithful" representation of the perturbative QCD part) are transparent to anyone who is going to use it. What are the advantages of using a Monte Carlo event generator in our simulations ? First it is particularly suitable for describing complex final states that traditional analytical techniques are not capable of, second it is particularly convenient since we can impose on our final states the same experimental cuts as those used in the experiment. Thus a Monte Carlo event generator is an interesting tool that is particularly important if we are to estimate the accuracy of perturbative QCD predictions in this particular case, or more generally to simulate the physics of the Standard Model as a background to some new physics.

The structure of this thesis is as follows: in Chapter 2 we present an overview of the most important Monte Carlo techniques used in Monte Carlo event generators, in Chapter 3 we describe the main assumptions and approximations used in HERWIG for simulating two-to-two parton-parton scattering, in Chapter 4 we compare data simulated with HERWIG QCD Monte Carlo event generator to those of experimental proton-antiproton collisions at 1.8 TeV involving a hard scattering and focus on whether our 'default', Monte Carlo model describes correctly the 'underlying event' in hard jets. In Chapter 5 we present an overview of the Hard Multiparton interaction model and examine whether this alternative model describes better the 'underlying event'. In Chapter 6 we propose a new model for simulating the 'underlying event' based on an eikonal approach and compare it to HERWIG's default Underlying Event model and the Hard Multiparton Interaction model results. Finally we test the predictability of our model by comparing our simulated data to the experimental UA1

measurement at $\sqrt{s}$=630 GeV.

1.2   QCD

The theoretical and experimental study at high energies of hadron-hadron, lepton-lepton and lepton-hadron interactions has led to a description of properties of the strong force. The strong force is one of the four fundamental forces in nature and is responsible for nuclear binding and hadron-hadron interactions. Quantum Chromo Dynamics (QCD) is considered today as the most correct theoretical description of strong interactions.

The QCD Lagrangian is formulated in terms of its fundamental fields, quarks and gluons. Each fundamental particle of QCD carries, together with the usual quantum numbers an additional degree of freedom, named colour. Colour was introduced to explain the wave function for the doubly charged Δ^{++} baryon, having the spin of 3/2. If we are to construct a Δ^{++} wave function, using three identical quarks in their ground state, we will obtain a symmetrical wave function of space, spin and flavour $\mathrm{SU}(3)_f$ degrees of freedom. However as quarks have spin 1/2, Fermi-Dirac Statistics dictates a totally anti-symmetric wave function for the Δ^{++} baryon. By adding the colour degree of freedom (with three possible values) to quarks, the Δ^{++} baryon wave function can be made totally anti-symmetric in colour. The elementary fundamental particles of QCD cannot be observed in experiments as such, only their bound states, such as hadrons are. QCD in consequence exhibits a particular behaviour, at small distances the fundamental particles can be essentially considered as free (i.e small coupling constant) and at large distances ($\approx 1fm$) and large coupling constant, quarks and gluons form bound states. The decrease of the coupling constant at small distances is known as *asymptotic freedom* and the mechanism forcing quarks and gluons into asymptotic states is known as *confinement*. Furthermore because coloured states are not detected in experiments, one additional constraint is required, that only colour singlet states can exist in nature. The behaviour of the coupling constant at large

distances prevents perturbative QCD calculations from predicting asymptotic final states.

The idea of colour was checked in early experimental tests, for example the rate of decay $\pi^0 \to \gamma\gamma$ or the ratio of the e^+e^- hadronic total cross section to the cross section for the production of a muon pair. The evidence for the existence of approximately point-like particles was provided by the early electron deep inelastic scattering experiment at SLAC showing the scaling behaviour of the measured cross section. The point-like particles inside hadrons were termed partons and identified later with quarks and gluons.

1.2.1   QCD Lagrangian

The expression for the QCD Lagrangian density, invariant under SU(3) local gauge phase transformations, can be written as

$$\mathcal{L} = \sum_f^{n_f} \bar{\psi}_a^{(f)}(i\slashed{\mathcal{D}} - m)_{ab}\psi_b^{(f)} - \frac{1}{4}F_{\mu\nu}^a F_a^{\mu\nu} + \mathcal{L}_{\text{gauge fixing}} + \mathcal{L}_{\text{ghost}}. \tag{1.1}$$

The quark and gluon fields are represented by ψ and A respectively. $\mathcal{D}$ is the covariant derivative $(\mathcal{D}_\mu)_{ab} = \partial_\mu \delta_{ab} + ig(t^C A_\mu^C)_{ab}$ acting on triplet quark fields and $(\mathcal{D}_\mu)_{AB} = \partial_\mu \delta_{AB} + ig(T^C A_\mu^C)_{AB}$ on octet gluon fields. The flavour number, f in eq.1.1, runs over all n_f quark flavours. $F_{\mu\nu}^a$ is the field strength tensor derived from the gluon field

$$F_{\mu\nu}^A = \partial_\mu A_\nu^A - \partial_\nu A_\mu^A - gf^{ABC}A_\mu^B A_\nu^C. \tag{1.2}$$

The indices A, B, C run over $1, ..., N_c^2 - 1$ colour degrees of freedom of the gluon field and a, b, c run over the triplet representation of the colour group, f^{ABC} are the $SU(N_c)$ group structure constants, g is the coupling constant which determines the strength of the interaction between the coloured quanta and N_c is the number of colours in the theory. We mention here, without going into further details, that the choice of gauge is

necessary for defining the gluon propagator and the ghost term cancel the unphysical degrees of freedom which would otherwise propagate in the covariant gauges.

1.2.2   Renormalization

Feynman rules can be directly deduced from the Lagrangian in eq.1.1. At higher orders, divergences will appear in loop integrals, when the momentum in the loop integral goes to infinity (ultra-violet divergences) or when the outgoing partons are in the soft or collinear limit (infra-red divergences). In the case of infrared divergences the loop and soft and collinear contributions cancel each other[*], making their sum 'infrared' finite. However for loop integrals such as shown in fig.1.1, the infinite integrals need first to be regularized before the infinite (ultra-violet) divergences are absorbed. One way to regularize an infinite integral would be to introduce a momentum cutoff and then absorb the divergent term into newly redefined fields or parameters. The re-definition of the fields and parameters after absorption of the divergent term is known as *renormalization*. We give here an outline of the renormalization of the bare strong coupling g (for more details see [3]).

If we are to compute the effective strong coupling at one loop level we would get

$$g_{eff} = g_{eff}(Q^2) = g - b\frac{g^3}{32\pi}\left[\ln\frac{Q^2}{\Lambda^2}\right] + O(g^5), \tag{1.3}$$

where Λ is the ultraviolet cutoff, for $\Lambda \to \infty$, $g_{eff}(Q^2)$ is divergent (i.e. $g_{eff}(Q^2) \to \infty$). The procedure now consists of introducing a *renormalization scale* μ^2 at which the renormalized coupling (as opposed to bare) for some choice of $Q^2 = \mu^2$ will be fixed to a particular finite value. The new effective (measured) coupling $g_{eff}(Q^2)$ becomes then a function of the renormalization scale μ^2 and can be expressed as

$$g_{eff}(Q^2) = g_{eff}(\mu^2) - b\frac{g^3_{eff}(\mu^2)}{32\pi}\left[\ln\frac{Q^2}{\mu^2}\right] + O(g^5_{eff}). \tag{1.4}$$

An often used method for regularizing infinite integrals is dimensional regularization. The idea is that the loop integral is only divergent in four dimensions, for

---

[*]Initial-state collinear divergencies do not cancel but can be factorised and replaced by non-perturbative parton distribution functions

smaller number of dimensions the integral is finite. Thus by integrating in D = 4-ϵ (ϵ > 0) dimension a finite result should be found. The one-loop contributions shown in fig.1.1, contain respectively integrals of the form [1]

$$I_1 = \int \frac{d^4k}{(2\pi)^4} \frac{C}{(k^2 - m^2)((k+q)^2 - m^2)}, \tag{1.5}$$

$$I_2 = \int \frac{d^4k}{(2\pi)^4} \frac{D}{k^2(k+q)^2}, \tag{1.6}$$

$$I_3 = \int \frac{d^4k}{(2\pi)^4} \frac{E}{k^2}, \tag{1.7}$$

$$I_4 = \int \frac{d^4k}{(2\pi)^4} \frac{F}{k^2(k+q)^2}. \tag{1.8}$$

For an expression with two factors in the denominator we first introduce Feynmann parameters x and y defined as

$$\frac{1}{AB} = \int_0^1 dx \frac{1}{[xA + (1-x)B]^2} = \int_0^1 dxdy\delta(x + y - 1)\frac{1}{[xA + yB]^2}. \tag{1.9}$$

We can now express eqs.1.5-1.8 respectively as

$$I_1 = \int_0^1 dx \int d^4l \frac{1}{(2\pi)^4} \frac{C'}{(l^2 - \Delta')^2}, \tag{1.10}$$

$$I_2 = \int_0^1 dx \int d^4l \frac{1}{(2\pi)^4} \frac{D'}{(l^2 - \Delta)^2}, \tag{1.11}$$

$$I_3 = \int_0^1 dx \int d^4l \frac{1}{(2\pi)^4} \frac{E'}{(l^2 - \Delta)^2}, \tag{1.12}$$

$$I_4 = \int_0^1 dx \int d^4l \frac{1}{(2\pi)^4} \frac{F'}{(l^2 - \Delta)^2}, \tag{1.13}$$

where $l = k + xq$, $\Delta' = m^2 - x(1-x)q^2$ and $\Delta = -x(1-x)q^2$.

We perform the Wick rotation of the variable l and define the Euclidean 4-momentum variable l_E as

$$l^0 = il_E^0, \ \mathbf{l} = \mathbf{l_E}. \tag{1.14}$$

The integrals from eqs.1.10-1.13 can now be evaluated in four-dimensional spherical coordinates using the general expression

$$I = \int_0^1 dx \int d^4l_E \frac{1}{(2\pi)^4} \frac{1}{(l_E^2 + \Delta)^2}, \tag{1.15}$$
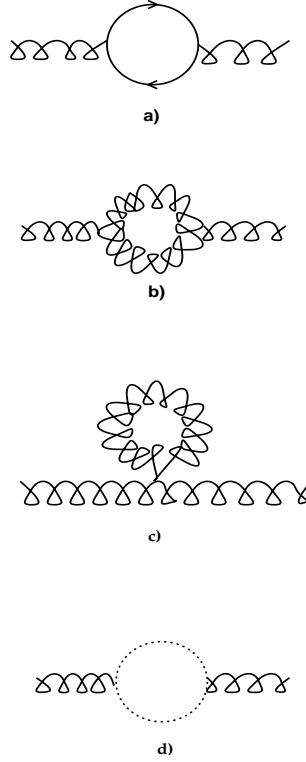
Figure 1.1: One loop Feynman diagrams.

which is badly ultraviolet divergent. This integral can however be regularized using dimensional regularization.

In d dimensions the integral in eq.1.15 can be written as [1]

$$I = \int d^d l_E \frac{1}{(2\pi)^d} \frac{1}{(l_E^2 + \Delta)^2} = \frac{1}{(4\pi)^{d/2}} \frac{\Gamma(2 - d/2)}{\Gamma(2)} \left(\frac{1}{\Delta}\right)^{2-d/2}. \qquad (1.16)$$

Defining $\epsilon = 4 - d$, near $d = 4$ we use the approximation,

$$\Gamma\left(2 - \frac{d}{2}\right) = \Gamma\left(\frac{\epsilon}{2}\right) = \frac{2}{\epsilon} + \gamma_E + O(\epsilon), \qquad (1.17)$$

where $\gamma_E \approx .5772$ is the Euler constant and the integral in eq.1.16 becomes then for $d \to 4$

$$I = \int d^d l_E \frac{1}{(2\pi)^d} \frac{1}{(l_E^2 + \Delta)^2} \to \frac{1}{(4\pi)^2} \left(\frac{2}{\epsilon} - \log \Delta - \gamma_E + \log(4\pi) + O(\epsilon)\right) \qquad (1.18)$$

The divergence in the loop integral now shows as a pole in ϵ. The pole in ϵ can be removed by adding counter terms to the Lagrangian and re-interpreting the new

terms as the renormalized fields and coupling. If the counter terms exactly cancel the ϵ pole then this defines the minimal subtraction scheme (MS). However if additional constant terms (such as $\gamma_E - \log(4\pi)$) are also removed then this defines a modified MS scheme known as $\overline{MS}$. One drawback of the dimensional regularization is that the coupling being dimensionless in d=4 acquires dimensions in d $\neq$ 4 and the subtraction scale μ is introduced and factors of μ^ϵ keep appearing.

1.2.3   Asymptotic freedom

A physical observable should not depend on the choice of the renormalization scale. This statement can be formulated as the renormalization group equation (RGE) (see for example [2]),

$$\mu^2 \frac{d}{d\mu^2}\Theta(Q^2/\mu^2,\alpha_s) \equiv \left[\mu^2\frac{\partial}{\partial\mu^2} + \mu^2\frac{\partial\alpha_s}{\partial\mu^2}\frac{\partial}{\partial\alpha_s}\right]\Theta = 0, \quad \alpha_s = \frac{g^2}{4\pi}, \qquad (1.19)$$

where $\Theta(Q^2/\mu^2,\alpha_s)$ is a dimensionless physical observable with physical scale Q^2. The expression in eq.1.19 can be rewritten as

$$\left[-\frac{\partial}{\partial t} + \beta(\alpha_s)\frac{\partial}{\partial\alpha_s}\right]\Theta(\exp(t),\alpha_s) = 0, \qquad (1.20)$$

where the variables t and $\beta(\alpha_s)$ are defined as

$$t = \ln\left(\frac{Q^2}{\mu^2}\right), \quad \beta(\alpha_s) = \mu^2\frac{\partial\alpha_s}{\partial\mu^2}. \qquad (1.21)$$

The first order differential equation in eq.1.20 can be solved by defining the running coupling $\alpha_s(Q^2)$ as

$$t = \int_{\alpha_s}^{\alpha_s(Q^2)} \frac{du}{\beta(u)}, \quad \alpha_s(\mu^2) \equiv \alpha_s. \qquad (1.22)$$

By differentiating eq.1.22 we can check that

$$\frac{\partial\alpha_s(Q^2)}{\partial t} = \beta(\alpha_s(Q^2)), \quad \frac{\partial\alpha_s(Q^2)}{\partial\alpha_s} = \frac{\beta(\alpha_s(Q^2))}{\beta(\alpha_s)}, \qquad (1.23)$$

and that $\Theta(1,\alpha_s(Q^2))$ is a solution of eq.1.20.

The running of the coupling constant α_s is thus determined by the RGE

$$Q^2\frac{\partial\alpha_s}{\partial Q^2} = \beta(\alpha_s). \qquad (1.24)$$

In QCD, $\beta(\alpha_s)$ in eq.1.20, can be expanded pertubatively [2] as

$$\beta(\alpha_s) = -b\alpha_s^2(1 + b'\alpha_s + O(\alpha_s^2)). \tag{1.25}$$

At one loop level, graphs from fig.1.1.(a,b) are used to obtain the value of b which can be expressed as [2]

$$b = \frac{11C_A - 2n_f}{12\pi} = \frac{(33 - 2n_f)}{12\pi}. \tag{1.26}$$

At higher order b' is calculated to be [2]

$$b' = \frac{(17C_A^2 - 5C_A n_f - 3C_F n_f)}{2\pi(11C_A - 2n_f)} = \frac{(153 - 19n_f)}{2\pi(33 - 2n_f)}. \tag{1.27}$$

If higher order terms to one loop level in eq.1.25 are neglected, eq.1.24 can be rewritten as

$$Q^2\frac{\partial \alpha_s(Q^2)}{\partial Q^2} = -b\alpha_s^2(Q^2), \tag{1.28}$$

which gives as solution

$$\alpha_s(Q^2) = \frac{\alpha_s(\mu^2)}{1 + \alpha_s(\mu^2)bt}, \quad t = \ln\left(\frac{Q^2}{\mu^2}\right). \tag{1.29}$$

The role of the running coupling $\alpha_s(Q^2)$ in eq.1.29 can be seen as twofold, first it compensate for the $\Theta(Q^2/\mu^2, \alpha_s)$ dependence of the renormalization scale μ, second it regulates the $\Theta(Q^2/\mu^2, \alpha_s)$, Q^2 scale dependence. From eq.1.29 we notice that the running coupling $\alpha_s(Q^2)$ decreases and tends to zero as Q (i.e. t) increases. This property of QCD is known as *asymptotic freedom*.

The renormalization scale μ can be removed from the running coupling by introducing a scale Λ_{QCD} at which the coupling will diverge (i.e. α_s will become strong) by setting [2]

$$\ln\frac{Q^2}{\Lambda_{QCD}^2} = -\int_{\alpha_s(Q^2)}^{\infty} \frac{du}{\beta(u)}. \tag{1.30}$$

The integral in eq.1.30, at one loop level, leads to [2],

$$\alpha_s(Q^2) = \frac{1}{b\ln(Q^2/\Lambda_{QCD}^2)}, \tag{1.31}$$

where Λ_{QCD} is of the order of 200 MeV and indicates the boundary for $Q \approx 1 \text{GeV}$ below which $\alpha_s(Q^2)$ becomes large and perturbative calculations break down. The value of Λ_{QCD} is determined from the measurement of α_s and will depend on the number of flavours used in loop calculations and the renormalization scheme. The often used value of Λ_{QCD} is the 5-flavour QCD scale $\Lambda_{QCD}^{(5)\overline{MS}}$ performed in the modified minimal subtraction scheme [4]. In fig.1.2 we show various experimental tests of the running coupling in good agreement with the theoretical predictions. The average
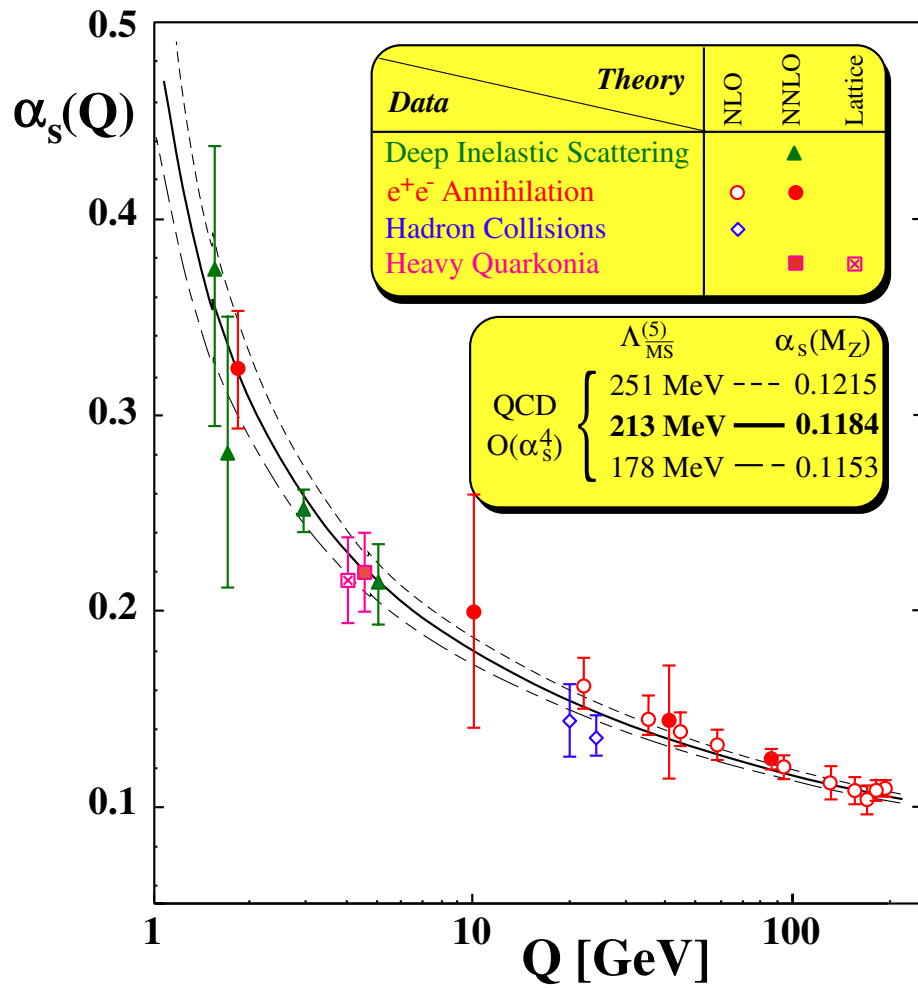
Figure 1.2: Experimental tests of the QCD running coupling [5].

world value for the coupling constant at the Z^0 mass is

$$\alpha_s(\text{M}_\text{Z}) = 0.118 \pm 0.002, \qquad (1.32)$$

from which the value of $\Lambda_{\text{QCD}}^{(5)\overline{MS}}$ can be deduced to be

$$\Lambda_{\text{QCD}}^{(5)\overline{\text{MS}}} = 208^{+25}_{-23} \text{ MeV}. \tag{1.33}$$

1.2.4 The proton structure and the naive parton model

The information about the proton structure is extracted from deep inelastic lepton-hadron scattering (DIS) experiments. The two incoming particles (usually electron and proton), shown in fig.1.3, are pictured as exchanging a virtual photon (or Z^0 boson) with large transverse momentum squared during which the proton breaks down into a struck quark and remnant jets of hadrons.
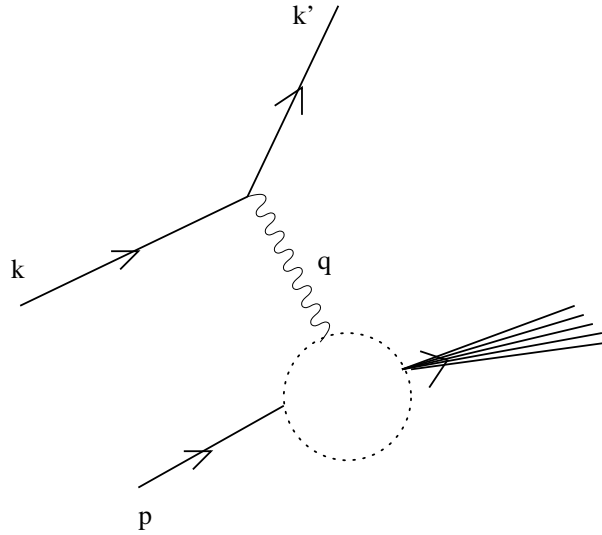
Figure 1.3: Illustration of an DIS collision.

In fig.1.3 the incoming and outgoing lepton (electron) four-momenta are labeled k^μ and k'^μ, the incoming hadron (proton) four momentum as p^μ and the momentum transfer as $q^\mu = k^\mu - k'^\mu$. The standard deep inelastic variables can be defined as

$$Q^2 = -q^2,$$

$$M^2 = p^2,$$

$$\nu = p \cdot q,$$

$$x = \frac{Q^2}{2\nu},$$

$$y = \frac{q \cdot p}{k \cdot p}. \tag{1.34}$$

The inclusive spin averaged cross section for lepton-hadron scattering can be written as

$$\frac{d^2 \sigma^{lh}}{dx dQ^2} = \frac{4\pi\alpha^2}{xQ^4} \left[xy^2 F_1(x, Q^2) + (1-y)F_2(x, Q^2) \right], \tag{1.35}$$

in which the mass of the proton can be neglected and where α^2 is the electromagnetic coupling constant. In eq.1.35 F_1 and F_2 are gauge invariant functions called structure functions parametrizing the structure of the hadron probed by the virtual photon. In the leading order perturbative QCD picture the photon is considered to scatter from a point-like constituent of the proton moving parallel to it and carrying a fraction ε of the proton momentum. At leading order $(\gamma^* q \to q)$ the form of the structure functions is given by

$$2F_1(x, Q^2) = \frac{1}{x}F_2(x, Q^2) = \sum_q e_q^2 \int_0^1 d\varepsilon \; q(\varepsilon)\delta(x - \varepsilon) = \sum_q e_q^2 q(x), \tag{1.36}$$

where $q(x)$ is a quark momentum distribution which describes the probability that the struck quark carries a fraction x of the proton's momentum p. Thus at the leading order the structure functions depend only on x; this is known as $Bjorken$ scaling (i.e. partons behave as point-like particles) as shown in Fig.1.4. The relation between both structure functions is known as the $Callan - Gross\ relation$ and is the consequence of quarks being spin 1/2 particles.

1.2.5   Scaling violation and the Altarelli-Parisi equations

In this section we show how QCD gluon radiation introduces a Q^2 dependence of the F_2 structure function.

Adding next to the leading order terms $(\gamma^* q \to qg)$ to the leading order $(\gamma^* q \to q)$ as shown in fig.1.5 the F_2 structure function is modified to

$$\frac{1}{x}F_2(x, Q^2) = \sum_q e_q^2 q(x) + \sum_q \frac{e_q^2 \alpha_s}{2\pi} \int_x^1 \frac{dz}{z} q\left(\frac{x}{z}\right) \tag{1.37}$$
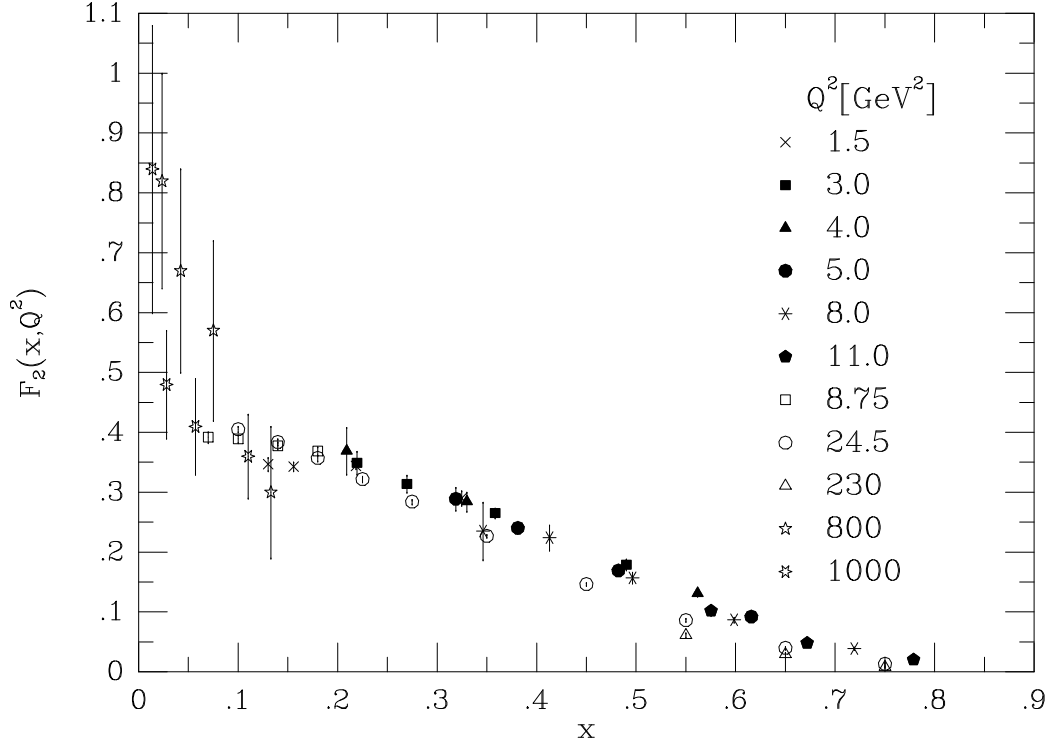
Figure 1.4: Scaling of the F_2 structure function taken from [2]

$$\int_0^{\frac{Q^2}{z}} d(-\hat{t}) C_F \left[\frac{1}{-\hat{t}} \frac{1+z^2}{1-z} - \frac{z^2(\hat{t}+2Q^2)}{(1-z)Q^4} \right],$$

where the quark momentum fraction is expressed as

$$z = \frac{x}{\varepsilon} = \frac{Q^2}{2p_i \cdot q} = \frac{Q^2}{((p_i+q)^2 - q^2)} = \frac{Q^2}{\hat{s}+Q^2}, \tag{1.38}$$

and variables with a hat indicate that we are considering a process at the partonic level and x is the usual Bjorken variable.

The expression in eq.1.37 has two singularities. The first singularity arises when $z \to 1$ and corresponds to the limit

$$\hat{s} = Q^2 \frac{1-z}{z} \to 0. \tag{1.39}$$

This singularity is known as infrared soft and corresponds to the emitted gluon with momentum $k = 0$. We will explain how the soft infrared singularity cancels with loop vertex corrections, for now we regularize it with a cutoff at $z_{soft} < 1$.
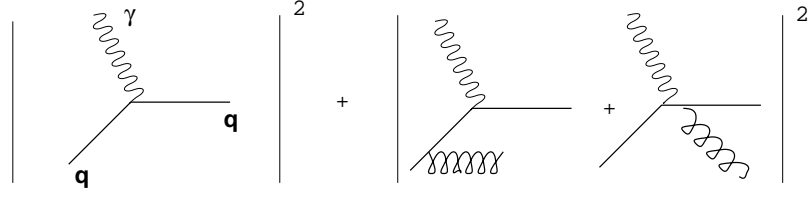
Figure 1.5: Real part of the NLO contribution to $\gamma^* q \to q$.

The second singularity in eq.1.37 arises as $\hat{t} \to 0$ and is known as the mass or collinear singularity. The collinear singularity corresponds to the incident quark emitting a collinear gluon while itself remaining on the mass shell. We regularize the collinear singularity with a cut off at $\hat{t} = -\mu_{coll}^2$ which will be absorbed into the bare quark distribution. Keeping only leading logarithms, the F_2 structure function can now be expressed as

$$\frac{1}{x} F_2(x, Q^2) = \sum_q e_q^2 q(x) + \sum_q \frac{e_q^2 \alpha_s}{2\pi} \int_x^{z_{\text{soft}}} \frac{dz}{z} q\left(\frac{x}{z}\right) P_{qq}(z) \ln\left(\frac{Q^2}{\mu_{\text{coll}}^2}\right). \qquad (1.40)$$

We can chose to set μ_{coll}^2 equal to the renormalization scale μ^2 at which the coupling α_s is defined, and express F_2 as

$$\frac{1}{x} F_2(x, Q^2) = \sum_q e_q^2 q(x) + \sum_q \frac{e_q^2 \alpha_s(\mu^2)}{2\pi} \int_x^{z_{\text{soft}}} \frac{dz}{z} q\left(\frac{x}{z}\right) P_{qq}(z) \ln\left(\frac{Q^2}{\mu^2}\right), \qquad (1.41)$$

where P_{qq} represents the probability,

$$P_{qq} = C_F \left(\frac{1+z^2}{1-z}\right) \qquad (1.42)$$

of a quark to emit a gluon with a momentum fraction $1 - z$, and where the colour factor $C_F = \frac{4}{3}$.

At this point we introduce virtual gluon corrections to the leading order $\gamma^* q \to q$ process as shown in fig.1.6.

The sum of the amplitudes squared of fig.1.5 and fig.1.6 leads F_2 to be expressed as

$$\frac{1}{x} F_2(x, Q^2) = \sum_q e_q^2 \int \frac{dz}{z} q\left(\frac{x}{z}\right) \left(\delta(1-z) + \frac{\alpha_s(\mu^2)}{2\pi} P_{qq}(z) \ln\left(\frac{Q^2}{\mu^2}\right)\right). \qquad (1.43)$$
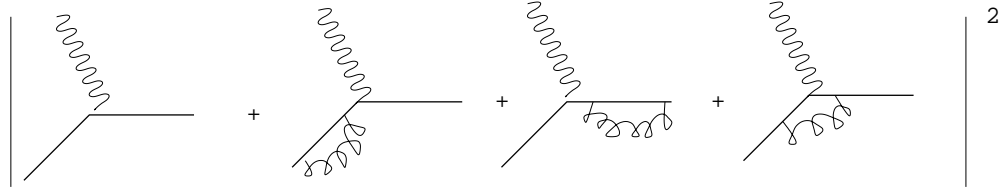
Figure 1.6: Virtual part of the NLO contribution to $\gamma^* q \to q$.

In eq.1.43 the soft singularities have been canceled by the virtual corrections to $\gamma^* q \to q$ process, in doing so the splitting function P_{qq} has been modified and now includes a term which removes its original singularity. P_{qq} can now be expressed as

$$P_{qq} = C_F \frac{1+z^2}{(1-z)_+} + \frac{3}{2} C_F \delta(1-z),$$ (1.44)

where the $(+)$ prescription is defined as

$$\int_0^1 dz \frac{f(z)}{(1-z)_+} \equiv \int_0^1 dz \frac{f(z) - f(1)}{1-z}.$$ (1.45)

In eq.1.43 in addition to the x dependence, the structure function F_2, now has a logarithmic Q^2 dependence which violates Bjorken scaling with μ the cutoff scale for collinear gluon emissions. The Q^2 logarithmic dependence can be absorbed into the quark probability distribution function and eq.1.43 can be rewritten as

$$
\begin{aligned}
\frac{1}{x} F_2(x, Q^2) &= \sum_q e_q^2 \int_x^1 \frac{d\varepsilon}{\varepsilon} \left(q(\varepsilon) + \Delta q(\varepsilon, Q^2) \right) \delta \left(1 - \frac{x}{\varepsilon} \right) \\
&= \sum_q e_q^2 \left(q(x) + \Delta q(x, Q^2) \right),
\end{aligned}
$$ (1.46)

where
$$\Delta q(x, Q^2) = \frac{\alpha_s(\mu^2)}{2\pi} \ln \left(\frac{Q^2}{\mu^2} \right) \int_x^1 \frac{d\varepsilon}{\varepsilon} q(\varepsilon) P_{qq} \left(\frac{x}{\varepsilon} \right).$$ (1.47)

From eq.1.47 the quark density $q(x, Q^2)$ now depend on Q^2 and its evolution as function of Q^2 can be written as

$$\frac{d}{d \ln Q^2} q(x, Q^2) = \frac{\alpha_s(\mu^2)}{2\pi} \int_x^1 \frac{d\varepsilon}{\varepsilon} q(\varepsilon, Q^2) P_{qq} \left(\frac{x}{\varepsilon} \right),$$ (1.48)

The expression in eq.1.48 is the direct consequence of quarks interacting through the gluonic field. As the scale of photon-quark interaction increases, the number of partons

sharing the proton momentum is increased and so the probability of finding a quark at small x. Furthermore because high-momentum quarks lose momentum through gluon radiation the chance of finding a quark with high x should decrease.

To the diagram in fig.1.5 we should also add contributions from the gluon annihilation process $(\gamma^* g \to q\overline{q})$ shown in fig.1.7. The F_2 structure function contains thus
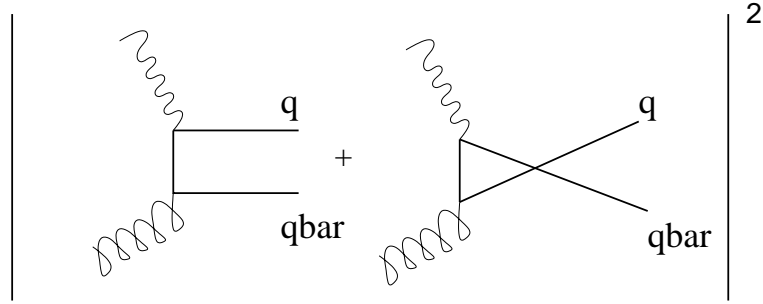
Figure 1.7: NLO contribution from gluon annihilation.

an additional contribution

$$\frac{1}{x}F_2(x,Q^2) = \sum_q e_q^2 \int_x^1 \frac{d\varepsilon}{\varepsilon} g(\varepsilon) \frac{\alpha_s(\mu^2)}{2\pi} P_{qg}\left(\frac{x}{\varepsilon}\right) \ln\left(\frac{Q^2}{\mu^2}\right), \tag{1.49}$$

where $g(\varepsilon)$ is the gluon density in the proton and where

$$P_{qg}\left(\frac{x}{\varepsilon}\right) = \frac{1}{2}\left(\left(\frac{x}{\varepsilon}\right)^2 + \left(1 - \frac{x}{\varepsilon}\right)^2\right), \tag{1.50}$$

is the probability for a gluon to annihilate into a $q\overline{q}$ pair.

The complete quark evolution equation can now be written as

$$\frac{d}{d\ln Q^2}q_f(x,Q^2) = \frac{\alpha_s(\mu^2)}{2\pi} \int_x^1 \frac{d\varepsilon}{\varepsilon} \left(q_f(\varepsilon,Q^2)P_{qq}\left(\frac{x}{\varepsilon}\right) + g(\varepsilon,Q^2)P_{qg}\left(\frac{x}{\varepsilon}\right)\right), \tag{1.51}$$

for each quark flavour f and is valid for any massless quark and antiquark. The full expression in eq.1.51 is known as Dokshitzer-Gribov-Lipatov-Altarelli-Parisi (DGLAP) [6, 7, 8, 9] equation. The DGLAP equation describes a quark with momentum fraction x coming from a parent quark with larger momentum fraction ε which has radiated a gluon. The corresponding equation for the gluon distribution can be written as

$$\frac{d}{d\ln Q^2}g(x,Q^2) = \frac{\alpha_s(\mu^2)}{2\pi} \int_x^1 \frac{d\varepsilon}{\varepsilon} \left(\sum_f q_f(\varepsilon,Q^2)P_{gq}\left(\frac{x}{\varepsilon}\right) + g(\varepsilon,Q^2)P_{gg}\left(\frac{x}{\varepsilon}\right)\right), \tag{1.52}$$

where

$$P_{gq} = C_F \left(\frac{1 + (1 - z)^2}{z} \right), \tag{1.53}$$

and

$$P_{gg} = 2C_A \left(\frac{1 - z}{z} + \frac{z}{(1 - z)_+} + z(1 - z) \right) + 2\pi b \, \delta(1 - z), \tag{1.54}$$

are respectively the gluon-quark and gluon-gluon splitting functions, and where b is given in eq.1.26. In fig.1.8 we show data on the structure function $F_2^{\mu p}$ and prediction from the DGLAP evolution equations using MRS [10] parton distribution function set.
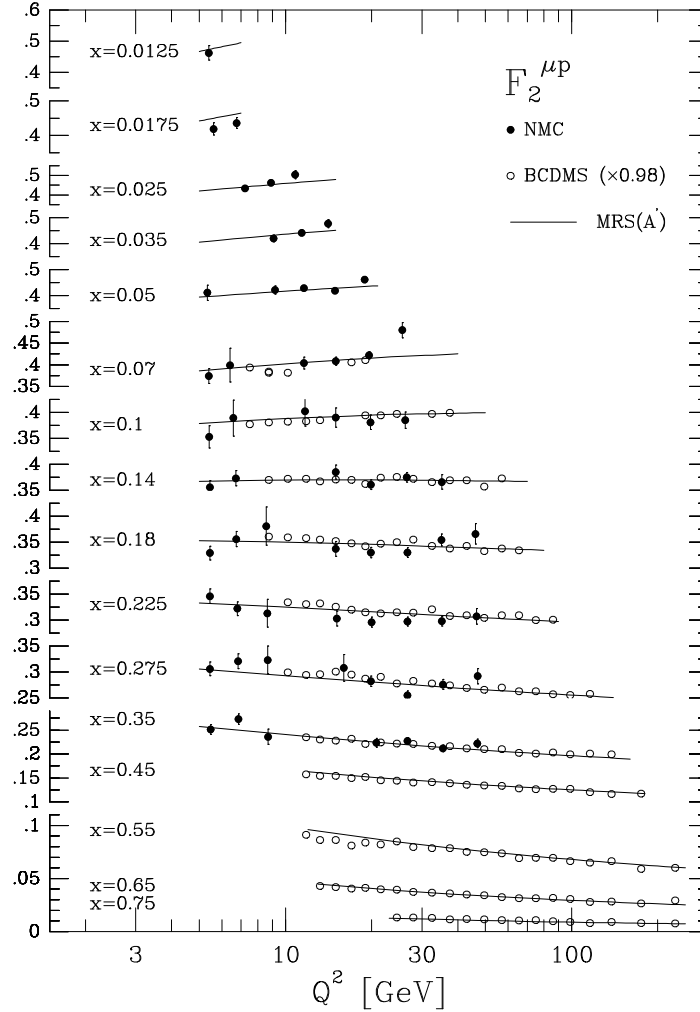
Figure 1.8: QCD fits to muon-proton DIS F_2 taken from [2]

1.2.6   Parton distribution functions

Parton distribution functions are obtained from accurate measurements of the structure functions $F_2(x, Q^2)$. The procedure consists of performing a QCD fit to the entire experimental data set. The QCD fit starts by assuming a certain parametrized form in x for the different parton distribution at low Q^2, parton distributions are then evolved up in Q^2 with a particular value of $\Lambda_{\overline{MS}}$ through the DGLAP evolution equations to the values of Q^2 where the structure function has been measured. The initial set of parameters is then chosen to correspond to the best fit to the experimental data. In fig.1.9 we show a set of parton distribution functions at $Q^2 = 20 \text{ GeV}^2$.
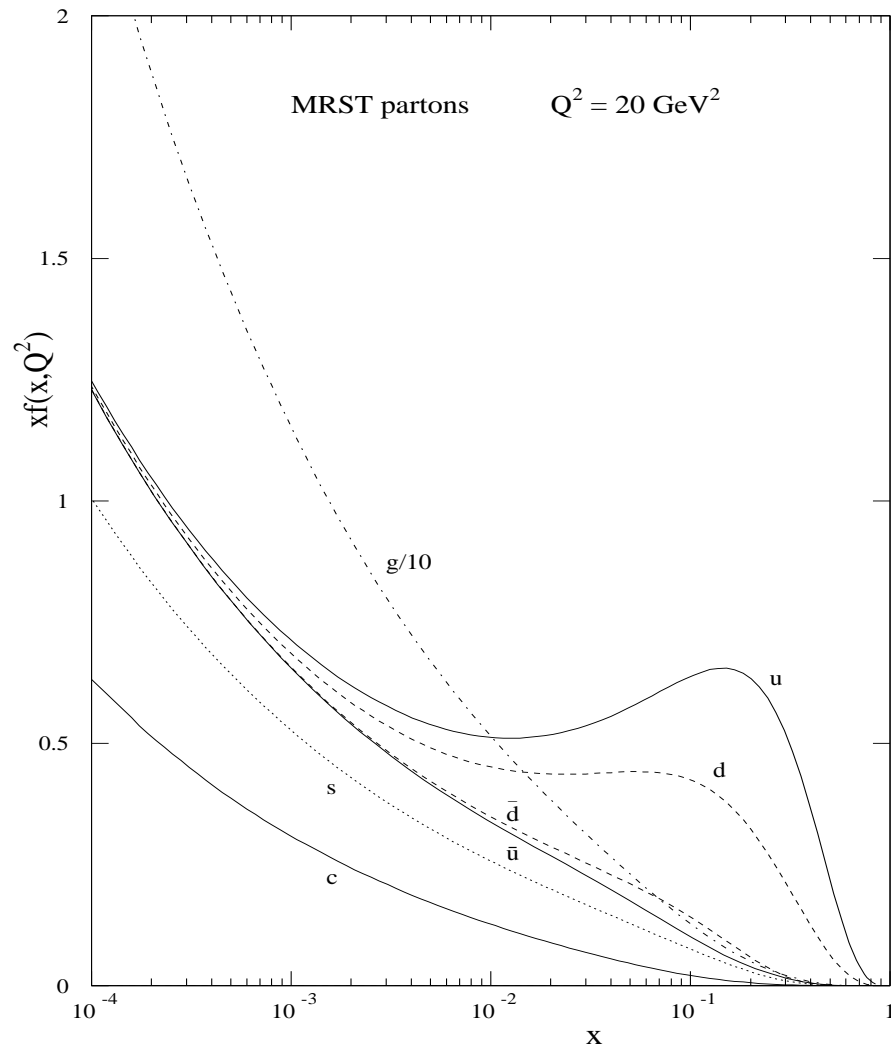
Figure 1.9: Parton density distributions as functions of x for $Q^2 = 20$ GeV^2 taken from [11].

1.3   Regge Theory and Total cross sections

1.3.1   Two body scattering

In this section we give a brief overview of the concepts that we use to derive the remarkable unitarity relation called the "optical theorem". In fig.1.10 we show the general expression for two-to-two particle scattering processes. The scattering process
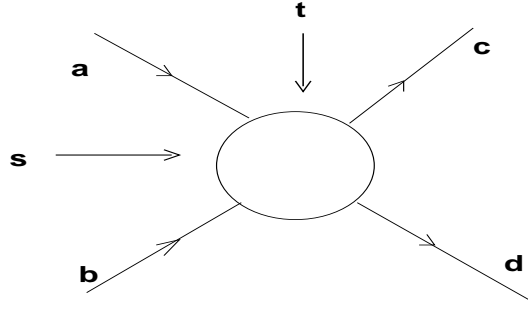
Figure 1.10: The scattering process in the s channel of eq.1.55.

between two particles in the s channel can be written as

$$a(p_1) + b(p_2) \rightarrow c(p_3) + d(p_4), \tag{1.55}$$

where p_i (i=1,...4) are the respective 4 momenta of particles a, b, c and d. The Mandelstam variables s, t, u, which are invariant under Lorentz transformations, are defined as

$$s = (p_1 + p_2)^2, \tag{1.56}$$

$$t = (p_1 - p_3)^2, \tag{1.57}$$

$$u = (p_1 - p_4)^2. \tag{1.58}$$

For massive particles the Mandelstam variables satisfy the relation

$$s + t + u = \sum_i^4 m_i^2, \tag{1.59}$$

which leaves us with only two independent variables which we choose to be s and t. For the s-channel process t represents the momentum transferred and the scattering angle between particles 1 and 3 can be expressed as

$$t = m_1^2 + m_3^2 - 2p_1 p_3, \tag{1.60}$$

$$= m_1^2 + m_3^2 - 2E_1 E_3 + 2|\mathbf{p_1}||\mathbf{p_3}| \cos(\theta). \tag{1.61}$$

Thus for an elastic process

$$a(p_1) + b(p_2) \rightarrow a(p_1) + b(p_2), \tag{1.62}$$

in the forward direction (i.e. $\theta = 0$) t is zero.

The scattering process in eq.1.55, and hence its scattering amplitude $\mathcal{A}_{ab}$, should be Lorentz invariant, thus the scattering amplitude can be expressed as a function of the Mandelstam variables s and t.

The differential cross section for the process in eq.1.55 can be expressed as

$$d\sigma = \frac{|\mathcal{A}_{ab}(s,t)|^2}{F}dQ,$$ (1.63)

where F is the flux of the incoming particles and dQ is the Lorentz invariant phase space factor which for two body scattering is given by

$$dQ = (2\pi)^4\delta^{(4)}(p_3 + p_4 - p_1 - p_2)\frac{d^3\mathbf{p_3}}{(2\pi)^3 2E_3}\frac{d^3\mathbf{p_4}}{(2\pi)^3 2E_4},$$ (1.64)

where free particles are represented by plane waves with the normalization of $2E$ particles per unit volume. We express the flux factor F in eq.1.63 as

$$F = 4\sqrt{[(p_1 p_2)^2 - m_1^2 m_2^2]},$$ (1.65)

which in the high energy limit becomes $F \approx 2s$.

In the center-of-mass frame where $|\mathbf{p_1}| = |\mathbf{p_2}|$ and $|\mathbf{p_3}| = |\mathbf{p_4}|$ the differential cross section is expressed as

$$\frac{d\sigma}{d\Omega_{cm}} = \frac{1}{64\pi^2 s}\frac{|\mathbf{p_3}|}{|\mathbf{p_1}|} \mid \mathcal{A}_{ab}(s,t) \mid^2,$$ (1.66)

where for spinless particles

$$d\Omega_{cm} = d(\cos(\theta))d\phi = \frac{dt}{2|\mathbf{p_1}||\mathbf{p_3}|}d\phi.$$ (1.67)

The Lorentz invariant expression in eq.1.66 can now be expressed as

$$\frac{d\sigma}{dt} = \frac{1}{16\pi s^2}|\mathcal{A}_{ab}(s,t)|^2.$$ (1.68)

1.3.2   The S-matrix, unitarity and the optical theorem

The scattering operator S is such that its matrix elements between the initial and final states $\langle f \mid S \mid i \rangle$ squared give us the probability P_{fi} that $\mid f \rangle$ will be the final state

resulting from $\mid i \rangle$ i.e.

$$P_{fi} = \mid \langle f \mid S \mid i \rangle \mid^2 = \langle i \mid S^\dagger \mid f \rangle \langle f \mid S \mid i \rangle, \tag{1.69}$$

where $S^\dagger$ is the Hermitian adjoint of S. The $S - matrix$ can be expressed as the sum of two parts, the non-interaction part (the identity operator) and the interaction part (containing the dynamics of strong interactions)

$$S_{fi} = \delta_{fi} + iT_{fi}. \tag{1.70}$$

For strong interactions with high momentum transfer the scattering matrix elements can be calculated using standard perturbative QCD techniques where the $T - matrix$ is usually defined as

$$\langle f \mid iT \mid i \rangle = i(2\pi)^4 \delta^{(4)}(\sum p_f - \sum p_i)\mathcal{A}_{fi}, \tag{1.71}$$

and where $\mathcal{A}_{fi}$ is the scattering amplitude for the state $\mid i \rangle$ to end in the state $\mid f \rangle$.

The $S - matrix$ contains the following assumptions:

$Postulate(i)$

The scattering process and hence the $S - matrix$ is Lorentz invariant.

$Postulate(ii)$

The scattering $S - matrix$ is unitary. By using the conservation of probability, if we are to start with some initial state $\mid i \rangle$ the probability that there will be some final state $\mid f \rangle$ must be unity. From eq.1.69 this translate to

$$\begin{aligned} \sum_n P_{ni} &= \sum_n \mid \langle n \mid S \mid i \rangle \mid^2 = \sum_n \langle i \mid S^\dagger \mid n \rangle \langle n \mid S \mid i \rangle \\ &= \langle i \mid S^\dagger S \mid i \rangle, \end{aligned} \tag{1.72}$$

where free particle states $\mid n \rangle$, constitute a complete orthonormal set of basis states satisfying the completeness relation,

$$\sum_n \mid n \rangle \langle n \mid = \mathbf{1}. \tag{1.73}$$

Since eq.1.73 must be true for any state $\mid i \rangle$ we have

$$S^\dagger S = \mathbf{1} = SS^\dagger. \tag{1.74}$$

$Postulate(iii)$

The scattering amplitude is assumed to be an analytic function of the Mandelstam variables s and t regarded as complex variables.

The Optical theorem is a consequence of the unitarity of the $S - matrix$. From

$$S = 1 + iT, \tag{1.75}$$

and using eq.1.74 we obtain

$$-i(T - T^{\dagger}) = TT^{\dagger}. \tag{1.76}$$

The matrix elements of eq.1.76 between particles states $\mid i \rangle$ and $\mid f \rangle$ can be written as

$$\langle f \mid T^{\dagger} T \mid i \rangle = \sum_{n} \left(\prod_{i=1}^{n} \int \frac{d^3 p_i'}{(2\pi)^3} \frac{1}{2E_i} \right) \langle f \mid T^{\dagger} \mid n \rangle \langle n \mid T \mid i \rangle, \tag{1.77}$$

using the definition in eq.1.71 we can now write eq.1.77 as

$$-i[\mathcal{A}_{fi} - \mathcal{A}_{if}^*] = \sum_{n} \left(\prod_{i=1}^{n} \int \frac{d^3 p_i'}{(2\pi)^3} \frac{1}{2E_i} \right), \tag{1.78}$$

$$\mathcal{A}_{nf}^* \mathcal{A}_{ni} \times (2\pi)^4 \delta^{(4)}(\sum_{i}^{n} p_i' - \sum_{i} p_i).$$

For identical initial and final state we can write eq.1.78 as

$$2Im(A_{el}(s, t = 0)) = \sum_{n} \int dQ_n \mid \mathcal{A}_{in} \mid^2 . \tag{1.79}$$

Dividing the right hand side by the high energy limit flux factor F (see eq.1.65) we obtain the expression known as the optical theorem,

$$\sigma_{tot} = \frac{1}{s} Im(A_{el}(s, t = 0)). \tag{1.80}$$

This relation (as shown in fig.1.11) is well known in non-relativistic potential scattering where, due to conservation of probability, the magnitude of the wave function in the 'shadow' behind the target at (θ=0) must be reduced relative to the incoming wave by an amount equal to the total scattering in all directions. The expression in eq.1.80 is just the extension of the same conservation requirement to the relativistic situation.

Using eq.1.80 we can now rewrite eq.1.68 as

$$\frac{d\sigma_{ela}}{dt}\mid_{t=0} = \frac{\sigma_{tot}^2}{16\pi}(1 + \beta) \tag{1.81}$$

where β is the ratio of the real to the imaginary part of the elastic amplitude.

Figure 1.11: The optical theorem.

1.3.3 Regge Theory

The idea of Regge poles was introduced in non relativistic potential theory by Regge [12]. Regge poles are poles of the partial wave amplitude $a(J, s)$ in the analytically continued complex angular momentum plane J. Such poles define trajectories $\alpha(s)$ which are functions of the momentum squared $k^2 = (s - 4m^2)/2$. The scattering amplitude in the relativistic case, for $s \to \infty$ and $t < 0$ fixed, can be expressed as the exchange of a sum of poles in the t-channel

$$A(s, t) = \sum_k \frac{1 + \xi_k \exp i\pi\alpha_k(t)}{\sin\left(\pi\alpha_k(t)\right)} \gamma_k(t) \left(\frac{s}{s_0}\right)^{\alpha_k(t)}, \qquad (1.82)$$

where $\gamma_k(t)$ are the residue of the pole and ξ_k is known as the signature, defined as $\xi_k = (-1)^{J-1/2}$ for baryons and $\xi_k = (-1)^J$ for mesons. Each Regge pole corresponds to a family of exchanged particles belonging to the same trajectory $\alpha_k(t)$, which is an analytic function of t. The value of $\alpha_k(t)$ is equal to the spin of the particle whenever t takes the value of its mass squared. Regge poles are ordered into different families according to their quantum numbers. For Regge poles with quantum numbers of mesons one observes remarkable agreement with data by using linear trajectories

$$\alpha(t) = \alpha(0) + \alpha't, \qquad (1.83)$$

as shown in fig.1.12 with $\alpha(0)$ the intercept and α' the slope. The Regge pole parametrization gives a very good phenomenological description of the bulk of data on high-energy scattering at small momentum transfers, $|t| \leq 1$ GeV^2 and $s \gg t$. Using the optical theorem and the expression in eq.1.82 the total cross section can be written as [12]

$$\sigma_{tot} = s^{-1} Im\left(A(s, t = 0)\right) \sim \left(\frac{s}{s_0}\right)^{\alpha_k(0)-1}. \qquad (1.84)$$
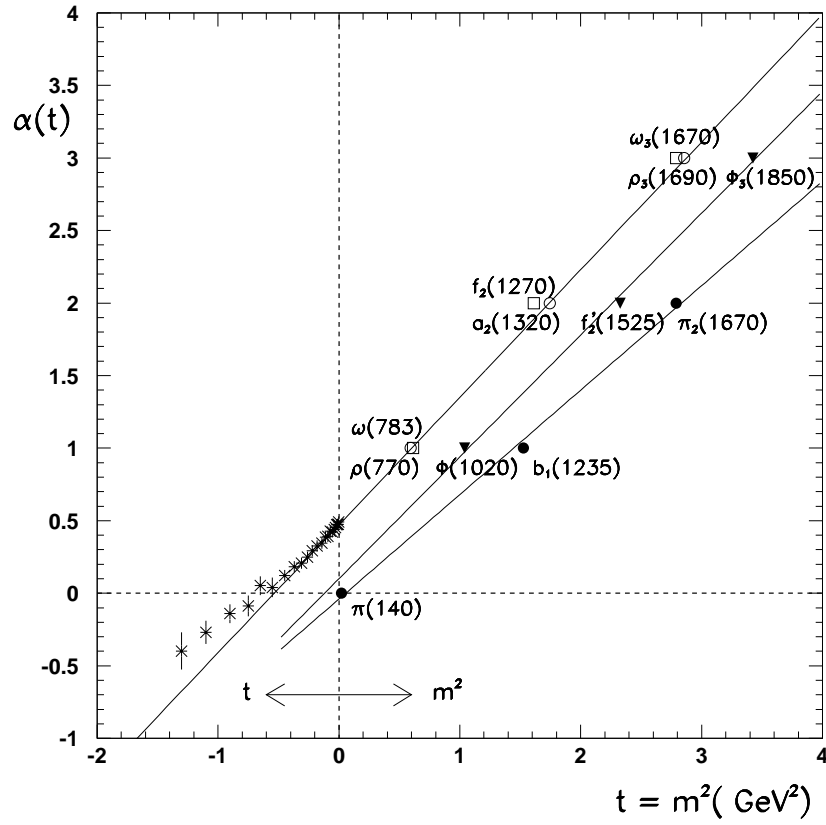
Figure 1.12: The ρ (∘), ω (□), ϕ (△) and π (●) trajectories. The ρ trajectory has been continued as measured in $\pi^- p \to \eta n$ taken from [13].

At high energies, the process is dominated by the term with the largest value of $\alpha_k(0)$, the so-called pomeron trajectory with the quantum numbers of the vacuum ($J=0$, $I=0$, $C=+1$). Since at high energies, processes with the exchange of quantum numbers die out there are no known hadronic bound states on this trajectory (although some candidates have been proposed such as glue-balls) and its explanation in terms of QCD remains unknown [14]. It has been shown in [15] that a remarkably good description of hadron-hadron scattering data at high energies and small momentum transfers can be obtained with the exchange of one pomeron, with a Regge trajectory

$$\alpha_P(t) = 1.0808 + 0.25t. \tag{1.85}$$

With the pomeron trajectory alone contributing to the Regge expansions in eq.1.82 the energy dependence of the total cross section is given by

$$\sigma_{tot}(s) = \sigma_{tot}(s_0) \left(\frac{s}{s_0}\right)^{0.0808}. \tag{1.86}$$

Since the intercept in eq.1.85 is larger than one it would lead to a violation of the Froissart-Martin bound $\sigma_{tot} \leq C \ln^2 \left(\frac{s}{s_0} \right)$ [16] for extremely high values of s, which indicates that unitarity corrections must play an important role at high energies.

1.3.4 Conclusion

In this chapter we have described a number of concepts used in the theory of strong interactions of both perturbative and non-perturbative nature. In the following two chapters we give a brief overview of how some of the perturbative concepts can be implemented in the form of a Monte Carlo event generator in order to simulate particle collisions involving strong interactions. The total cross section and its parametrization in terms of Regge trajectories will be particularly useful in Chapter 6 where we introduce a new model based on an eikonal approach incorporating both the perturbative and non-perturbative part in order to simulate the 'underlying event' in jet events. We consider our multiparticle interaction approach as a unitary correction to the hard and soft Born-graph cross sections.

Chapter 2

Monte Carlo Methods

2.1   Introduction

Monte Carlo techniques can be defined as methods which use random numbers to solve problems of deterministic or analytic nature such as (multidimensional) integration or to simulate complex physical phenomena of fundamentally random nature. In high energy particle physics Monte Carlo techniques may be used for a variety of purposes ranging from the detailed detector simulation to the full event generation and total cross section integration. Monte Carlo techniques are seen as a powerful way of performing calculations generally too complicated for a more classical approach.

In this chapter we present a brief overview of the Monte Carlo methods used in HERWIG and compare this particular technique to other numerical integration methods. We also show how to improve the efficiency of the Monte Carlo integration method in few dimensions using two particular techniques of variance reduction.

2.2   Random Number Generators

A random variable is a variable that can take more than one value and for which any particular value cannot be predicted in advance. A random number is just a particular value of the random variable. In principle it is impossible to generate a true sequence of random numbers using a mathematical formalism, since any algorithm would lead to a strictly deterministic and consequently reproducible sequence of numbers. Since it is not possible to generate a truly random sequence of numbers, we use pseudorandom numbers in all of our calculations. They are generated according to a definite algorithm which generats a sequence of numbers such as to be indistinguishable from a sequence generated truly at random (a sequence of truly random numbers can be generated by a random physical process such as radioactive decay for example). Thus when we talk about random numbers in this thesis we really mean pseudorandom. For a more detailed discussion we refer to [17] and for the update on more modern generators to [18].

2.2.1   Multiplicative Linear Congruential Generators

In this section we will give an example of a simple random number generator. However we must point out that it is plagued by a severe insufficiency and that a more modern generator should be used instead [18].

MLCGs generate a sequence of random numbers by using the simple recursive formula given below

$$r_{i+1} = (ar_i + c) \bmod m. \tag{2.1}$$

This basic algorithm given a starting value or seed, will calculate a sequence of random integers r_i in the range $(0, m\text{-}1)$ where m - 1 is usually, but not always, the largest integer which can be represented on a given machine. The two other variables are a the multiplier and c an additional constant which usually can take two values 1 or 0 depending respectively on whether we want to generate an exact zero or not. The integers obtained through eq.2.1 are then converted to floating point numbers in the range $[0,1)$ by dividing by m. In MLCGs pseudorandom number generators the entire sequence of numbers will repeat itself after a certain period (this being a more general property of pseudorandom generators). To improve MLCGs the early theoretical work concentrated mainly on maximizing the period (the maximum period in MLCGs is at most m since this is the maximum possible generated integer) of generators. To improve MLCGs we can search for values of a which will achieve the maximum period and try to minimize the amount of correlation between two successive points in the recursive series (i.e between r_i and r_{i+1}).

Marsaglia has shown that all types of MLCG generators have an important defect [18]. If we take n-tuples as coordinates of points in n-dimensional space then all generated points will lie on a certain finite number of parallel hyperplanes. Marsaglia has shown that for MLCGs the number of hyperplanes will be fewer than what would be expected from numbers generated truly at random. Typically the number of hyperplanes will be a function of n dimensions and the maximum possible integer number generated by the machine as shown in eq.2.2. Marsaglia has also shown how to choose

a best multiplier of the generator for a given m in order to maximize the number of hyperplanes and the minimum number of dimensions in which the ordering would become apparent.

To make the ordering of points on hyperplanes apparent we need to take a narrow hyperslice through n-space taking only points which lie within it and project it on the first two dimensions (i.e. $x - y$) plane. All the hyperplanes not parallel to the hyperslice will then appear as bands in the $x - y$ plane. If for example we take a 16 bits machine in $n = 3$, generated points will be distributed over 73 hyperplanes but in $n=10$ only over 13, making the pattern of points less random. This progressive 'ordering' of points as we go up in number of dimensions can have several undesired effects on our Monte Carlo calculations.

First, the uneven coverage of the integration volume introduces a bias which may induce the integral to converge toward a numerical result different from the one calculated analytically .

Second, in generating phase-space points with many dimensions and few hyperplanes, the MLCG method will produce artificial correlations between parameters which will show up in our final results.

Third if we have very few hyperplanes a large portion of phase space might not be sampled at all and so we might lose some points in event generation.

The maximum number of hyperplanes using MLCGs is

$$Hyperplanes = (n!2^t)^{1/n}, \tag{2.2}$$

where t is the machine word length (16, 32, 36 bits) and n is the number of dimensions.

2.2.2   Compound Multiplicative Congruential Generators

It is possible to improve the Marsaglia hyperplane problem by combining two MLCGs (or more) together [17]. CMCGs generate an integer random number by combining

two simple MLCGs using the last two seeds from the the sequence

$$r_{i+1} = (ar_i + br_{i-1} + c) \ mod \ m. \tag{2.3}$$

This type of algorithm is used in HERWIG. The advantage of this method is to give the same number of hyperplanes in n dimensions as the simple generator MLCG in $n/2$ dimensions. The number of hyperplanes can be increased arbitrarily by adding more terms to the recursive sequence in eq.2.3.

2.3 Distribution functions and Non-Uniform Generators

Let $f(x)dx$ be the probability $P(x)$ of finding a random variable x in the interval $[x, x + dx]$, $f(x)$ is then called a probability density function (pdf) of variable x. Since x must lie somewhere in the range $[-\infty, +\infty]$ the probability density function can be normalized to unity as

$$\int_{-\infty}^{+\infty} f(x)dx = 1. \tag{2.4}$$

We define also

$$\int_{-\infty}^{x} f(x')dx' = F(x), \tag{2.5}$$

the cumulative distribution function. To construct a random variable x uniformly distributed in the range $[x_1, x_2]$ the probability density function of x can be expressed as

$$f(x) = \begin{cases} \frac{1}{x_2 - x_1} & x_1 \leq x \leq x_2 \\ 0 & otherwise \end{cases} \tag{2.6}$$

the random variable x sampled from

$$x_i = x_1 + (x_2 - x_1)r_i. \tag{2.7}$$

Because a certain confusion is made between the two notions of randomness and distribution, we would like to stress that a random variable may have any distribution

we like and that a uniformly distributed sequence of numbers may not be random at all.

In the following sections we will present two techniques used in event generators for producing non-uniformly distributed random variables.

2.3.1   Transformation method

It is possible to construct a non-uniformly distributed random variable $x(r)$ from a random variable r uniform in [0,1] by using the inversion technique (or transformation method). To generate a non-uniform random variable $x(r)$ we require that

$$
\begin{aligned}
P(r \leq r') &= P(x \leq x(r')), \\
\int_{-\infty}^{r'} g(r)dr = r' &= \int_{-\infty}^{x(r')} f(x')dx' = F(x(r')),
\end{aligned} \tag{2.8}
$$

where $g(r)$ is the uniform distribution of r in [0,1]. By setting $F(x(r)) = r$ and solving for $x(r)$ (i.e. $x = F^{-1}(r)$), $x(r)$ will be distributed according to $f(x)$.

An example of the inversion technique is given below:

• generate $x(r)$ between 0 and 4 according to $f(x)=x^{-1/2}$:

$$
\begin{aligned}
\frac{\int_0^x x'^{-1/2}dx'}{\int_0^4 x'^{-1/2}dx'} &= r, \\
\rightarrow \ generate \ x \ according \ to \ x(r) &= 4r^2.
\end{aligned} \tag{2.9}
$$

This method can only be applied to functions with invertible integrals.

2.3.2   Rejection Method

This is the method used in event generation (see Chapter 3.4.1). This method can be quite inefficient and can be improved by variance reduction techniques. If we want our random variable x to be distributed according to some probability distribution function $f(x)$ we can choose x uniformly in the integration region $[x_1, x_2]$ and reject it if

$$
r > f(x)/f_{max}, \tag{2.10}
$$

where r is uniformly distributed random number in the range [0,1] and f_{max} is the largest value of $f(x)$ within the integration region. The choosing of x and the test in eq.2.10 are carried out until x is accepted.

2.4 Integral evaluations

In the following section we will briefly review numerical methods used for integral evaluation.

Consider the following integral in one dimension,

$$I = \int f(x)dx. \tag{2.11}$$

There are a number of numerical quadrature methods which we can use to estimate the above integral (which can then be generalized further to d dimensions), the trapezium rule and Simpson's method for example consist of evaluating $f(x_i)$ at evenly spaced points, x_i, on a grid. Using these two methods the integral in eq.2.11 can be estimated as

$$I \approx (x_2 - x_1)\frac{\sum_{i=1}^{N} w_i f(x_i)}{\sum_{i=1}^{N} w_i}. \tag{2.12}$$

The weights w_i in the sum of eq.2.12 may be different for each sampling point x_i, depending on the quadrature method used. In the trapezium rule, the weights are all equal to one except for the first and the last, which are half. The trapezium rule can integrate all first-degree polynomials exactly and the uncertainty on the integral for any function is proportional to $1/N^2$ for large N. The Simpson rule is a higher order quadrature (it requires three points on a given interval). Its alternate sampled points have respectively weights of one and a half and it is guaranteed to integrate all third-degree polynomials exactly. The uncertainty on the integral is proportional to $1/N^4$ for large N. The highest efficiency is however achieved with the higher-order Gaussian quadrature method. Gaussian quadrature at the mth order involves at least m points with (non-uniform) positions and weights derived from the function to be

integrated. For the function to be integrated the mth differential of the integrand must exist and be continuous. This method is guaranteed to integrate ($2m$ - 1)-degree polynomials exactly, and converges as $1/N^{(2m-1)}$ for sufficiently large N.

An alternative numerical technique of integration is to approximate the integral in eq.2.11 by choosing sampled x_i points at random leading to the Monte Carlo estimate of the integral (also known as crude Monte Carlo),

$$
\begin{aligned}
I_{MC} &\approx (x_2 - x_1)\frac{1}{N}\sum_{i=1}^{N} f(x_i), \\
&\approx (x_2 - x_1)\overline{f},
\end{aligned}
\tag{2.13}
$$

where $\overline{f}$ is the arithmetic mean of values of the function $f(x)$ estimated at each sampling point x_i. Given a uniformly distributed random number r_i on the interval [0,1], sampled points x_i are chosen according to eq.2.7. If we assume N is large, we can use the Central Limit Theorem to show that the distribution of $\overline{f}$ will tend to a Gaussian with standard deviation given by

$$
\sigma_{MC} = \frac{\sigma}{\sqrt{N}},
\tag{2.14}
$$

where

$$
\sigma^2 \approx \frac{\sum_{i=1}^{N}[f(x_i) - \overline{f}]^2}{N - 1}.
\tag{2.15}
$$

σ_{MC} in eq.2.14 is the statistical error in the Monte Carlo estimate of the integral. This error goes as $\frac{1}{\sqrt{N}}$ and is independent of the dimensionality of the integral. For a Monte Carlo method to be efficient the integrand $f(x)$ in eq.2.13, must be integrable everywhere, finite and at least piecewise continuous. Under such conditions the Monte Carlo Method estimate will converge to the true value of the integral as N becomes large (the law of large numbers).

2.4.1   Monte Carlo vs quadrature

In our three different examples of quadrature methods (trapezium rule, Simpson's rule and Gaussian quadrature) we have argued that the integral estimate will converge in

one dimension as $\frac{1}{N^2}$, $\frac{1}{N^4}$ and $\frac{1}{N^{(2m-1)}}$ respectively. We can extend these rules to multidimensional quadrature rules in d dimensions where the convergence rate will slow down according to a $1/d$ factor in the exponent. The integral estimates will now converge in accordance with $n = N^{1/d}$ (the number of points along each axis) leading respectively to $\frac{1}{N^{2/d}}$, $\frac{1}{N^{4/d}}$ and $\frac{1}{N^{(2m-1)/d}}$ convergence. The Monte Carlo method will then show a faster convergence than any of the quadrature methods in $d = 4$, 8, and $4m$ - 2 dimensions. This property of the Monte Carlo method is particularly useful in particle physics where integrals are evaluated over 5 or more dimensions. Although Gaussian quadrature converges much faster than a Monte Carlo method when d is low, it is much more difficult to give the uncertainty on the estimate for the former since formulas for calculating the error on the integral are given in terms of values of higher derivatives of the function, which are much harder to calculate than the integral itself. Also, while in the Monte Carlo approach combining results is done by taking the weighted mean (as in experimentally measured quantities) for Gaussian quadrature we must throw away the lower order results and keep only the higher.

In addition to faster convergence in many dimensions, the Monte Carlo approach is particularly suitable for integral estimation of complex integration regions, since we can enclose any region in the smallest hyperrectangle and throw away the points that fall outside the inner region. This is somehow inefficient but allows us to deal in a quite straightforward way with any finite region. This technique cannot be used in numerical quadrature. Furthermore because of computer resources we are limited to a certain maximum number of function evaluations we can make, this feasibility limit is reached except for very low order Gaussian rules before the crossover point where Monte Carlo converges faster than the higher-order Gaussian numerical quadrature, thus making the full convergence of the higher-order rules purely theoretical.

Finally if the 'growth rate' is defined as the smallest number of additional functions evaluations needed to improve the current estimate, with Monte Carlo this can be done by adding a single point while Gaussian quadrature will require going to a higher-order rule, with $(m + 1)^d$ additional points.

2.5   Variance reduction

The biggest disadvantage of Monte Carlo integration is its slow convergence in few dimensions and since the accuracy of the estimate goes as eq.2.14, it is in our advantage, to reduce σ and thus improve the accuracy of our Monte Carlo estimate.

2.5.1   Stratified Sampling

The idea of the stratified sampling method is to divide a volume of integration into a large number of sub-volumes and then calculate integrals separately, using crude Monte Carlo, in each sub-volume. Thus if we divide the integration region into n sub-regions the additive property of the integral operator gives for the Monte Carlo estimate

$$I_{MC} = \sum_i^n I_i.$$
(2.16)

The σ_{MC} uncertainty in I_{MC} is then given by

$$\sigma_{MC}^2 = \sum_i^n \frac{V_i}{N_i},$$
(2.17)

where

$$V_i = \tau_i^2 \left(\sum f_i^2 - \left(\sum f_i \right)^2 \right),$$
(2.18)

and τ_i, I_i, V_i, N_i are respectively the volume, integral, variance and number of sampled points of each sub-region. By choosing the sub-regions and the number of points in each, it is possible to optimize the accuracy of I_{MC} by reducing σ_{MC}^2.

2.5.2   Importance Sampling

Monte Carlo calculation can be performed by choosing random numbers from any arbitrary probability distribution. Often Monte Carlo calculations can be quite inefficient if we are to use a uniform distribution in the integration of more peaked or sloped functions since we would sample regions of phase space not necessarily contributing

much to the total integral. Instead of choosing points from a uniform distribution we can then choose a distribution which will concentrate the points where the function being integrated is large. Thus eq.2.11 can be rewritten as

$$I = \int_{x_1}^{x_2} \frac{f(x)}{u(x)} u(x) dx, \tag{2.19}$$

where the $u(x)$ is chosen to be a reasonable approximation to $f(x)$. The integral is then calculated by choosing points sampled from the probability distribution $u(x)$ and evaluating $f(x_i)/u(x_i)$ at these points. The average of these evaluations gives an estimate of I as

$$I_{MC} \quad \approx \quad (x_2 - x_1) \frac{1}{N} \sum_{i=1}^{N} \frac{f(x_i)}{u(x_i)}. \tag{2.20}$$

We can also choose to define $dU = u(x) dx$ and express the integral in eq.2.19 as

$$I = \int_{U_1}^{U_2} \frac{f(x(U))}{u(x(U))} dU, \tag{2.21}$$

where the limits of integration correspond to the change of variable. In this method we choose values for U randomly and uniformly in the range [0,1], we then invert for each value of the integral $x(U)$ and solve for x to finally evaluate $\frac{f(x(U))}{u(x(U))}$, the average of these evaluations gives an estimate of the integral in eq.2.21. If $u(x)$ has been chosen of similar shape to $f(x)$ the new integrand in eq.2.21 will be close to unity and its variance will be much smaller than that of $f(x)$.

Several conditions need to apply for $u(x)$:

1. $u(x)$ is usually a probability distribution function normalized to unity and must be non-negative everywhere in the integration region.

2. The integral $U(x)$ should be known analytically. If $u(x)$ is a pdf normalized to unity, then $U(x)$ increases monotonically as a function of x, from zero to one.

3. Either $U(x)$ can be inverted or it is possible to generate random numbers with a distribution $u(x)$.

4. The ratio $\frac{f(x)}{u(x)}$ needs to be as close as possible to unity thus giving the smallest possible value for the variance.

Although importance sampling is a widely used technique to reduce the variance it

has some drawbacks. First $u(x)$ needs to be integrable and analytically invertable and there are simply not many such functions. The inversion can be done numerically, but this is usually slow and sometimes inaccurate. Second multidimensional importance sampling is difficult to handle except for the simplest functions and except one dimension at a time. Third $u(x)$ should not go to zero in the integration region since the variance then becomes infinite(unless $f(x)$ also goes to zero in the same way).

Variance reduction techniques are essential for making a Monte Carlo calculation really efficient. Without them the convergence of Monte Carlo integrals will be too slow and not very useful. In many dimensions the benefit of variance reduction is even greater since the reduction factor in number of points to be sampled multiplies for each new dimension.

2.6   Conclusion

In this chapter we have shown the main advantages of using Monte Carlo methods in event generators such as HERWIG. In the next chapter we will give a more detailed overview of how these techniques are used in QCD event generation.

Chapter 3

Event generators

3.1   Introduction

In this chapter we will give a brief overview of the main physics and methods used in HERWIG [19] to simulate a collision between two hadrons with large momentum transfer. We first present a brief theoretical description of high transverse momentum interactions in hadron-hadron collisions and give the expression of the leading order inclusive jet cross-section. We then present an overview of the initial and final state parton shower algorithms implemented in HERWIG and discuss some key features of the model such as colour coherence and hadronisation. Finally we present a time line of an event generation in HERWIG leading to a complete event simulation of a hadron-hadron interaction with high momentum transfer.

3.2   Hadron-Hadron interactions
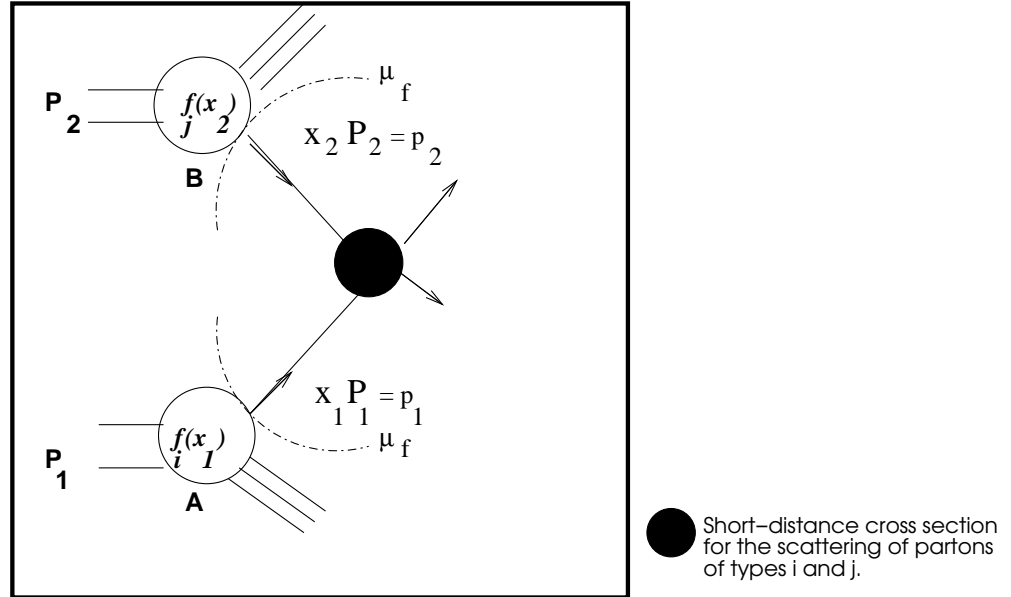
Figure 3.1: The parton model description of a hard scattering process

A high-energy interaction between two hadrons is described by the QCD improved parton model [2]. The model describes the interaction between the two incoming hadrons

as the interaction between their constituent partons (quarks and gluons). Partons with momenta p_1, p_2, as shown in fig.3.1, inside each incoming hadron (A, B with momenta P_1 and P_2) are distributed through parton distribution functions $f_{A,i}(x_1, \mu_f^2)$ and $f_{B,j}(x_2, \mu_f^2)$. Each parton distribution function $f_{A,i}(x_1, \mu_f^2)$ and $f_{B,j}(x_2, \mu_f^2)$ is obtained from QCD fits to the entire deep inelastic scattering data-set (as explained in Chapter 1.2.6) and subsequently evolved using the DGLAP equations (with a particular value of $\Lambda_{\overline{MS}}$) up to a factorization scale μ_f^2. The cross section for a hard scattering process between two hadrons (A, B) with four-momenta P_1 and P_2 can be written as

$$\sigma(P_1, P_2) = \sum_{i,j} \int dx_1 dx_2 f_{A,i}(x_1, \mu_f^2) f_{B,j}(x_2, \mu_f^2) \hat{\sigma}_{i,j}(p_1, p_2, \alpha_s(\mu_f^2), Q^2/\mu_f^2), \qquad (3.1)$$

where $p_1 = x_1 P_1$ and $p_2 = x_2 P_2$ are the momenta of the partons involved in the hard interaction at some scale Q, $\alpha_s(\mu_f^2)$ is the value of the strong coupling constant at the factorization scale μ_f^2 and $\hat{\sigma}_{i,j}$ is the short distance cross section for the scattering of two incoming partons i and j. At high energy scale of interaction ($Q > 1$ GeV) due to the asymptotic property of QCD, the strong coupling α_s is small and the short-distance cross section can be calculated perturbatively and expressed as a power series in the running coupling $\alpha_s(\mu_R^2)$ function of the renormalization scale μ_R^2 as

$$\hat{\sigma}_{i,j} = \sum_{n=n_0}^{\infty} \left(\frac{\alpha_s(\mu_R^2)}{\pi} \right)^n \hat{\sigma}_{i,j}^{(n)} \left(p_1, p_2, \frac{Q^2}{\mu_f^2}, \frac{Q^2}{\mu_R^2} \right), \qquad (3.2)$$

where $n_0 = 2$ for a two-to-two hard subprocess. In the leading order approximation the short distance cross section $\hat{\sigma}_{ij}$ in eq.3.2 is identical to the Born cross-section $\hat{\sigma}_{ij}^{(0)}$. In higher orders the perturbative parton scattering cross-section contains long distance interaction terms which are factorised into the parton distribution functions and absorbed into the description of the incoming hadrons. In this way the remaining hard part of the interaction with high momentum transfer is insensitive to the physics of the low momentum scale and allows the short distance cross section not to depend on the details of the hadron wave function or the type of the incoming hadron. This separation of the hard part of the cross section from the low momentum physics is known as factorization and has been proven to all orders in perturbation theory [20]

*.

The separation between the long and short distance interactions is determined by the parameter μ_f, the factorization scale. A parton emitted with transverse momentum below μ_f is considered as part of the hadron and is absorbed in the parton distribution. A parton with transverse momentum above μ_f is considered as part of the perturbative interactions. For convenience it is usual to choose the factorization and the renormalization scale equal to the scale of interaction Q. This however does not need to be the case, the three scales are in principle independent.

The main theoretical justification for QCD Monte Carlo simulations lies in the factorization theorem. Without the factorization theorem it would be too difficult to construct an efficient algorithm. The factorization theorem greatly simplifies the algorithm by factorizing probabilities for separate parts of the event. It is then possible to simulate an event knowing its initial condition, step by step using a sequential Monte Carlo simulation. In HERWIG this particular method is used both with the parton shower formalism (see below) and the hadronisation model.

We will now turn our attention to the particular subprocess used in HERWIG to simulate jet production in hadron-hadron collisions.

3.2.1   The inclusive jet cross section in LO approximation

In two to two parton-parton subprocesses the two incoming partons, with negligible transverse momenta, interact at some scale Q to produce two final state outgoing partons, each with transverse momentum $p_t \approx Q$. Due to momentum conservation the two outgoing partons are produced with equal and opposite momenta in the subprocess centre-of-mass frame. If only two partons are produced, and the relatively small transverse momentum of the incoming partons is neglected, the two outgoing partons will give rise to two jets of particles, back-to-back in azimuthal angle and balanced in transverse momentum in the laboratory frame.

---

*Violations of factorization are expected to be suppressed by inverse powers of Q^2

To write the two jet cross-section we start first by writing down the cross-section for two to two parton-parton scattering subprocesses. In the massless limit we label the two to two parton-parton scattering as

$$parton_i + parton_j \rightarrow parton_k + parton_l, \tag{3.3}$$

and we define the Mandelstam variables as $\hat{s} = (p_i + p_j)^2$, $\hat{t} = (p_i - p_k)^2$ and $\hat{u} = (p_j - p_k)^2$ with p_i, p_j, p_k, p_l being respectively i, j, k, l parton four momenta.

The scattering cross-section for two to two parton-parton scattering in their centre of mass frame can be written as

$$\frac{d\hat{\sigma}_{i,j \rightarrow k,l}^{QCD}(\hat{s}, \hat{t})}{d\cos(\hat{\theta}_{CM})} = \frac{1}{2\hat{s}} \frac{1}{16\pi} \overline{\sum} |\mathcal{A}|^2 \tag{3.4}$$

where $\mid \mathcal{A} \mid^2$ represent leading order matrix elements squared for two to two parton-parton scattering subprocess and $\overline{\sum}$ denotes the average and sum over initial and final state spins and colours respectively.

We give below expressions for the LO matrix elements squared [21, 22] used in eq.3.4.

- $qq' \rightarrow qq'$

$$\alpha_s^2 \left[\frac{4}{9} \frac{\hat{s}^2 + \hat{u}^2}{\hat{t}^2} \right] \tag{3.5}$$

- $qq \rightarrow qq$

$$\alpha_s^2 \left[\frac{4}{9} \left(\frac{\hat{s}^2 + \hat{u}^2}{\hat{t}^2} + \frac{\hat{s}^2 + \hat{t}^2}{\hat{u}^2} \right) - \frac{8}{27} \frac{\hat{s}^2}{\hat{u}\hat{t}} \right] \tag{3.6}$$

- $q\overline{q} \rightarrow q'\overline{q}'$

$$\alpha_s^2 \left[\frac{4}{9} \frac{\hat{t}^2 + \hat{u}^2}{\hat{s}^2} \right] \tag{3.7}$$

- $q\overline{q} \rightarrow q\overline{q}$

$$\alpha_s^2 \left[\frac{4}{9} \left(\frac{\hat{s}^2 + \hat{u}^2}{\hat{t}^2} + \frac{\hat{t}^2 + \hat{u}^2}{\hat{s}^2} \right) - \frac{8}{27} \frac{\hat{u}^2}{\hat{s}\hat{t}} \right] \tag{3.8}$$

- $q\overline{q} \rightarrow gg$

$$\alpha_s^2 \left[\frac{32}{27} \frac{\hat{t}^2 + \hat{u}^2}{\hat{t}\hat{u}} - \frac{8}{3} \frac{\hat{t}^2 + \hat{u}^2}{\hat{s}^2} \right] \tag{3.9}$$

- $gg \to q\overline{q}$

$$\alpha_s^2 \left[\frac{1}{6} \frac{\hat{t}^2 + \hat{u}^2}{\hat{t}\hat{u}} - \frac{3}{8} \frac{\hat{t}^2 + \hat{u}^2}{\hat{s}^2} \right] \tag{3.10}$$

- $gq \to gq$

$$\alpha_s^2 \left[-\frac{4}{9} \frac{\hat{s}^2 + \hat{u}^2}{\hat{s}\hat{u}} + \frac{\hat{u}^2 + \hat{s}^2}{\hat{t}^2} \right] \tag{3.11}$$

- $gg \to gg$

$$\alpha_s^2 \left[\frac{9}{2} \left(3 - \frac{\hat{t}\hat{u}}{\hat{s}^2} - \frac{\hat{s}\hat{u}}{\hat{t}^2} - \frac{\hat{s}\hat{t}}{\hat{u}^2} \right) \right] \tag{3.12}$$

The triple differential inclusive two-jet cross section for hadronic interactions can be written as

$$\frac{d\sigma^{hard}(s)}{dx_1 dx_2 d\hat{t}} = \sum_{i,j,k,l} \frac{1}{1 + \delta_{k,l}} f_{A,i}(x_1, \mu^2) f_{B,j}(x_2, \mu^2) \frac{d\hat{\sigma}_{i,j \to k,l}^{QCD}(\hat{s}, \hat{t})}{d\hat{t}}, \tag{3.13}$$

since

$$\hat{t} = \frac{-\hat{s}(1 - \cos(\hat{\theta}_{CM}))}{2}, \tag{3.14}$$

where

$$\frac{d\sigma_{i,j \to k,l}^{QCD}(\hat{s}, \hat{t})}{d\hat{t}} = \frac{\pi}{\hat{s}^2} \overline{\sum} |\mathcal{A}|^2, \tag{3.15}$$

and μ^2 is set equal to Q^2 (the scale of interaction). The two-jet cross section in eq.3.13 is written as a sum of terms each representing a particular combination of initial (i, j) and final (k, l) state partons. We note that the relative importance of each subprocess in the calculation of the inclusive two-jet cross section is dominated by processes involving gluons because of their large colour charge.

HERWIG estimates the total cross section for hadronic interactions involving transverse momenta greater than a certain cutoff $(p_{tmin} \gg \Lambda_{QCD})$ by Monte Carlo integration of the integral

$$\sigma^{hard}(s, p_{tmin}) = \int_{p_{tmin}^2}^{s/4} dp_t^2 \int \frac{d\sigma^{hard}(s)}{dx_1 dx_2 dp_t^2} dx_1 dx_2, \tag{3.16}$$

where p_t is the transverse momentum of the outgoing partons. The p_{tmin} cutoff in the integral in eq.3.16 is necessary since in the limit $p_t \to 0$ the perturbative cross-section diverges.

3.3 Final and Initial state parton showers

In a semi-classical picture partons involved in the hard scattering undergo a phase of acceleration or deceleration in which they might radiate coloured gluons. The parton radiation needs to be taken into account in the calculation of the cross section. In principle the cross section for hard scattering could be calculated to all orders using perturbative QCD, although the complete perturbative calculations have been completed only to next-to-leading order. Nevertheless it is possible to calculate a correction to the leading order cross section, to all orders, for partons emitted in the soft and collinear limit. This is possible since the divergences encountered in the integral for soft and collinear partons cancel with appropriate virtual loop diagrams leaving us with a finite result (see comment on page 30). However because of kinematic constraints the cancellation is not perfect and the final result will include large logarithms which will dominate the cross section. If we keep only the leading logarithmic terms (the Leading Logarithmic Approximation, LLA) the final result will be in a factorised form, where the original cross-section is convoluted with process independent splitting functions. Because splitting functions are process independent any subsequent emissions can be repeated in the same way as the first one with the upper scale of each new emission set by the scale of the previous. In this way emissions follow a semi-classical time-ordered picture with the time scale of each new emission longer than the previous one. Algorithms which simulate such emissions in QCD are called "parton shower" algorithms.

3.3.1   Final State Parton Shower

In this section we describe the parton shower procedure used in the HERWIG Monte Carlo [23, 24, 25] event generator.

We define DGLAP splitting functions $D_{a/b}(z, Q^2)$ in eqs.2.17-2.20 as representing the momentum fraction distribution of parton b inside parton a as a function of the energy fraction z carried by the observed parton and the momentum scale Q of observation.

$$D_{g/q}(z, Q^2)dzdQ^2 \;\; = \;\; \frac{C_F \alpha_s}{2\pi} \frac{dQ^2}{Q^2} \frac{dz}{z} \left(1 + (1-z)^2 \right), \tag{3.17}$$

$$D_{q/q}(z, Q^2)dzdQ^2 \;\; = \;\; \frac{C_F \alpha_s}{2\pi} \frac{dQ^2}{Q^2} \frac{dz}{(1-z)} \left(1 + z^2 \right), \tag{3.18}$$

$$D_{q/g}(z, Q^2)dzdQ^2 \;\; = \;\; \frac{T_R \alpha_s}{2\pi} \frac{dQ^2}{Q^2} dz \left(z^2 + (1-z)^2 \right), \tag{3.19}$$

$$D_{g/g}(z, Q^2)dzdQ^2 \;\; = \;\; \frac{N_C \alpha_s}{2\pi} \frac{dQ^2}{Q^2} \frac{dz}{z(1-z)} \left(1 - 2z(1-z) + z^2(1-z)^2 \right), \tag{3.20}$$

where $C_F = (N_C^2 - 1)/(2N_C)$ and $T_R = \frac{1}{2}$ with $N_C = 3$ colours and N_f the number of flavours which varies with the scale. The four DGLAP component from above may be written in a more general form as

$$D_{a/b}(z, Q^2)dQ^2 = \frac{C \alpha_s}{2\pi} \frac{dQ^2}{Q^2} P_{a/b}(z), \tag{3.21}$$

where $P_{a/b}(z)$, the splitting function, represents the probability distribution for finding parton a inside parton b. In the Monte Carlo implementation of branching the cancellation between the divergent part of the splitting function and the virtual loop diagrams is handled by the introduction of a resolution scale parameter Q_c^2 below which any branching is indistinguishable from no branching at all. In HERWIG the resolution branching scale is chosen to be equal to the hadronisation scale. By considering the conservation of probability (the sum of branching plus no-brunching probabilities is one at each vertex) the cancellation of divergences is handled implicitly since both the probability for emission and no emission is finite.

We can write a probability that a parton of type b carrying energy fraction z, $0 < z_1(Q^2, Q_c^2) < z < z_2(Q^2, Q_c^2) < 1$ at some scale Q^2 will not radiate another parton before

reaching the resolution infrared cut-off scale Q_c^2, as one minus the n-emission proba-
bilities summed over all $n > 0$. The probability of nonemission $\Delta_b(Q^2, Q_c^2)$ (known as
the Sudakov form factor [26]) in the same interval can then be written as

$$\Delta_b(Q^2, Q_c^2) = \exp\left(-\sum_a \int_{Q_c^2}^{Q^2} \frac{dk^2}{k^2} \int_{z_1}^{z_2} dz \frac{C\alpha_s}{2\pi} P_{a/b}(z)\right). \tag{3.22}$$

Thus the probability distribution for the first branching below scale Q_{max}^2 to be at
scale Q^2 is

$$dP(Q^2; Q_{max}^2, Q_c^2) = \sum_a \frac{dQ^2}{Q^2} \int_{z_1}^{z_2} dz \frac{C\alpha_s}{2\pi} P_{a/b}(z) \Delta_b(Q_{max}^2, Q^2). \tag{3.23}$$

We can then choose the value of Q^2 from the distribution in eq.3.23 by inverting its
integral (giving us precisely the form factor in eq.3.22) and solving

$$\Delta_b(Q_{max}^2, Q^2) = r, \tag{3.24}$$

in Q^2 corresponding to the emission of parton at scale Q^2 above cutoff scale $Q_c^2 \gg$
$\Lambda_{\overline{MS}}$, if the parton is emitted below the cutoff scale, the branching is terminated (since
this correspond to no resolvable emission). This procedure is recursively applied to
each of the outgoing partons with the upper scale set equal to Q^2.

The algorithm constructed according to the above prescription correctly treats
all leading collinear logarithms (from the $\frac{dQ^2}{Q^2}$ term), but large logarithms come also
from the $\frac{dz}{z}$ term. They correspond to the emission of soft gluons which may not be
necessary collinear (i.e. partons with momentum small compared with the scale Q
but still large compared with the QCD scale $\Lambda_{\overline{MS}}$). In [27] it was shown that the soft
gluons are actually emitted coherently in an angular ordered manner. This property
is due to the strongly destructive interference between different configurations of soft
gluons contributing to the same final states. After these contributions are averaged
over azimuthal orientations they will interfere in a completely destructive manner,
leading to large angle emissions from the parent partons and small angle emissions
from the split pairs (i.e the angle between the two emitted partons is smaller than
that of the previous branching) [25, 27].

In HERWIG the coherence of emitted soft gluons is introduced by the ordering of scale Q^2 through

$$Q^2 = E^2 \epsilon, \tag{3.25}$$

where $\epsilon = q_i \cdot q_j / E_i E j \approx 1 - cos\theta_{i,j}$ is the angular variable. Thus the ordering of Q^2 scale will correspond to coherent angular ordered, emissions.

In the parton showering algorithm the energy fraction z is defined as the energy fraction between the upper limit of the successive emission $Q^2_{max,i} = z_i^2 Q^2$ and the infrared cutoff. Thus the energy fraction of a branching is defined as,

$$
\begin{aligned}
z &> z_1 = Q_{0i}/Q, \\
z &< z_2 = 1 - Q_{0j}/Q, \\
Q^2 &> Q_c^2 = (Q_{0i} + Q_{0j})^2.
\end{aligned}
\tag{3.26}
$$

where the partons i and j are allowed to have different infrared cutoffs.

The full leading logarithmic coherent parton showering algorithms in HERWIG also treats correctly correlations in azimuth of the gluon emission (i.e determines correctly the azimuthal angle distribution of gluon emissions to leading infrared order), due to their spin (the splitting functions above are averaged over spin and azimuth) and due to coherence (the angular ordered implementation of coherence is exact only in the azimuthally averaged case). It sums correctly single logarithmic and double logarithmic terms associated with soft emission and thus should correctly describes parton distributions to leading infrared order and intra-jet distributions.

3.3.2 Initial State Parton Shower

The structure of the shower is essentially the same as in the final state process although the initial state parton shower works its way backward [30], starting from the hard process and working back toward the on-shell incoming parton [25], with the scale decreasing at each step. The correct prescription takes into account the parton density functions $f(x_{k-1}, Q_k)$ for choosing a parton at the next scale Q_k (where k is the kth

emission counting from the hard subprocess). The probability of backward evolution for a parton without branching between (Q_{k-1}, x_{k-1}) and (Q_k, x_{k-1}) is given by

$$\Delta(Q_k, Q_{k-1}; x_{k-1}) = \frac{f(x_{k-1}, Q_k)}{\Delta(Q_k)} \frac{\Delta(Q_{k-1})}{f(x_{k-1}, Q_{k-1})}, \qquad (3.27)$$

with $P(z_k)$ replaced by

$$P(z_k) \to f\left(\frac{x_{k-1}}{z_k}, Q_k\right) P(z_k). \qquad (3.28)$$

Thus instead of the Sudakov form factor $\Delta(Q_k)$ a modified Sudakov form factor is used $\Delta(Q_k)/f(x, Q_k)$. The value of Q_k and energy fraction is then chosen by inverting the modified form factor in eq.3.27 and solving eq.3.29

$$\Delta(Q_k, Q_{k-1}; x_k) = r. \qquad (3.29)$$

The lower and upper limit on z are chosen between $x_{k-1} < z_k < 1 - Q_0/Q_k$ to keep x_k below 1 and z below the infrared cutoff. If Q_k is less than some scale Q_{cut} (at which the parton distribution functions have been measured or evolved to) the emission is terminated with $k - 1$ emissions. Usually the Q_{cut} scale is different from the infrared cutoff scale Q_c. If the evolution has not been terminated a new value for z is chosen and the above procedure is repeated. Once the Q_{cut} scale or the infrared cutoff scale is reached the emitted partons produce final state parton showers with their upper scale given by Q_k. If the backward evolving parton is not a valence quark it is forced to be evolved back to a gluon and a valence quark. The presence of structure functions in eq.3.27 for each parton type is to enforce the correct development of the backward parton shower evolution. In the large x limit this coherent initial state branching algorithm correctly sums not only leading but also the next-to-leading logarithmic contributions.

3.3.3   Hadronisation Process

Using the parton shower formalism described in the previous two sections the outgoing partons are evolved in energy through successive parton emissions until they reach a typical low energy scale ≈ 1 GeV known as the hadronisation scale Q_0. At this scale

long distance effects of non-perturbative nature become important. One of these effects is the conversion of outgoing partons into observed hadrons. Since the hadronisation scale is low compared to the scale of the hard interaction, the evolving partons have had a long time to branch into new ones before reaching it. One property of parton showers is to tend to inhibit the separation of the colour charges forming a singlet. This preconfinement effect of parton showers causes emitted partons to end up close in momentum space to their respective opposite colour (anticolour) partners [31, 32]. Although perturbative QCD does not give any information about the confinement phase of partons the two partons forming the colour singlet entity can be converted locally in phase space into hadrons at the hadronisation scale Q_0 independently of the hard interaction scale Q (for large Q). This local conversion of partons into hadrons (i.e. hadrons will inherit their momentum and space-time structure as well quantum numbers from partons locally) is named Local Parton Hadron Duality. A consequence of LPHD is that, if gluon emission is treated correctly, a simple hadronisation model should be enough to explain the experimental data.

HERWIG implements the hadronisation phase through the cluster model [25, 24]. The cluster model uses the property of preconfinement of colour due to parton branching processes. Once the outgoing gluons from the parton shower have reached the hadronisation scale, they are split non-perturbatively into $q\overline{q}$ pairs. Neighbouring (in colour) quarks and antiquarks are then combined into singlet clusters. The cluster mass distribution falls rapidly at high mass. Each cluster is decayed into a pair of hadrons, with branching ratios determined simply by density of states. The advantage of combining the non-perturbative hadronisation model with the perturbative parton shower algorithm is to have a realistic model for event generation which could be compared directly with the experimental data.

3.4 Event Generators

An event generator is a program designed to simulate a given physical process. An event generator based on Monte Carlo methods in particle physics is particularly suitable since it mimics the inherent randomness of the natural process and allows us to make a direct comparison between simulated phase-space points and real events. Monte Carlo models are widely used today in particle physics experiments as tools in data analysis.

3.4.1 Event generation

Each event or each specific physical process (with its set of phase space points) carries with it a probability with which it should happen. The probability is just a weight in the overall integral of the ensemble of events. Generating events with different weights would be inefficient since we would also generate events with low weight thus contributing very little to the bulk of the processes. In HERWIG a rejection technique is used for generating events with the same weight (i.e. unweighted events), thus reducing the variance to zero. This is done by finding a maximum weight W_{max} by a Monte Carlo search of the phase-space in the first instance, followed by a test of whether to keep or reject each event with the probability W/W_{max}. All accepted events are then given a weight $\overline{W}$, calculated from the Monte Carlo integral over all the generated events (not just the accepted ones). Although HERWIG is a general purpose event generator, in this thesis we will really concentrate on one particular subprocess the hard two to two parton-parton scattering [33].

3.4.2   Event generation description

Initialization

HERWIG starts first by checking the input parameters and calculates the values for parameter dependent variables (for example computes look-up tables of Sudakov form factors for the evolution of initial and final-state parton showers). Then a number of phase space points are generated and the maximum weight in the phase space is determined. Subsequently an estimate of the cross section for the selected process is given.

Hard Subprocess Generation

For each hard subprocess a specific subroutine is called twice. In the first call a phase space point is generated and the corresponding weight in the integral calculated. If the event is accepted (using the rejection technique) a second call determines the structure of the hard subprocess corresponding to the phase space point. It calculates values for parton momenta, identifies colour connections in the hard subprocess, sets up colour structure labels and various other pointers and spin vectors needed by later stages of processing.

Parton Evolution

Initial and final state partons are evolved through perturbative branching, emitted outgoing partons are then evolved in turn until they reach the hadronisation scale.

Hadronization

Once the parton shower phase is over all the outgoing partons are converted into hadrons locally in phase space since the confinement phase is considered as local in colour and independent of the hard scale of interaction. Hadrons then inherit their momentum and space-time structure from partons as well as quantum numbers which are also transferred locally. All the outgoing gluons are split non-perturbatively into quark-antiquark pairs, and through the planar approximation † each outgoing parton is connected to its colour partner with which it forms a colour-singlet cluster. Clusters

---

†That is, to leading order in $1/N$ where N is the number of colours.

have distributions of mass and spatial size that peak at low values, fall rapidly for large cluster masses and sizes, and are independent of the hard subprocess scale. Finally clusters are fragmented into hadrons on a phase space basis.

Particle Decays

The unstable hadrons produced after cluster hadronisation go through a secondary decay. This is done through experimentally measured decay branching fractions based on phase space arguments. Any quarks or gluons produced at this stage are evolved and hadronised as above.

Underlying soft event

In hadron-hadron interactions (or hadron-lepton) the hard scattering is accompanied by the two hadron remnants. The two remnants contain the spectators from the two incoming hadrons which are colour connected to the parton showers. The underlying soft event is modeled then as a soft collision between these two beam clusters. The model is based on a parametrisation of the minimum-bias $p\overline{p}$ event generator of the UA5 collaboration [34] modified for the use of the cluster fragmentation algorithm. The model starts from the parametrisation of the $p\overline{p}$ inelastic charged multiplicity distribution according to which clusters are produced and hadronised. The same hadronisation model is used for clusters coming from both the 'soft' interactions and those coming from parton branching. The cluster momenta are generated from simple phase-space distributions.

3.5   Conclusion

In this chapter we have presented an overview of the main theoretical features implemented within the HERWIG program for jet event simulation. In the next chapter we will turn our attention to testing how well HERWIG describes the growth and development of charged particle jets produced in $p\overline{p}$ interactions. We will be particularly interested in testing whether HERWIG correctly describes particle distributions away from the leading jet (i.e. in the interjet region).

Chapter 4

Jet physics and the underlying event

4.1   Introduction

We begin this chapter by giving an overview of the main kinematic variables used to describe final state particles followed by the definition of a jet of particles produced in high energy collisions. We briefly discuss the importance of determining the value of the underlying event activity in jet measurements. The underlying event is an interesting object which is difficult to model since it involves a mix of both non-perturbative and perturbative physics. We adopt a simple jet definition and present the analysis of the charged particle component of jets simulated by HERWIG in three different topological regions. For hard scattering proton-antiproton collisions we simulate the underlying event activity in each region using HERWIG's Underlying Event model. Finally we compare the experimental analysis of the underlying event [35] with theoretical simulated data using HERWIG's Underlying Event model for both low p_t<50 GeV and high 50 GeV $< p_t <$ 300 GeV jets in two separate analyses. We thus independently confirm the results obtained by the CDF collaboration [35].

4.2   Kinematic variables

The scattering of two hadrons can be seen as the scattering of two incoming beams of partons each having a spectrum of longitudinal momenta determined by the parton distribution functions. The CM of the two colliding partons is usually boosted relative to that of the two incoming hadrons and connected to the momentum fractions of the two hadrons carried by the colliding partons. For reasons of convenience, final states should then be expressed in terms of variables which transform simply under longitudinal boosts. In this respect the kinematics of final states are most suitably described by the following set of variables; the transverse momentum p_t, the rapidity y and the azimuthal angle ϕ. Using these three variables the four-momentum of a particle of mass m can be expressed as

$$P^\mu \;\; = \;\; (E, p_x, p_y, p_z),$$

$$= \quad (m_t \cosh y, p_t \sin \phi, p_t \cos \phi, m_t \sinh y), \tag{4.1}$$

with the transverse mass $m_t = \sqrt{p_t^2 + m^2}$.

The particle rapidity y, which is additive under boosts along the z direction, is defined as

$$y = \frac{1}{2} \ln \left(\frac{E + p_z}{E - p_z} \right), \tag{4.2}$$

with rapidity differences being boost invariant. The pseudorapidity of the particle is defined as

$$\eta = -\ln \tan \left(\frac{\theta}{2} \right), \tag{4.3}$$

and in the $m{\to}0$ limit is identical to its rapidity. From the experimental point of view pseudorapidity is more convenient than the rapidity since the angle θ (shown in fig.4.1) of a particle is a directly measurable quantity in the detector.
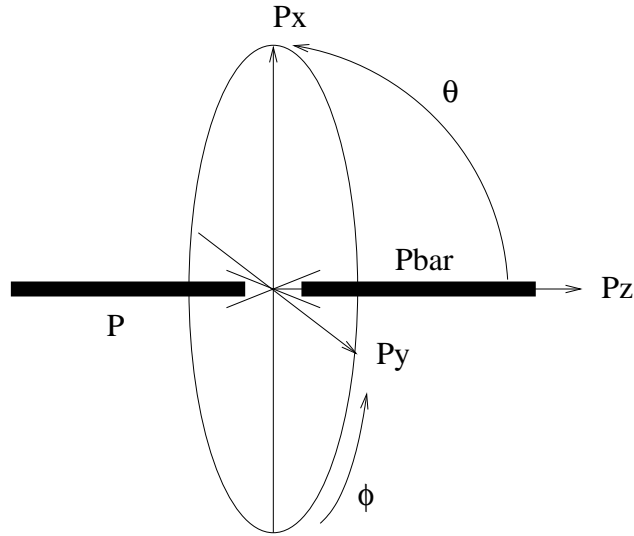
Figure 4.1: Coordinate system in the CM frame of the two incoming hadrons.

The transverse energy of a particle

$$E_t = E \sin \theta, \tag{4.4}$$

is also used in the experiment since it is E_t and not the p_t of the particle which is measured in the hadron calorimeter. In our jet algorithms (see below) the values of

$\theta \in [0, \pi]$ and $\phi \in [0, 2\pi]$ are calculated according to

$$\theta = \arccos\left(\frac{p_z}{\sqrt{p_t^2 + p_z^2}}\right),$$

(4.5)

and

$$\phi = \arctan\left(\frac{p_y}{p_x}\right).$$

(4.6)

4.3   Jets

High transverse momentum jets are often produced in high energy collisions at current hadron-hadron and hadron-lepton colliders. Jet physics plays an important part in particle physics and jet production has been used to measure the running of the strong coupling constant α_s, to measure parton distribution functions and to search for new physics. Jets are composed of collimated beams of particles with large transverse momentum produced in high energy collisions. Jets are not considered as fundamental QCD objects, but nevertheless they are crucial if we are to learn something about the partons from hadronic final states. At the Fermilab collider jets are produced in a particular type of inelastic $p\bar{p}$ interactions. The inelastic interactions can be separated into single diffractive, double diffractive and non-diffractive. The non-diffractive collisions (sometimes called hard core interactions) characterize inelastic events in which both the proton and antiproton break up as shown in fig.4.2. One type of non-diffractive interactions is made of high p_t jet events originating from hard parton-parton interactions as shown in fig.4.2.a.

Jets in an experiment can be defined at two levels; calorimeter and particle. The particle level jet energy is defined by applying a cone clustering algorithm (see below) to final state particles before they reach the calorimeter material. At the calorimeter level, the particle jet energy after being corrected for systematic effects can be directly compared to Monte Carlo simulations. The overall correction to the raw jet energy
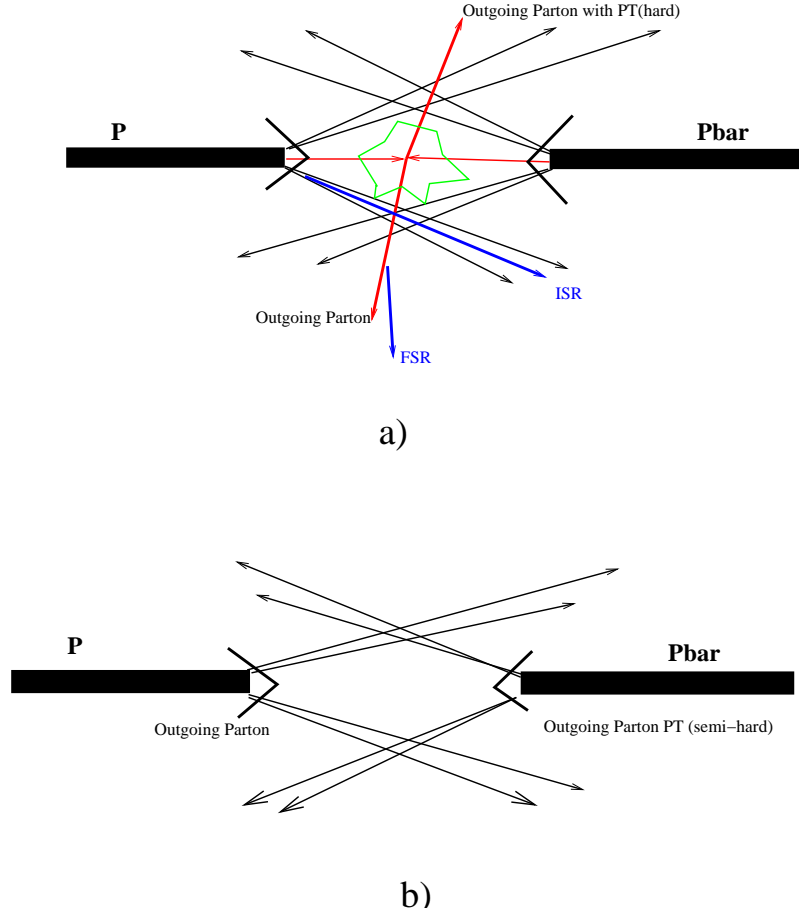
Figure 4.2: Illustrations of a) a hard subrocess occurring in a $p\overline{p}$ collision with remnant-remnant interactions and b) non-diffractive soft interaction in a $p\overline{p}$ collision.

such as; the effect of previous crossings (pile-up), contribution from additional $p\overline{p}$ interactions, noise from the radioactive decay of the uranium absorber and others (for a more complete overview on systematic effects see [36]) includes a correction due to the physics of the underlying event. The underlying event can be defined as the sum of all additional interactions not part of the main hard parton parton subprocess occurring between spectator constituents carrying the residual energy of the parent hadrons. For comparison between the experimental data and the perturbative QCD theoretical calculations to be valid the extra energy generated by these additional interactions needs to be subtracted from experimental jets (or added to the theoretical jets, but in practice the former is always done). In experiments the energy due to the underlying

event is determined by looking at the low luminosity minimum bias data triggering on inelastic non-diffractive collisions. At DØ [36] the energy E_{UE} to be subtracted from a jet, is given by

$$E_{UE} = D_{UE} A_{\eta,\phi} \tag{4.7}$$

where D_{UE} (GeV/ $\delta\eta\delta\phi$) is the density of energy due to the underlying event and $A_{\eta,\phi}$ is the area of the jet in $\eta - \phi$ space.

The uncertainty on the value of the underlying event activity at $\sqrt{s} = 1800$ GeV represent the largest experimental error (for both CDF and DØ) for jets with $E_t < 50$ GeV. The assumption that the underlying event is similar to the average energy found in minimum bias interactions used by most of the experimental collaboration needs to be reexamined. In [35] it is stated that the number of particles produced in the underlying event was a factor of two larger than in soft proton-antiproton collisions indicating that a greater activity is produced in remnant-remnant interactions than in soft proton-antiproton interactions.

From the theoretical point of view we expect hadronic final states to be strongly related to the physics at the parton level and a reliable jet definition is essential. For a jet definition to be valid two main constraints need to be satisfied:

1. The jet definition should be *collinear safe* i.e. it should be independent of a particle splitting into two parallel traveling partons which in theoretical calculations give rise to collinear divergences.

2. The jet definition should be *infrared safe* i.e. it should not depend on the emission of soft partons.

We mention that there are also experimental reasons for making the same requirements (i.e if two particles are too close together or if a particle has too low energy they cannot be reliably measured).

4.3.1   CDF and D∅ Cone Algorithms and jet definition

The cone jet algorithms are the type of algorithms usually used to study jets in hadron-hadron interactions. The cone jet algorithm builds a jet from its constituent particles according to the Snowmass accord [37]. The transverse energy, E_T, pseudorapidity, η, and azimuth, ϕ, of the jet are given by

$$E_{Tjet} = \sum_i E_{Ti} \tag{4.8}$$

$$\eta_{jet} = \sum_i \frac{E_{Ti}\eta_i}{E_{Tjet}} \tag{4.9}$$

$$\phi_{jet} = \sum_i \frac{E_{Ti}\phi_i}{E_{Tjet}} \tag{4.10}$$

where i runs over all the particles in the jet. The angle is the Lorentz-invariant opening angle $R_{ij} = \sqrt{(\eta_i - \eta_j)^2 + (\phi_i - \phi_j)^2}$. The energy of the jet will then be measured by the amount of transverse energy deposited in the angular region or "cone" of radius R_{ij} defined in ϕ, η space. In two dimensional η, ϕ plane, curves of constant R are circles around the axis of the jet.

The D∅ Jet Algorithm

The particles are clustered into jets according to the following steps [38]:

1. The particles are passed through a calorimeter with cell size $d_0 \times d_0$ in $\eta \times \phi$(in D∅, $d_0 = 0.1$).

2. Every calorimeter cell (cluster) with energy above E_0, is considered as a 'seed cell' for the following step (in D∅, $E_0 = 1$GeV).

3. A jet is defined by summing all cells within an angle R of the seed cell according to eq.4.8, eq.4.9 and eq.4.10.

4. If the jet direction does not coincide with the seed cell, step 3 is reiterated, replacing the seed cell by the current jet direction, until a stable jet direction is achieved.

5. We now have a long list of jets, one for each seed cell. Many are duplicates: these are thrown away.

6. Some jets may be overlapping. Any jet that has more than 50% of its energy in common with the higher-energy jet is merged with that jet: all the cells in the lower-energy jet are considered part of the higher energy jet, whose direction is again recalculated according to eq.4.8, eq.4.9 and eq.4.10.

7. Any jet that has less than 50% of its energy in common with a higher-energy jet is split from that jet: each cell is considered part only of the jet to which it is nearest. This is essentially the algorithm used by ZEUS(PUCELL), except that their merging/splitting threshold is 75% instead of 50%.

The CDF Jet Algorithm
This is essentially the same as in DØ case except for:

6. Any jet that has more than 75% of it's energy in common with the higher-energy jet is merged with that jet: all the cells in the lower-energy jet are considered part of the higher energy jet, whose direction is again recalculated according to the eq.4.8, eq.4.9 and eq.4.10.

7. Any jet that has less than 75% of its energy in common with a higher-energy jet is split from that jet: each cell is considered part only of the jet to which it is nearest. The directions of the two jets are then recalculated by iterating step 3.

Both of the above algorithms are considered as almost unsafe, i.e. one or both of the constraints stated above seems to be violated (although on closer inspection the iterative cone algorithm is safe) at the parton level despite being fully safe at the NLO level [38].

4.4 The Underlying event in Hard Scattering Processes

One of the first predictions of perturbative QCD is the appearance of jets with large transverse momentum. QCD also correctly describes the structure of radiation emitted within the cone around the jet axis i.e. the jet shape. QCD should also account for the radiation emitted outside the jet cone from the analysis based on the resummation of all leading infrared singular contributions, i.e. soft. The important property of resummation analysis shows that soft gluons interfere in such a way as to give coherent QCD radiation. The structure of QCD radiation outside the jet cone should then be particularly sensitive to the coherence property of the initial and final state radiation because of the important interference effects in this region.

The region outside the jet cone is also populated by radiation coming from interactions between the beam-beam remnants i.e. the underlying event. These remnant-remnant interactions are not very well known and because of the typically low Q scale of the interactions they cannot be modeled by standard perturbative QCD theory (in Chapter 5 we will however examine the possibility of additional multiple parton interactions contributing to the underlying event).

In this section we are going to closely examine the structure of events in which a hard scattering in a proton-antiproton collision has occurred. We will look at whether a proposed method of disentangling the two contributions from the soft underlying event and the perturbative part is really efficient and test whether HERWIG with its colour coherence effects gives a satisfactory description of the whole event structure.

In fig.4.2 we illustrate a QCD Monte-Carlo simulation of a proton-antiproton collision in which a parton-parton scattering with large transverse momentum has occurred. The simulated outgoing final state particles can be separated (according to the origin of their production) into two groups as shown in fig.4.2.a). The first group comes from outgoing partons, involved in the hard scattering, including initial and

final state radiation. The second group comes from particles originating in interactions between the two hadron remnants.

We define the underlying event as due to particles coming from all additional interactions that are not part of the main hard scattering (including initial and final state radiation). The two hadron remnants are just what is left after a parton has been knocked out from each of the two hadrons. Because of the soft scale of interactions it is not really known how additional interactions between the two remnants should be modeled. The soft underlying event model used in HERWIG, for example, is a parametrisation of the UA5 minimum bias data and is not based on any more fundamental physical assumptions.

Particles originating from the two outgoing hard partons will ultimately form two jets with large transverse momenta. In two-to-two hard parton parton interactions, the two jets are expected to be back-to-back in azimuthal angle.

In this section we will compare simulated data from the HERWIG Monte Carlo event generator (v5.9) with the experimental data coming from the study of the growth and structure of the underlying event measured at the CDF detector [35].

The overall CDF data are composed of two sets: the minimum bias set for which the minimum bias trigger selects predominantly the "hard core" component of the inelastic cross section and the JET20 (Calorimeter Tower cluster with $E_T > 20$GeV) set. To remain in the region where the charged particle tracks are found with high efficiency only the particles with ($p_t > 0.5$ GeV and $|\eta| < 1$) were considered. The experimental data were not corrected for the central tracking chamber (CTC) track finding efficiency but instead the theoretical Monte Carlo simulation data was. For theoretical simulations all parameters in HERWIG were set to their default values with $p_{tmin} = 3$ GeV. The value of p_{tmin} was set large enough for a perturbative QCD calculation to be applicable (since the perturbative QCD cross section diverges as $p_{tmin} \to 0$) and also large enough in order not to have our hard core inelastic cross section too high i.e. not greater than the measured total hard inelastic cross section. In the theoretical simulation particles were divided into two categories: particles arising from

the beam-beam remnants (those described as composing the underlying event) and particles originating from the hard scattering component (particles that result from the outgoing hard scattering jets plus initial and final-state radiation). The theoretical Monte-Carlo prediction was corrected for the track finding efficiency, which amounts to 8% and corresponds in removing 8 out of 100 charged particles on average from the theoretical prediction. Finally the data presented in the experimental work had an error of about 5% including both statistical and correlated systematic uncertainties.

4.4.1   Charged particle jet definition.

In this section we will repeat the analysis of the underlying event completed by the CDF collaboration presented in [35] in order to check the jet algorithms ready for further analysis presented in Chapters 5 and 6.

In this particular analysis [35] jets were defined as circular regions of radius $R = 0.7$ in $\eta - \phi$ space containing charged particles coming from both the underlying event and hard core interactions. Every charged particle in the event was assigned to a jet with a possibility that some jets might be composed of only one particle.
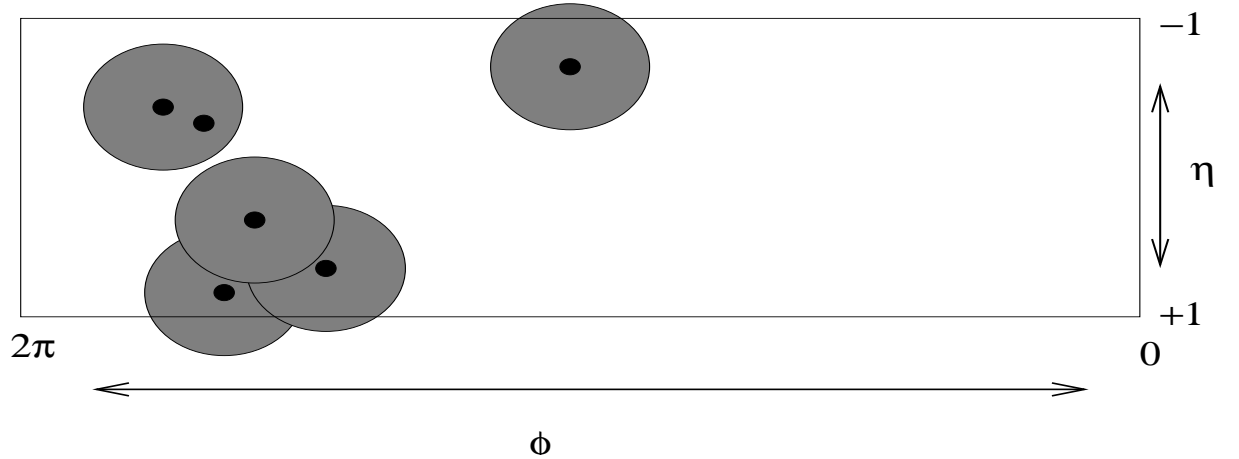
Figure 4.3: Event with six charged particles $p_t > 0.5$ GeV and $\eta < 1$ and five jets (radius in $\eta - \phi$ space $R = 0.7$).

Since the standard jet algorithm based on calorimeter clustering from Section

4.3.1 is not applicable at low transverse momentum, a very simple jet definition is used as described below :

- Charged particles are first ordered according to their p_t.

- Starting with the highest p_t particle, all particles within radius $R = 0.7$ are included to form a jet.

- Then we proceed to the next highest P_t particle (not already included in a jet) and include all particles within its radius $R = 0.7$ (not already included in a jet) to form a new jet.

- This is continued until all charged particles are part of one of the jets.

All charged particles with ($p_t > 0.5$ GeV and $|\eta| < 1$) are considered and the jet is allowed to extend outside $|\eta| < 1$. The transverse momentum of the jet is defined as the scalar p_t sum of all particles within the jet. Once all jets have been produced the one with the highest p_t(jet#1) is selected to be the leading jet. We calculate the ϕ of the leading jet following the definition given in Section 4.3.1,

$$\phi_{jet} = \sum_i \frac{p_{t_i} \phi_i}{p_{t_{jet}}} \qquad (4.11)$$

This simple charged particle jet definition is not infrared safe if applied at the parton level, however it can safely be used at the hadron level *, where the hadronic scale provides a cutoff.

4.4.2 Study of particle correlations in azimuthal angle

In this section we will use the simple jet algorithm presented in Section 4.4.1 in order to test whether HERWIG and its soft underlying event model correctly reproduce the particle distributions away in ϕ from the leading charged jet. There are three different regions of study (as shown in fig.4.4) separated in $\Delta\phi$ (i.e. the relative azimuthal

*Nevertheless results could be sensitive to soft hadron contributions

angle $\Delta\phi = \phi - \phi_{jet\#1}$ between charged particles and the direction of jet#1) from the leading p_t jet#1; the toward region defined over the range $|\Delta\phi| < 60°$ (this region includes particles of the leading jet#1), the away region defined over the range $|\Delta\phi| > 120°$ and the transverse region defined over the range $60° < |\Delta\phi| < 120°$. Each region, toward, transverse, and away covers the same range $|\Delta\eta| \times |\Delta\phi| = 2 \times 120°$. The transverse region, being perpendicular to the plane of the hard two-to-two scattering, is expected to be the most sensitive to particles produced in the underlying event and initial and final state radiation. In all our simulations we use typically 90 million events.
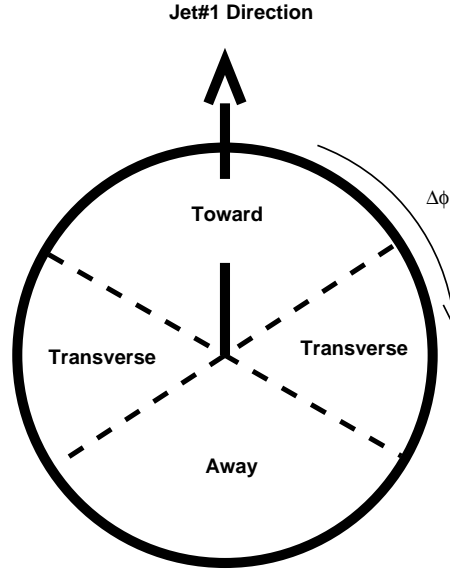
Figure 4.4: Toward, away and transverse regions from the leading in p_t jet (see [35]). The angle $\Delta\phi = \phi - \phi_{jet\#1}$ is the relative azimuthal angle between charged particles and the direction of jet#1.

The toward and the away regions

Fig.4.5 shows a fair agreement between the simulated and experimental data for the average total number of charged particles (including particles of the leading jet) as a function of the transverse momentum of the leading charged jet. We observe a rapid

rise in the overall number of charged particles at low jet#1 p_t followed by a flattening to a gradual rise at high p_t.

Figs.4.6 and 4.9 show a fair agreement between the experimental and simulated data for the toward region. The toward region is expected to be mainly populated by particles coming from the outgoing leading jet (jet#1) together with particles coming from the final and initial state radiation. The theoretical simulated data can be split into two different sets, particles originating from the remnant-remnant interactions and those from the hard scattering including initial and final state radiation, although there is no way of doing so in an experiment. It is clear from fig.4.6 that the main contribution in the toward region is due to particles from the main hard scattering. We notice that contributions to jets of up to 2 GeV come in equal proportions from both hard and soft processes meaning that jets can only be characterized as such once their transverse momentum is above 2 GeV.

In figs.4.7 and 4.10 we compare the experimental and the simulated data for the away region. This region contains particles coming from the recoiling side in ϕ of the leading jet (plus those from initial and final state radiation) together with the charged particles originating from the underlying event. Both the away and the toward region are dominated by the particles from the outgoing hard scattering jets although the away region contains a greater proportion of particles originating in remnant-remnant interactions.

The transverse region

In fig.4.8 we show the plot for the transverse region approximately perpendicular in ϕ to the plane of the two outgoing hard jets. From fig.4.8 we see that the charged particle activity in the transverse region forms an approximate plateau for jets with $p_t > 5$ GeV. We also notice that particles produced in remnant-remnant interactions form the main part of the activity for jets with $p_t < 15$ GeV and remain important for all p_t up to 50 GeV. This indicates that the transverse region is the most sensitive region
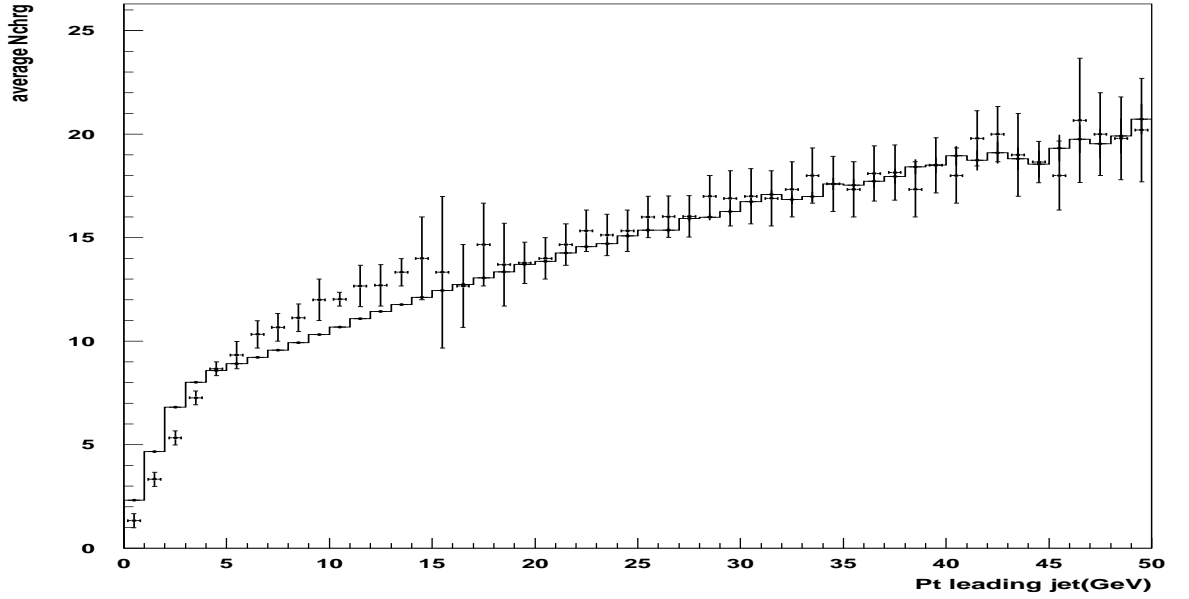
Figure 4.5: The average total number of charged particles in the event as a function of P_t (leading charged jet). HERWIG + Underlying Event model (solid line) simulated data, experimental CDF data [35] (data points).

to the underlying event activity (as shown in fig.4.8). Compared to the experimental data the HERWIG Underlying Event model fails to produce enough activity for both the average number of charged particles and the average scalar p_t and in addition has a wrong (too steep) p_t dependence as shown in figs.4.8 and 4.11.

4.4.3   Minimum-maximum region analysis

We now split the transverse region into two parts as shown in fig.4.12 [35]. The aim is to identify observables that are most sensitive either to the hard perturbative or the soft underlying components. On an event-by-event basis the two transverse parts are defined as the transverse Maximum part and the transverse Minimum part containing respectively the maximum and minimum activity in the transverse region. The Max part is expected to be more sensitive to the perturbative part of the total radiation while the Min part is expected to be more sensitive to the radiation coming from the
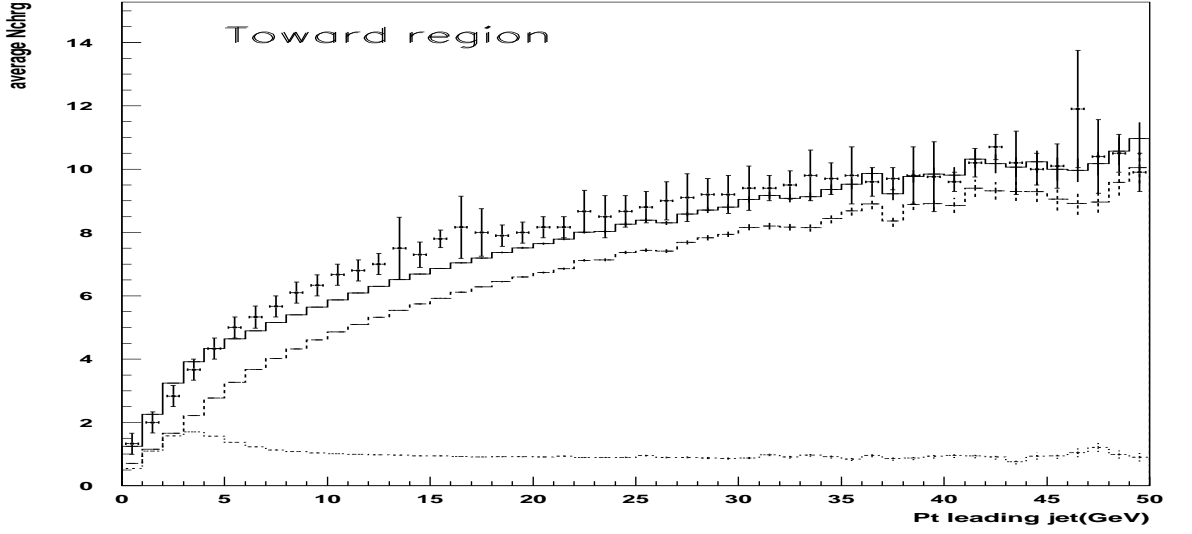
Figure 4.6: The average number of charged particles as a function of P_t (leading charged jet) in the toward region. HERWIG + Underlying Event model (solid line) simulated data, experimental CDF data [35] (data points). Charged particles arising from the break-up of the beam and target (dotted line) and charged particles that result from the outgoing jets initial and final-state radiation (dotted dashed line) are shown separately.

Figure 4.7: The average number of charged particles as a function of P_t (leading charged jet) in the away region. HERWIG + Underlying Event model solid line simulated data, experimental CDF data [35] (data points). Charged particles arising from the break-up of the beam and target (dotted line) and charged particles that result from the outgoing jets initial and final-state radiation (dotted dashed line) are shown separately.

Figure 4.8: The average number of charged particles as a function of P_t (leading charged jet) in the transverse region. HERWIG + Underlying Event model solid line simulated data, experimental CDF data [35] (data points). Charged particles arising from the break-up of the beam and target (dotted line) and charged particles that result from the outgoing jets initial and final-state radiation (dotted dashed line) are shown separately.
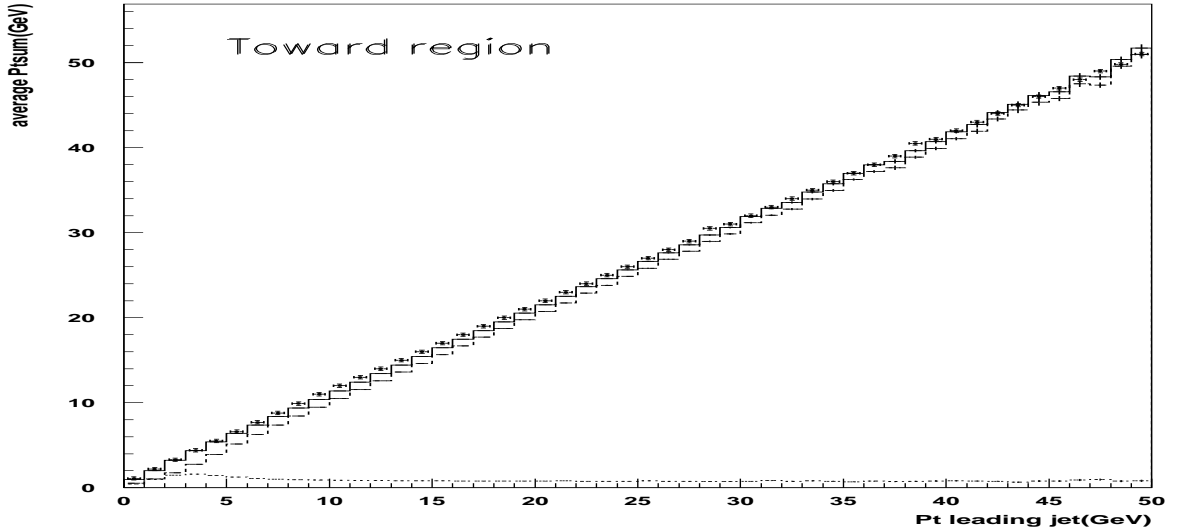
Figure 4.9: The average P_t sum of charged particles as a function of P_t (leading charged jet) in the toward region. HERWIG + Underlying Event solid line simulated data, experimental CDF data [35] (data points). Charged particles arising from the break-up of the beam and target (dotted line) and charged particles that result from the outgoing jets initial and final-state radiation (dotted dashed line) are shown separately.
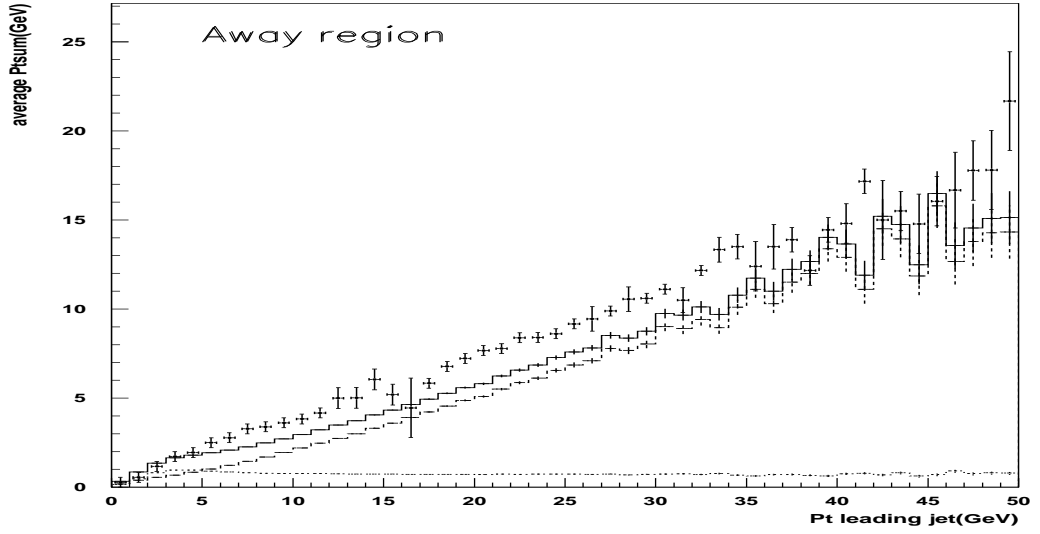
Figure 4.10: The average P_t sum of charged particles as a function of P_t (leading charged jet) in the away region. HERWIG + Underlying Event model solid line simulated data, experimental CDF data [35] (data points). Charged particles arising from the break-up of the beam and target (dotted line) and charged particles that result from the outgoing jets initial and final-state radiation (dotted dashed line) are shown separately.
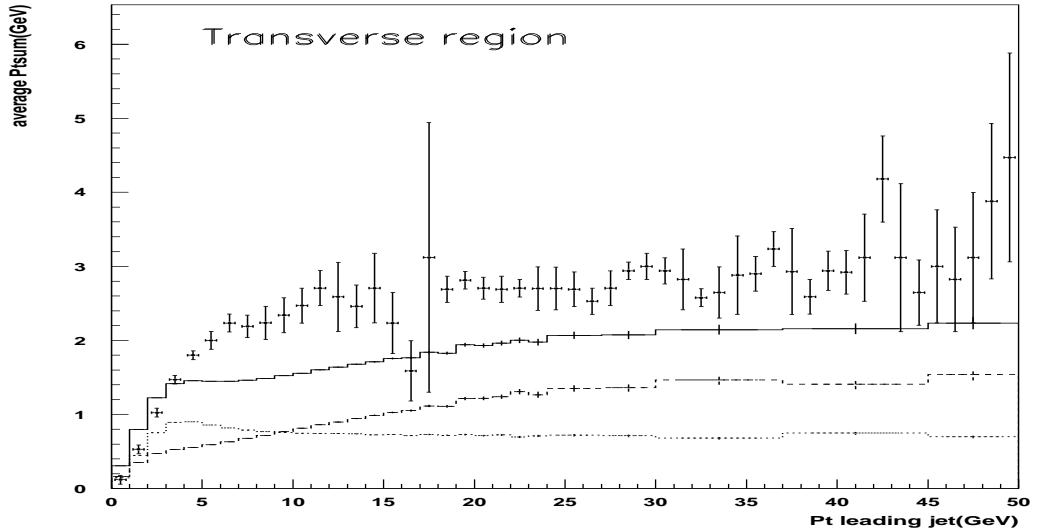
Figure 4.11: The average P_t sum of charged particles as a function of P_t (leading charged jet) in the transverse region. HERWIG + Underlying Event model (solid line) simulated data, experimental CDF data [35] (data points). Charged particles arising from the break-up of the beam and target (dotted line) and charged particles that result from the outgoing jets intial and final state radiation (dotted dashed line).
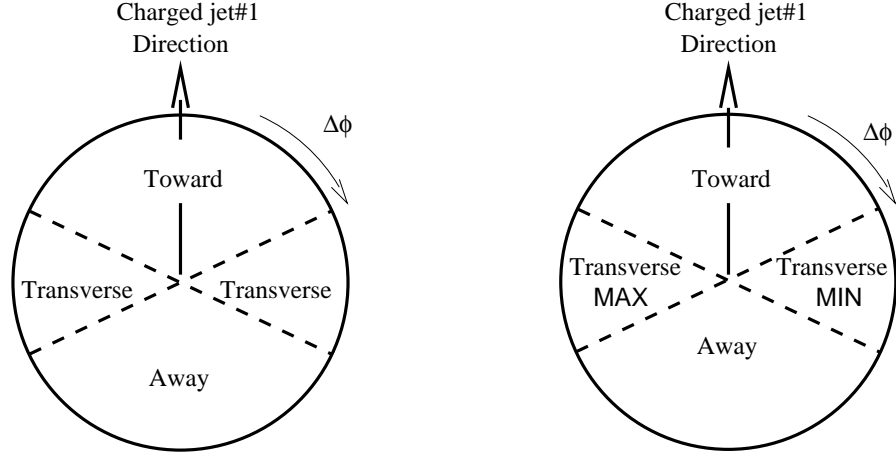
Figure 4.12: The transverse region (left) split in two, the transverse maximum (Max) and minimum (Min) parts (right).

underlying event [39]. Furthermore it is expected that the underlying event component should almost cancel in the difference between the two parts, leaving only the hard component (plus initial and final state radiation).

As shown in figs.4.13 - 4.16 the transverse Max region is more sensitive to the hard scattering component of the underlying event and the Min cone is more sensitive to the remnant-remnant component as expected in [39]. However fig.4.17 shows that the difference between the Max and Min region does not completely remove the beam-beam component although it does reduce it by about a factor of two.

4.4.4   Transverse Cone analysis

In this section we present the complement to the underlying event simulation study in the transverse region by looking at the underlying event activity in transverse cones [35, 40, 41] instead of transverse regions. The transverse cones as shown in fig.4.18 are defined as regions in $\eta - \phi$ space of radius $R = 0.7$ located at the same pseudo-rapidity as the leading jet but with azimuthal angle $\Delta\phi$ at $+\pi/2$ and $-\pi/2$ from the leading jet. In the experiment the leading jet is built using the standard CDF cone algorithm which looks at charged and neutral particles at the calorimeter level. The leading jet

Figure 4.13: The average scalar p_t sum of the trans-Max and trans-Min charged particles as a function of P_t (leading charged jet) in the transverse region. Solid (Max) and hollow (Min) circles are the experimental CDF data [35], the solid line the corrected theoretical data from HERWIG + Underlying Event model.
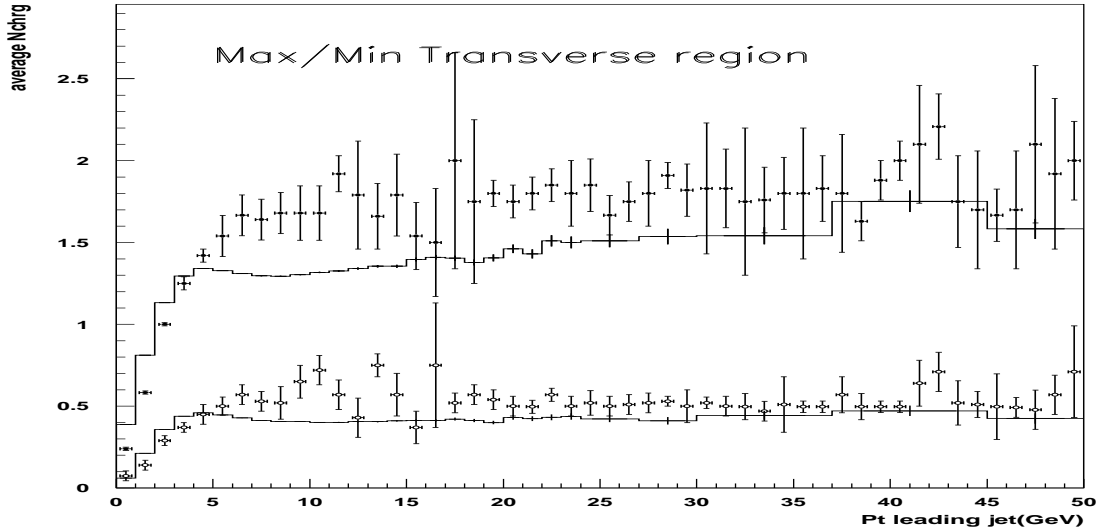
Figure 4.14: The average number of trans-Max and trans-Min charged particles as a function of P_t (leading charged jet) in the transverse region. Solid (Max) and hollow (Min) circles are the experimental CDF data [35], the solid line the corrected theoretical data from HERWIG + Underlying Event model.
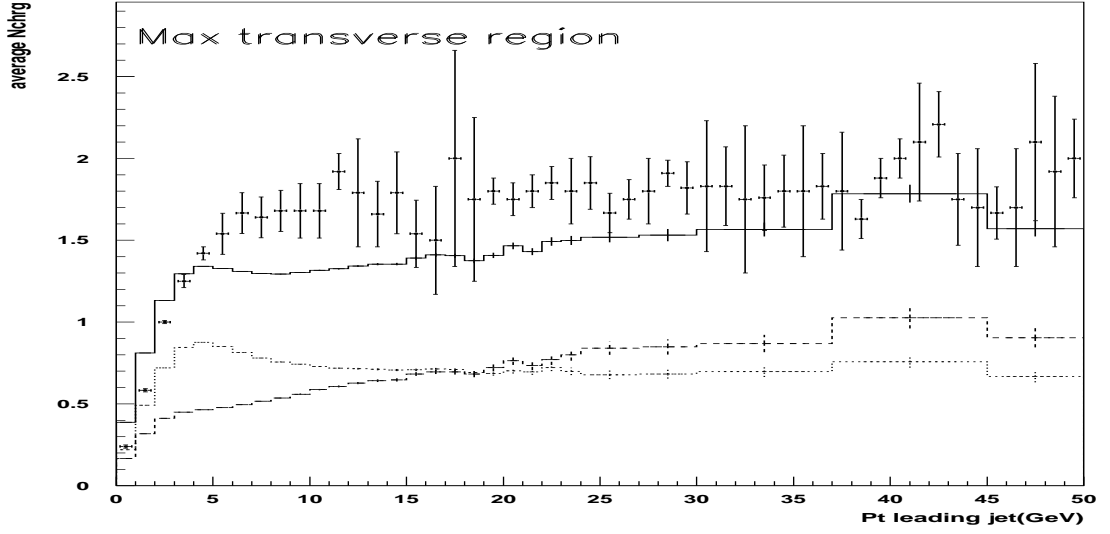
Figure 4.15: The average number of trans-Max particles as a function of P_t (leading charged jet) in the transverse region. Solid points are the experimental CDF data [35] and the solid line the simulated data from HERWIG + Underlying Event model. Charged particles arising from the break-up of the beam and target (dotted line) and charged particles that result from the outgoing jets initial and final-state radiation (dotted dashed line) are shown separatly.
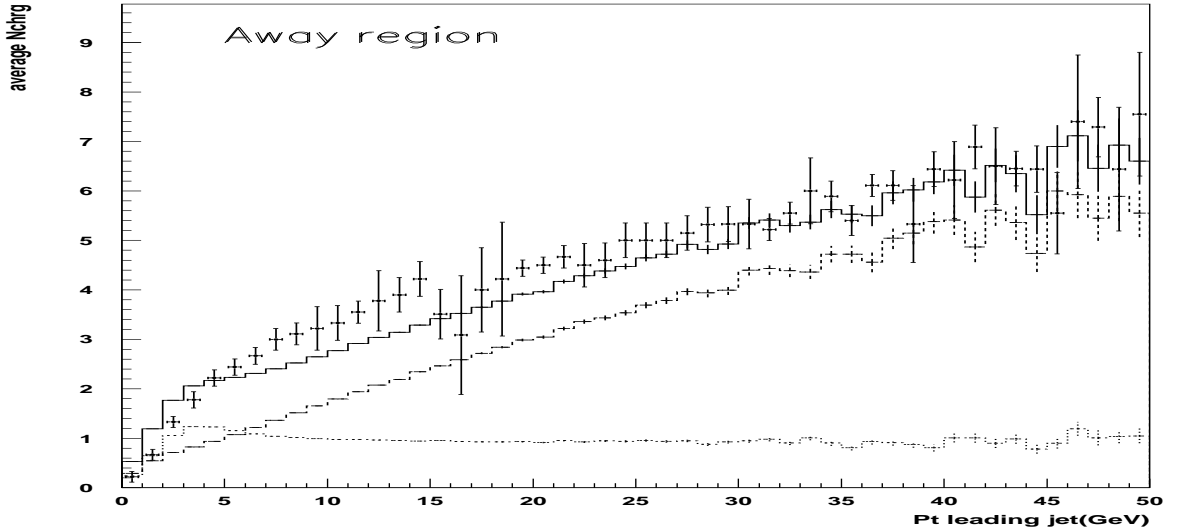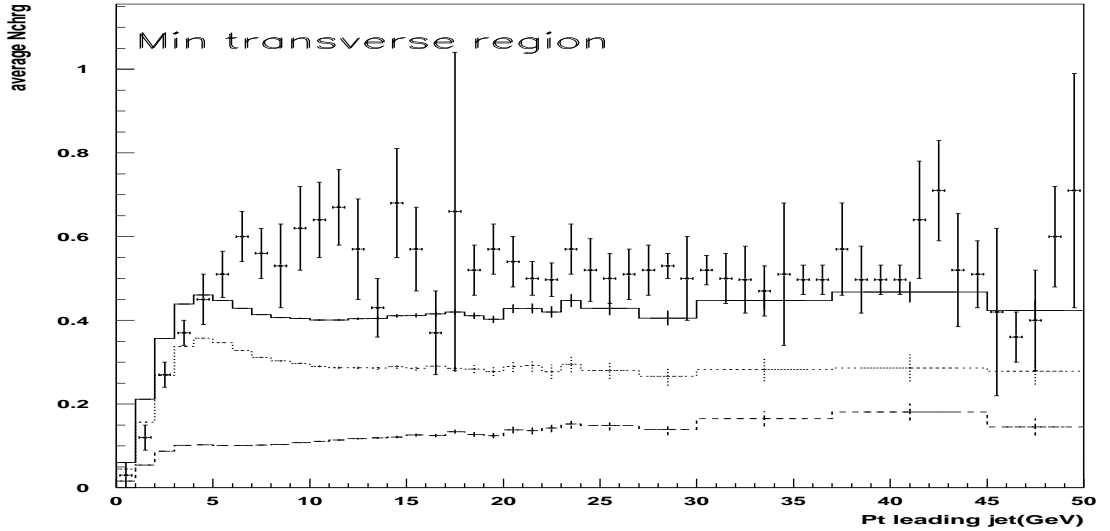

Figure 4.16: The average number of trans-Min particles as a function of P_t (leading charged jet) in the transverse region. Solid points are the experimental CDF data [35] and the solid line the simulated data from HERWIG + Underlying Event model. Charged particles arising from the break-up of the beam and target (dotted line) and charged particles that result from the outgoing jets initial and final-state radiation (dotted dashed line) are shown separatly.
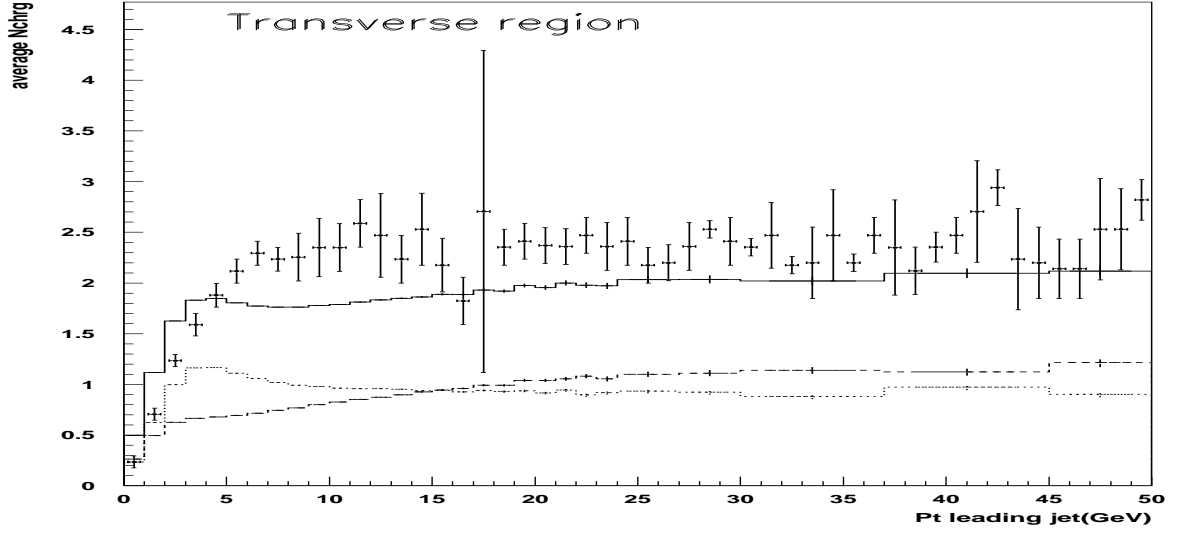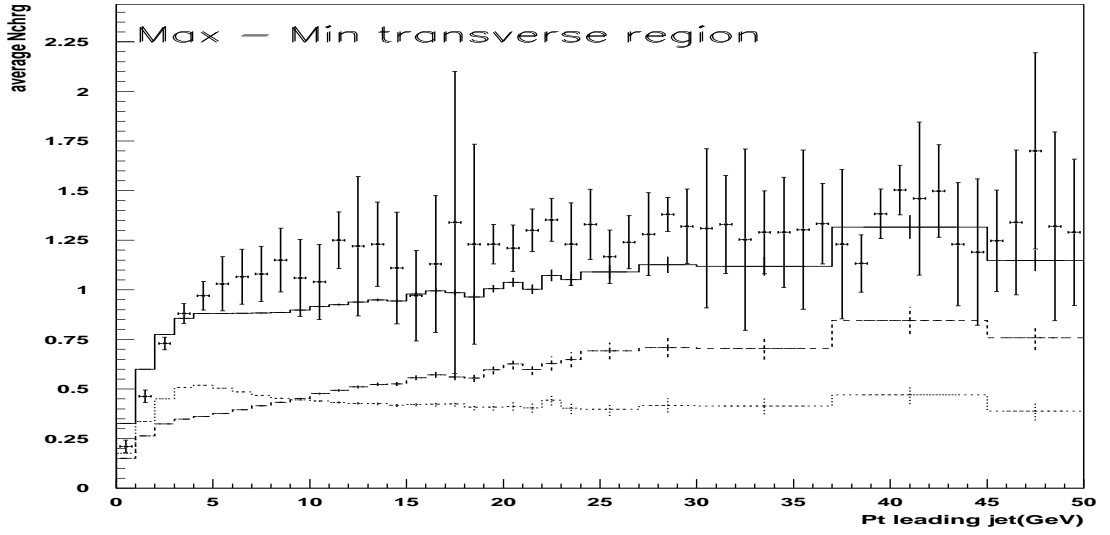
Figure 4.17: The average difference, trans-Max minus trans-Min, for the number of charged particles as a function of P_t (leading charged jet) in the transverse region. Solid points are the experimental CDF data [35] and the solid line the simulated data from HERWIG + Underlying Event model. Charged particles arising from the break-up of the beam and target (dotted line), and charged particles that result from the outgoing jets initial and final-state radiation (dotted dashed line) are shown separately.
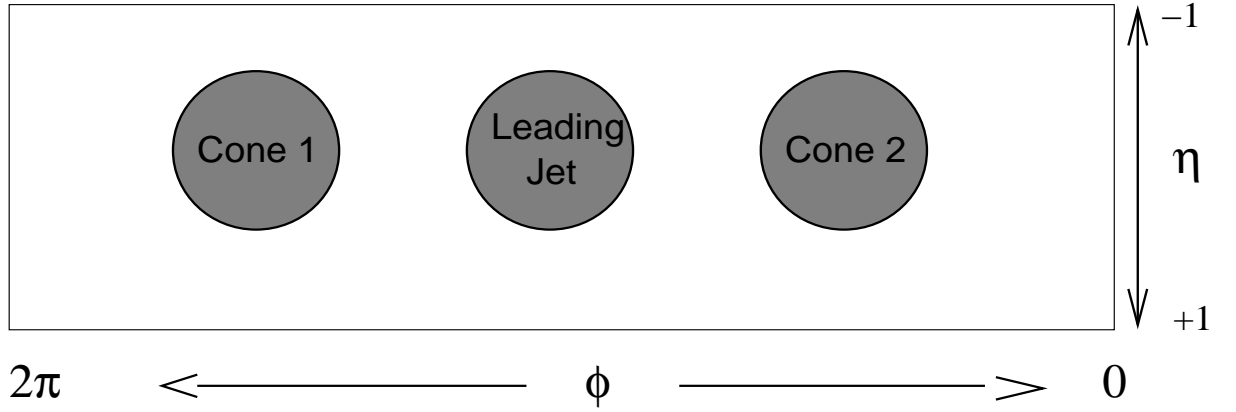
Figure 4.18: Illustration of transverse cones in the η - ϕ space with $|\eta|<1$ located at the same pseudorapidity as the leading jet but with azimuthal angle $\Delta\phi = +90°$ and $\Delta\phi = -90°$ relative to the leading jet. Each transverse cone has an area in η - ϕ space of $\pi R^2 = 0.49\pi$.

transverse energy covers the range between 50 and 300 GeV, $50 < E_T < 300$ GeV and can be seen as complementary to the low p_t jet study of transverse regions. The maximum and minimum activity in the two transverse cone regions is determined on an event by event basis, in the same way as in the transverse region analysis. Each of the cones has an area in $\eta - \phi$ space of $\pi R^2 = 0.49\pi$. The two cones in fig.4.18 are located in the region far away from the leading jet and should be particularly sensitive to the underlying event activity. Our simulated data were not corrected for the calorimeter effect which we consider as small (of the order of 5%). From fig.4.19 we see that the Monte Carlo prediction and the experimental data have a similar behaviour for both the max and min cone. We notice from fig.4.19 that the average p_t in the maximum cone increases with the jet energy while in the minimum cone the average p_t has a flat dependence indicating that it is dominated by contributions from the underlying event.
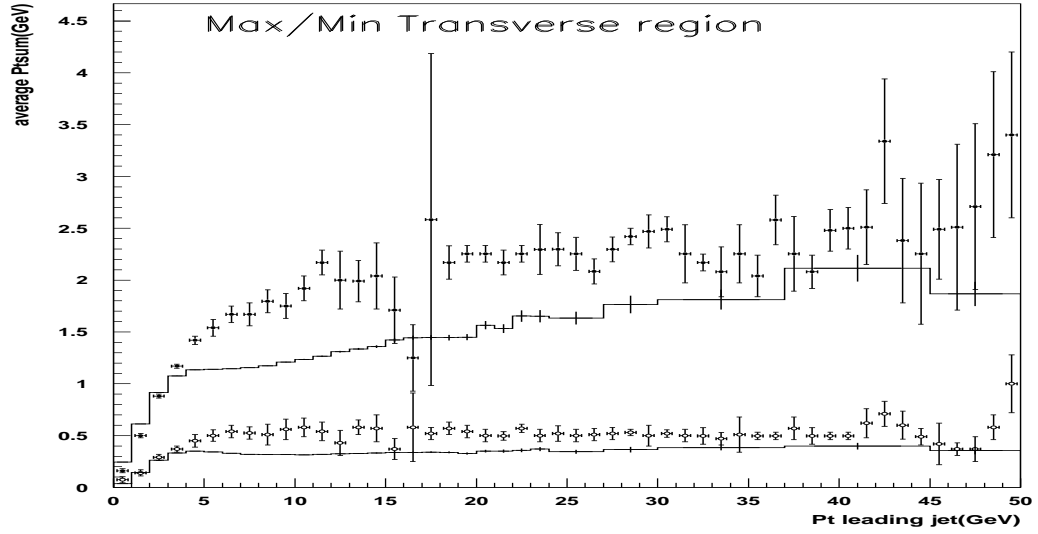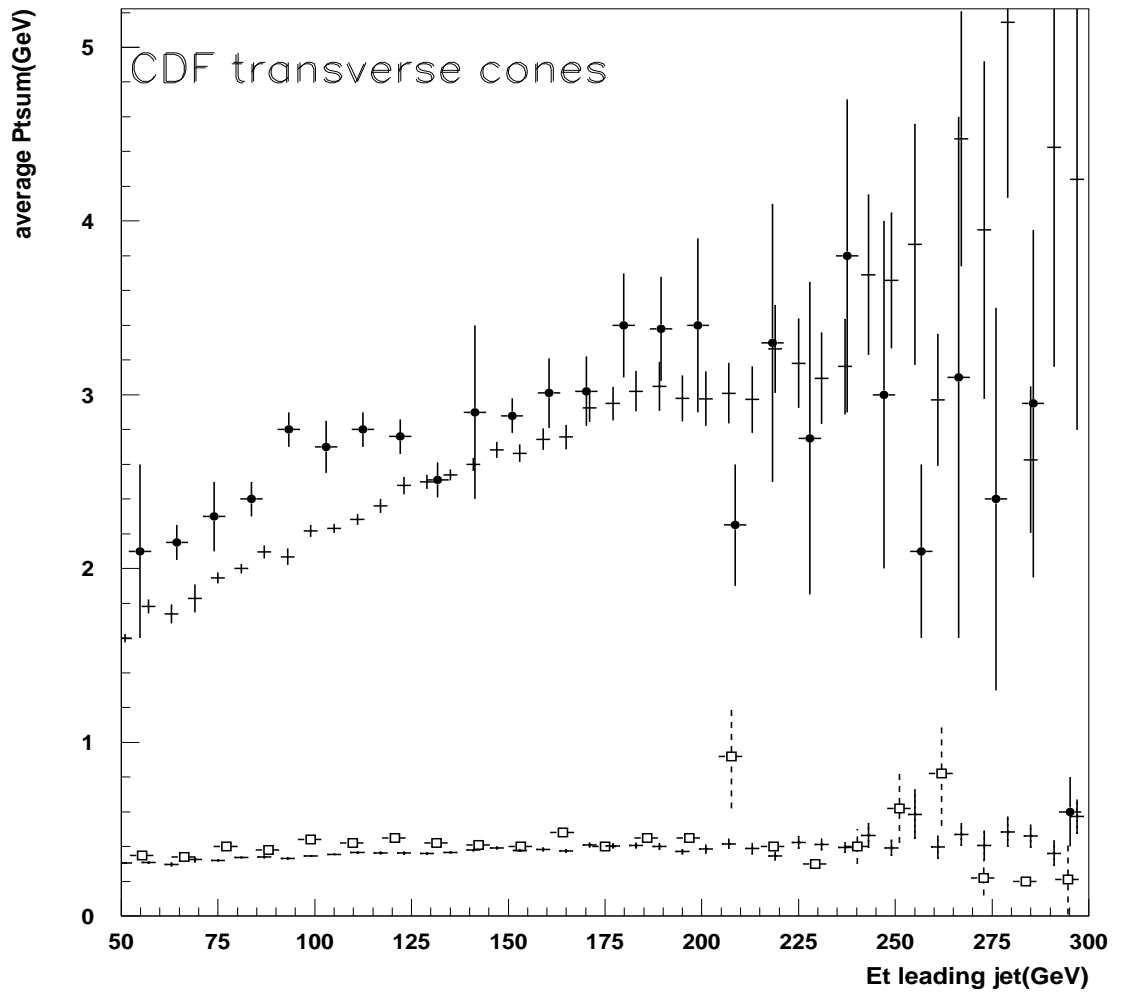
Figure 4.19: The average scalar p_t sum of the trans-Max and trans-Min charged particles as a function of E_t (leading charged jet) in transverse cones. Solid and hollow circles experimental CDF data [35], HERWIG + Underlying Event model (crosses) simulated data.

4.5   Summary

In this chapter we have shown our agreement with the results from [35] on the transverse region analysis. We have shown that HERWIG describes charged particle distributions rather well in all regions except in the transverse i.e. the most sensitive to the underlying event. HERWIG has a too steep p_t dependence and not enough charged particle activity in the transverse region. Separating the transverse region into two parts, Max and Min, provided additional information. The transverse Max part appears to be more sensitive to the hard component of the underlying event while the transverse Min part appears to be more sensitive to the remnant-remnant component part. Still the difference between the two parts do not entirely cancel the remnant-remnant part making the possibility to clearly separate the two components difficult. In the transverse cone analysis there is a fair agreement between HERWIG and the experimental data. In the next chapter we will present the multiparton interaction model as a substitute for HERWIG's Underlying Event model and discuss the results obtained.

Chapter 5

Hard Multiparticle Interaction Model

5.1   Introduction

In this chapter we present a simulation of proton-antiproton collisions at $\sqrt{s}$ =1.8 TeV in which the HERWIG Soft Underlying Event model is substituted by the Hard Multiparton Interaction model. We begin this chapter by presenting a brief overview of the Hard Multiparton Interaction model [42] with some references to a similar model used in the PYTHIA event generator [43]. In Section 5.2.2 we examine whether the addition of secondary hard scatters to the main hard interaction improves the simulated data on the underlying event presented in Chapter 4. Finally in Section 5.2.4 we propose to tune the mass (i.e. the radius of the proton) in the Hard Multiparton model in order to obtain a better fit to the experimental data.

5.1.1   Multiparton Interactions

Since hadrons are considered as composite particles it is reasonable to assume that in high energy collisions (i.e. hadron-hadron and lepton-hadron) interesting phenomena such as multiparton hard interactions might occur. These semi-hard interactions would arise from the hard scattering of partons carrying a small fraction of momenta of their parent hadrons. Such semi-hard interactions would lead to the appearance of jets with transverse energy much smaller than that of the total energy available in the hadronic collisions. The experimental evidence for multi-parton scattering in hadron-hadron collisions has been found in measurements carried out by CDF [44, 45], AFS [46], UA2 [47] and UA1 [48] collaborations.

The first hard multiparton formalism was implemented within PYTHIA Monte Carlo event generator. PYTHIA is a complete Monte Carlo event generator and, like HERWIG, includes all the necessary formalism (i.e. hard-scattering matrix elements, structure functions, initial and final state radiation and a hadronisation model) for simulating a hard interaction between two hadrons. In PYTHIA the formalism based on perturbative QCD for large p_t interactions, which determines the rate of parton-parton interactions as a function of the transverse momentum scale p_t, is extended

into the low-p_t region where a regularization of the divergence in the cross section for $p_t \to 0$ is introduced providing the main free parameter of the model. The secondary hard scatters in PYTHIA are assumed to happen independently of each other so that the number of secondary interactions in a hadron-hadron collision is given by a Poissonian distribution. However secondary scatters cannot be considered as really independent since some correlation between them must exist, most simply if we are to conserve momentum and flavour for each interacting parton, and less naively if we are to consider various quantum mechanical effects. Correlations between the secondary scatters are introduced in PYTHIA by the ordering of scatterings in the falling sequence of $x_t = 2p_t/E_{CM}$. Furthermore since the PYTHIA multiparton model assumes hadrons to be extended objects the average number of secondary scatters depends on the collision impact parameter (larger for central collisions and smaller for peripheral ones) and the assumed matter distribution of the two colliding hadrons. Data simulated with PYTHIA and the multiparton formalism with a double Gaussian matter distribution proved to be in rather good agreement with the UA1 [48] experimental data for various jet observables such as event rates for multiple minijet production, the variation of pedestal level with jet energy and the average transverse energy produced away from jet axes.

In the following section we present a Hard Multipartion Interaction Model which assumes (similar to PYTHIA) that at high centre of mass energy ($\sqrt{s} > 100$ GeV), the main hard scattering is accompanied by semihard interactions. Multiparton interactions will then drive the rise of the inclusive jet cross section at high energies through the small-x behaviour of the parton distribution or, to a good approximation, that of the dominant gluon distribution. The calculated semihard cross section is then expected to give an increasingly important part of the total hadron-hadron cross section at higher energies.

The inclusive jet cross section calculated at lowest order QCD (see eq.3.16), will eventually exceed the Froissart bound (see Chapter 1) and the total hadron-hadron cross section at very high energies. Thus multiparton interactions can be seen as a

unitarity correction to the total inclusive jet cross section at higher energies if we consider that the inclusive jet cross section exceeds the total hadron-hadron cross section by the mean multiplicity of multiple interactions.

5.2 Multiparton Interactions in the $p\overline{p}$ environment
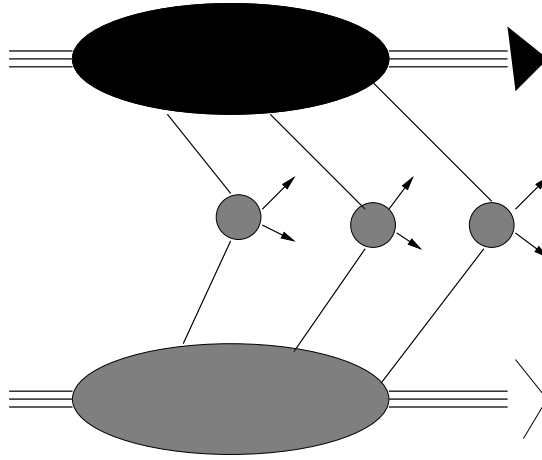
Figure 5.1: Example of a multiparton scattering in $p\overline{p}$ collision

In this section we summarize a multiparton-interaction model proposed in [42] which we use as the hard multiple-interaction part of our eikonal model to be introduced in Chapter 6.

In [49, 50, 51, 52, 42] it was shown that the average number of secondary hard scatters in an event can be deduced from the QCD improved parton model.

As mentioned in the introduction, multiparton interactions are seen as additional two to two parton-parton hard scatterings (the main one being the one involving the largest transverse momentum exchange Q) between partons contained in the two proton-antiproton remnants. In the centre-of-mass frame the two incoming hadrons can be pictured as Lorentz contracted 'parton pancakes' colliding at some impact

parameter, b. The average number of secondary scatters can be written as

$$
\begin{aligned}
\langle n(b, s_{p\overline{p}}) \rangle &= \int \pi db'^2 \int_{p_t^{min\,2}}^{s_{p\overline{p}}/4} dp_t^2 \int_{4p_t^2/s_{p\overline{p}}}^1 dx_p \int_{4p_t^2/x_p s_{p\overline{p}}}^1 \\
&\quad dx_{\overline{p}} \sum_{i,j} f_i(x_p,\ p_t^2, |\mathbf{b}' - \mathbf{b}|) f_j(x_{\overline{p}},\ p_t^2, \mathbf{b}') \\
&\quad \times \frac{d\hat{\sigma}_{ij}(x_p x_{\overline{p}} s_{p\overline{p}}, p_t)}{dp_t^2},
\end{aligned}
\tag{5.1}
$$

where x_p and $x_{\overline{p}}$ are the longitudinal fractional momentums carried by partons of the two incoming hadrons, $\frac{d\hat{\sigma}_{ij}(x_p x_{\overline{p}} s_{p\overline{p}}, p_t)}{dp_t^2}$ is the full differential cross section for parton-parton scattering, and $f_j(x_{\overline{p}},\ p_t^2, \mathbf{b}) dx db^2$ is equal to the number of partons in the interval dx and the transverse area element db^2 a distance b from the centre of the hadron. It is also assumed that $f_j(x_{\overline{p}},\ p_t^2, \mathbf{b}) dx db^2$ can be factorised in two parts; the $f_j(x_{\overline{p}},\ p_t^2)$ and $\rho(\mathbf{b})$ part. $f_j(x_{\overline{p}},\ p_t^2)$ is now the usual parton distribution function of parton-j in hadron-$\overline{p}$ and $\rho(\mathbf{b})$ is the probability density for finding a parton in the area db^2 at impact parameter b. Factorizing the b dependence like this is an assumption. In particular QCD effects which would spoil this, e.g. perhaps leading to 'hot spots' of partons are not considered.

The model assumes that the parton distribution inside the two hadrons is given by the electric form factor distribution of the two hadrons

$$
G_p(\mathbf{b}) = G_{\overline{p}}(\mathbf{b}) = \int \frac{d^2\mathbf{k}}{(2\pi)} \frac{exp(\mathbf{k} \cdot \mathbf{b})}{(1 + \mathbf{k}^2/\mu^2)^2},
\tag{5.2}
$$

with $\mu^2 = 0.71$ GeV^2. The significance of this assumption is that the dominant gluon distribution (at low x) in multiparton processes is tightly coupled to that of the spatial distribution of the constituent (or valence) quarks. The average number of scatters from eq.5.1 can now be rewritten as

$$
\langle n(b, s_{p\overline{p}}) \rangle = A(b) \sigma_H^{inc}(s_{p\overline{p}}),
\tag{5.3}
$$

where $\sigma_H^{inc}(s_{p\overline{p}})$ is the inclusive cross section for $p\overline{p} \rightarrow jets$,

$$
\begin{aligned}
\sigma_H^{inc}(s_{p\overline{p}}) &= \int_{p_{tmin}^2}^{s_{p\overline{p}}/4} dp_t^2 \int_{4p_t^2/s_{p\overline{p}}}^1 dx_p \int_{4p_t^2/x_p s_{p\overline{p}}}^1 dx_{\overline{p}} \sum_{i,j} f_i(x_p,\ p_t^2) f_j(x_{\overline{p}},\ p_t^2) \\
&\quad \times \frac{d\hat{\sigma}_{ij}(x_p x_{\overline{p}} s_{p\overline{p}}, p_t)}{dp_t^2},
\end{aligned}
\tag{5.4}
$$

and where the profile function $A(b)$ in eq.5.3 specifies the overlap of partons of the two colliding hadrons in impact parameter b. $A(b)$ can be written as a convolution of form factors distributions (in the first approximation where pQCD effects are ignored) of the two incoming hadrons as

$$A(b) = \int d^2\mathbf{b'} G_p(\mathbf{b'}) G_{\overline{p}}(\mathbf{b} - \mathbf{b'}), \qquad (5.5)$$

the integral in eq.5.5 then yields [51],

$$A(b) = \frac{\mu^2}{96\pi}(\mu b)^3 K_3(\mu b), \qquad (5.6)$$

where $K_i(x)$ is the modified Bessel function.

The overlap function $A(b)$ satisfies the normalization condition

$$\int \pi db^2 A(b) = 1. \qquad (5.7)$$

In addition to the assumption for the form of the parton distribution, the model assumes (as in [43, 42]) that secondary hard scatters are independent of each other so that the probability for the number of hard scatters h, in a $p\overline{p}$ collision at a given value of impact parameter, is given by the Poissonian probability distribution

$$P_h = \frac{(\langle n(b, s_{p\overline{p}}) \rangle)^h}{h!} \exp\left(-\langle n(b, s_{p\overline{p}}) \rangle\right). \qquad (5.8)$$

The inelastic hard cross section for $p\overline{p} \to$ partons with $p_t > p_{tmin}$ can now be written as

$$
\begin{aligned}
\sigma_H(s_{p\overline{p}}) &= \pi \int db^2 \sum_{h=1}^{\infty} P_h \\
&= \pi \int db^2 [1 - \exp(-\langle n(b, s_{p\overline{p}}) \rangle)]. \qquad (5.9)
\end{aligned}
$$

Since the inclusive jet cross section in eq.5.4 counts all jet pairs (even ones which occur in the same event) we expect $\sigma_H^{inc}(s_{p\overline{p}})$ to be greater than $\sigma_H(s_{p\overline{p}})$ by a factor equal to the average number of secondary scatters in an event (averaged over impact parameter) containing at least one hard scattering. This can be expressed as

$$
\begin{aligned}
\langle n(s_{p\overline{p}}) \rangle &= \frac{\int db^2 \sum_{m=1}^{\infty} m P_m}{\int db^2 \sum_{m=1}^{\infty} P_m} \\
&= \frac{\int db^2 \langle n(b, s_{p\overline{p}}) \rangle}{\int db^2 [1 - exp(-\langle n(b, sp\overline{p}) \rangle)]} \\
&= \frac{\sigma_H^{inc}(s_{p\overline{p}})}{\sigma_H(s_{p\overline{p}})}. \qquad (5.10)
\end{aligned}
$$

Note that $\sigma_H(s_{p\overline{p}})$ must always be less than the total $p\overline{p}$ cross section, whereas $\sigma_H^{inc}(s_{p\overline{p}})$ need not be.

The Hard Multiparton model is implemented as part of the HERWIG Monte Carlo program. Running the Hard Multiparton model in conjunction with HERWIG comes from the necessity to confront the simulated data with real final states data from experimental measurements. This can be achieved only by using realistic hadronisation and parton showering models already implemented within the HERWIG program. Here we give a brief summary of the Hard Multiparton implementation within HERWIG.

5.2.1   Multiparton Interaction Implementation

Event simulation starts with HERWIG generating a hard subprocess according to the leading order cross section using the parton distribution set selected by the user. Both incoming and outgoing partons involved in the hard subprocess (at some hard scale Q) are evolved (backward for the incoming parton) through a coherent parton shower algorithm until they reach a typical hadronic scale, $Q_h \approx 1\text{GeV}$. The coherent parton shower algorithm [25] resums to all orders both single logarithmic terms associated with the collinear emission (through implementation of the DGLAP splitting function) and single and double logarithmic terms associated with soft emissions (see Chapter 3). All the successive partons emitted in the parton shower are colour connected in such a way that partons carrying colour(anticolour) tend to end up close in momentum and real-space to their anticolour(colour) partners. Once the evolved partons have reached a hadronisation scale Q_h, clusters of partons are formed where each colour connected pair of partons forms a single colourless cluster. Each cluster is then decayed into hadrons according to phase space arguments [24]. The backward evolution in HERWIG is required to end up with the valence parton. Once the 4-momentum of the valence parton is known energy-momentum conservation is used to calculate the momentum of the remaining hadron remnant. In the case of the proton(antiproton) the remaining diquark(antidiquark) is taken to be a single anticolour(colour) parton.

In implementing multiple interactions into the Monte Carlo event generator the assumption that different scatters are uncorrelated does not hold any more. This is because the global energy-momentum conservation is imposed by adding the simplest possible correlation, a Θ function in the cross section to produce h and only h scatters requiring their total energy to be less than the available energy. Multiparton events are generated according to probabilities for exactly h scatters calculated using the analytical model with the total cross section calculated according to eq.5.9. Scatters in which energy-momentum cannot be conserved are vetoed. Once the main hard subprocess has been simulated, energy-momentum conservation is used to calculate the momentum of the remaining diquark(antidiquark) or proton(antiproton) remnant. Each diquark carries opposite colour to that of the parton involved in the hard subrocess. After the first hard scattering has been completed a number of secondary hard subprocess are simulated where each coloured remnant from the previous interaction is labeled as the new incoming hadron with identical properties to the original hadron but with gluons labeled as its valence partons.

We have mentioned the multiparton formalism implemented within PYTHIA in Section 5.1.1 and we would now like to underline differences and similarities between the two models. The main similarity is that both models assume that multiple interactions are independent of each other i.e. that the probability for the number of hard scatters is given by the Poissonian probability distribution. The main difference between the two models is that in PYTHIA multiparton model, successive hard scatterings are arranged in falling sequence of $x_t = 2p_t/E_{cm}$, with the first scattering being the hardest followed by subsequent softer ones. In the Hard Multiparton model such ordering in p_t of successive scatters is not imposed so that all scatters are treated equally. While the Hard Multiparton model is implemented with an abrupt p_t cutoff the PYTHIA model allows a possibility for a smooth turn-off at p_{t0} of the hard scale. This smooth turn-off of the hard scale can be motivated by the decrease of the effective strong coupling at low p_t, since the exchanged gluons with large transverse wavelength fail to resolve the individual colour charges. Finally the matter distribution describing

the parton distributions within the two hadrons are different in the two models, double gaussian in the case of PYTHIA and electric form factors in the multiparton hard model (we recall that the electric form factor distribution in eq.5.2 corresponds to the hadron's charge distribution in the Breit frame). Finally we mention a difference of implementation of multiparton interactions between the two models, while in the PYTHIA multiparton model each hard scattering happens at a certain value of the impact parameter b (selected from a given overlap distribution function), in the hard multi-parton model the probability for having h hard secondary scatters is integrated over the impact parameter b.

5.2.2   Study of particle correlations in azimuthal angle.

In this section we repeat essentially the same analysis as was done in Chapter 4, although we substitute HERWIG Soft Underlying Event model by the Hard Multiparton Interaction model. We use two values of p_{tmin} (3 GeV and 2 GeV) to test the agreement between the simulated and experimental data.

Average number of charged particles vs p_t (charged jet) in the toward and away regions

In fig.5.2 we show the total average number of charged particles in the event as a function of the p_t of the leading charged jet for two values of $p_{tmin} = 3$ GeV and 2 GeV. For $p_{tmin} = 2$ GeV the Hard Multiparton model has a wrong p_t dependence of the total average number of charged particles which for higher p_t values of the leading jet becomes too flat and thus fails to produce the right amount of charged particles observed in the experiment. For $p_{tmin} = 3$ GeV the model produces the right shape for the charged particles distribution but with a wrong normalization. The plots of the average number of charged particles in the toward and the away region confirm the same data pattern as observed for the total average number of charged particles (as shown in fig.5.3 and fig.5.4).

Average scalar p_t sum of charged particles vs p_t (charged jet) in the toward and away regions

In fig.5.6 we show the plot of the average scalar p_t sum of charged particles as function of the p_t of the leading jet in the toward region which is well described by the model for both values of p_{tmin}. In the away region however the model gives a wrong p_t distribution for $p_{tmin} = 2$ GeV (too low for jets > 15 GeV as shown in fig.5.7).

The transverse region

The transverse region is described (overall) better than by the HERWIG Soft Underlying Event model (see Chapter 4) for $p_{tmin} = 2$ GeV as shown in fig.5.5 and fig.5.8. The slope of the simulated distributions seems to have the right (flat) distribution although the data for both the average number of charged particles and the average scalar p_t is still below the experimental one. For the value of $p_{tmin} = 3$ GeV the simulated distributions are too low compared to the experimental data as shown in fig.5.5 and fig.5.8.

In fig.5.11 we show the multiparton contribution to the transverse momentum sum in the transverse region for two values of p_{tmin}, 2 GeV and 3 GeV which we compare to the HERWIG hard subprocess (including initial and final state radiation). For p_{tmin} = 2 GeV we notice that the contribution due to multiple scattering first increases rapidly for low p_t jets ($p_t < 5$ GeV with $p_{tmin} = 2$ GeV) to then form a plateau region for jets with $p_t > 10$ GeV. We thus conclude that multiple scatters contribute little to jet events with leading jet energies (p_t) greater than 30 GeV. Finally we point out that a better agreement with experimental data is obtained when the multiparton interaction rate is increased (i.e. from $\langle n_{hard} \rangle = 1.07$ (at $p_{tmin} = 3$ GeV) to $\langle n_{hard} \rangle = 1.3$ (at $p_{tmin} = 2$ GeV)).
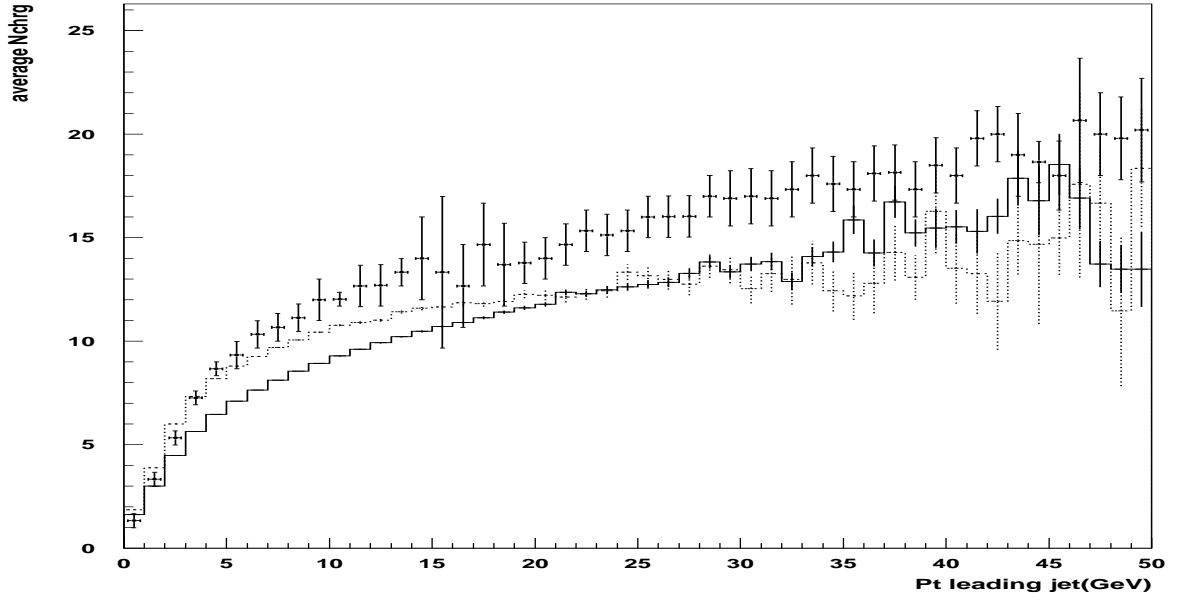
Figure 5.2: The average total number of charged particles in the event as a function of P_t (leading charged jet). HERWIG + Hard Interaction model simulated data (solid line p_{tmin} = 3.0 GeV), (dotted line p_{tmin} = 2.0 GeV), experimental CDF data [35] (data points).

Minimum-maximum region analysis

In fig.5.9 and fig.5.10 we show the performance of the hard multiparton model in the two Max/Min regions for p_{tmin} = 2 GeV. While the Min region seems to be described correctly, the simulated Max region lacks both in average number of charged particles and average scalar p_t sum.

5.2.3   Proton radius as a parameter

In this section we show how the radius of the proton in the Hard Multiparton model can be used as a parameter in order to obtain a better overall agreement with the experimental data. A good agreement is obtained by reducing the proton radius by a factor of 1.73 (with p_{tmin} = 3 GeV) as shown in figs.5.14-5.22 (which we stress is not the result of the detailed fit). The reduction of the proton radius causes the value

Figure 5.3: The average number of charged particles as a function of P_t (leading charged jet) in the toward region. HERWIG + Hard Interaction model simulated data (solid line $p_{tmin} = 3.0$ GeV), (dotted line $p_{tmin} = 2.0$ GeV), experimental CDF data [35] (data points).

Figure 5.4: The average number of charged particles as a function of P_t (leading charged jet) in the away region. HERWIG + Hard Interaction model simulated data (solid line p_{tmin} = 3.0 GeV), (dotted line $p_{tmin} = 2.0$ GeV), experimental CDF data [35] (data points).

Figure 5.5: The average number of charged particles as a function of P_t (leading charged jet) in the transverse region. HERWIG + Hard Interaction model simulated data (solid line $p_{tmin} = 3.0$ GeV), (dotted line $p_{tmin} = 2.0$ GeV), experimental CDF data [35] (data points).

Figure 5.6: The average P_t sum of charged particles as a function of P_t (leading charged jet) in the toward region. HERWIG + Hard Interaction model simulated data (solid line $p_{tmin} = 3.0$ GeV), (dotted line $p_{tmin} = 2.0$ GeV), experimental CDF data [35] (data points).
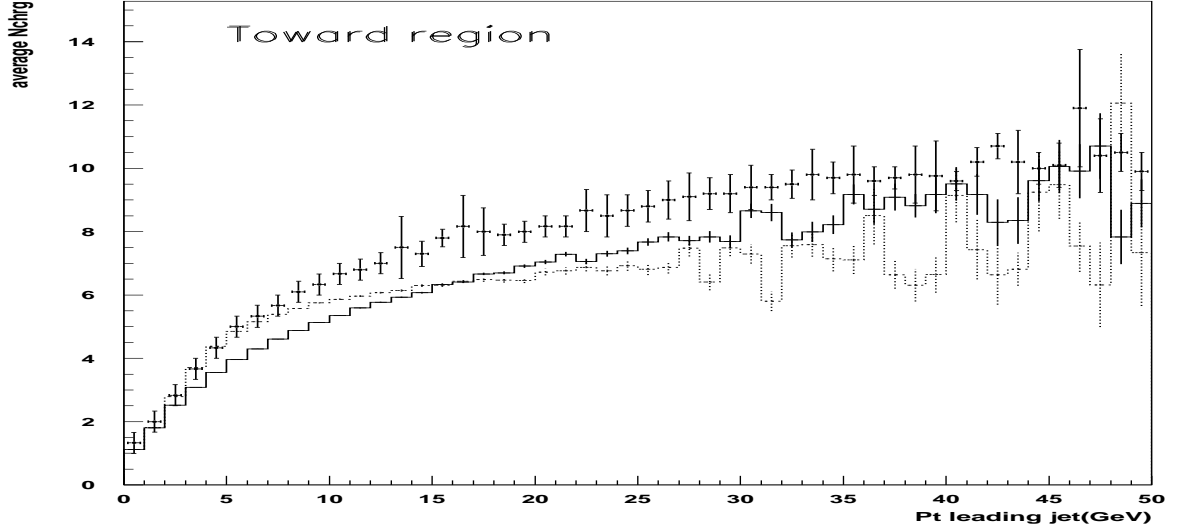
Figure 5.7: The average P_t sum of charged particles as a function of P_t (leading charged jet) in the away region. HERWIG + Hard Interaction model simulated data (solid line p_{tmin} = 3.0 GeV), (dotted line p_{tmin} = 2.0 GeV), experimental CDF data [35] (data points).

Figure 5.8: The average P_t sum of charged particles as a function of P_t (leading charged jet) in the transverse region. HERWIG + Hard Interaction model simulated data (solid line p_{tmin} = 3.0 GeV), (dotted line p_{tmin} = 2.0 GeV), experimental CDF data [35] (data points).
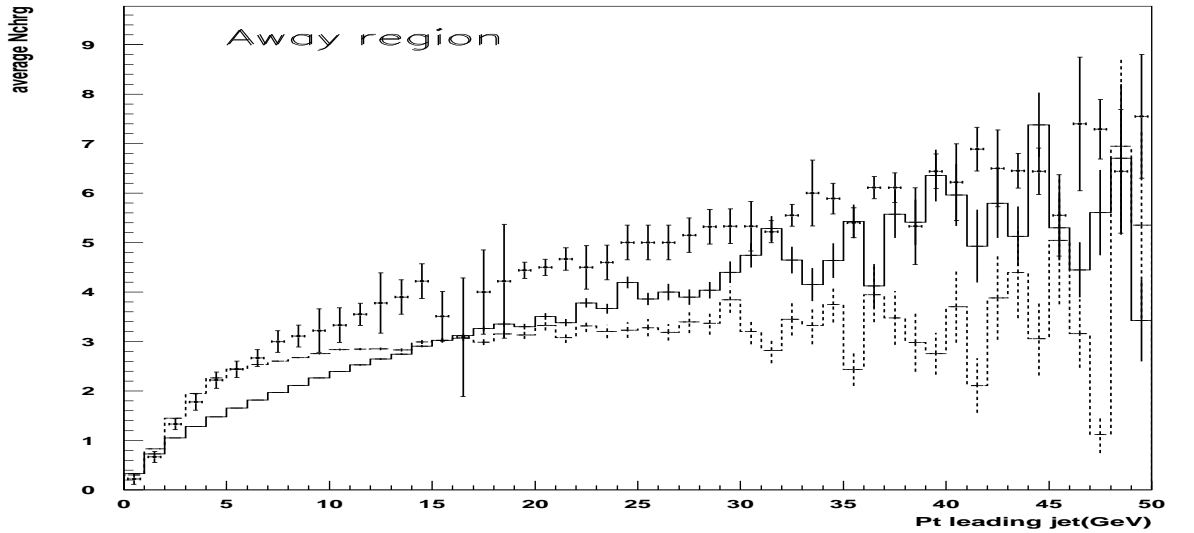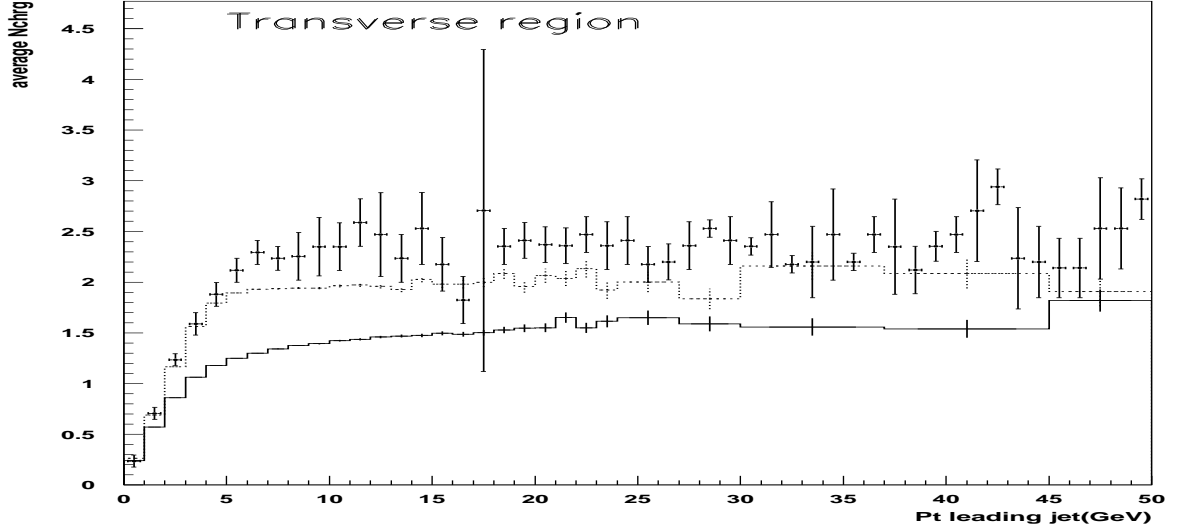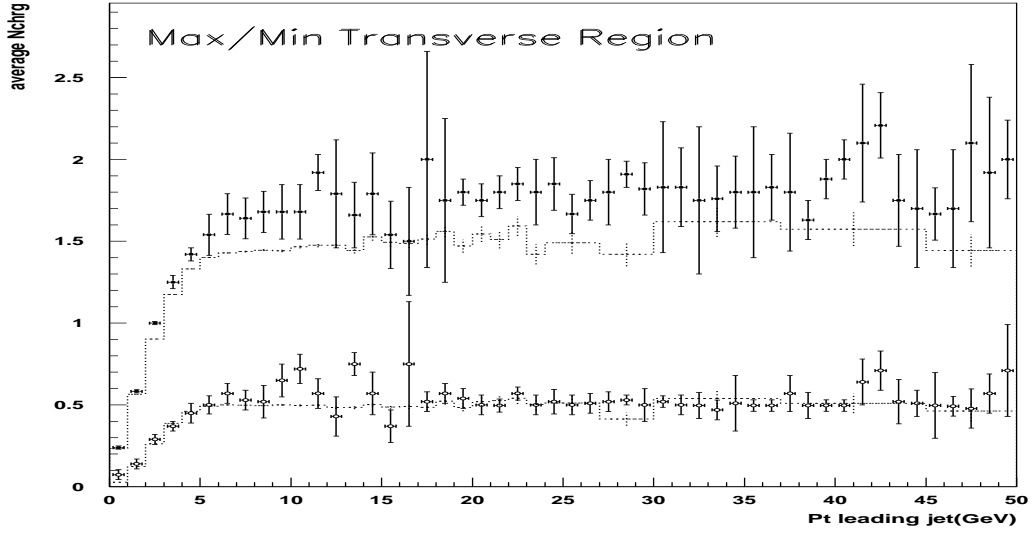
Figure 5.9: The average number of the trans-Max and trans-Min charged particles as a function of P_t (leading charged jet) in the transverse region. Solid (Max) and hollow (Min) points experimental CDF data [35]. HERWIG + Hard Interaction model simulated data (dotted line p_{tmin} = 2.0 GeV).
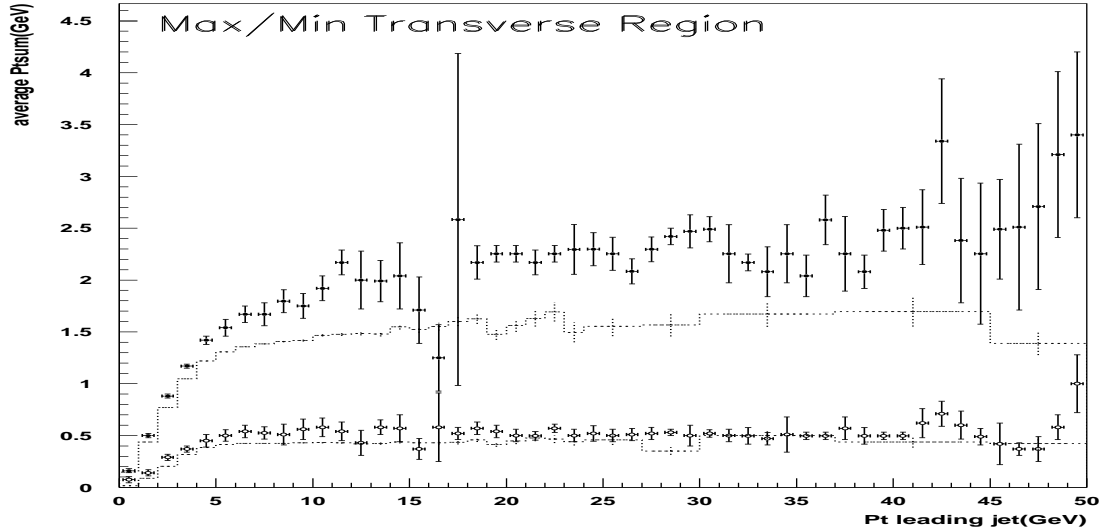
Figure 5.10: The average scalar p_t sum of the trans-Max and trans-Min charged particles as a function of P_t (leading charged jet) in the transverse region. Solid (Max) and hollow (Min) points experimental CDF data [35]. HERWIG + Hard Interaction model simulated data (dotted line p_{tmin} = 2.0 GeV).
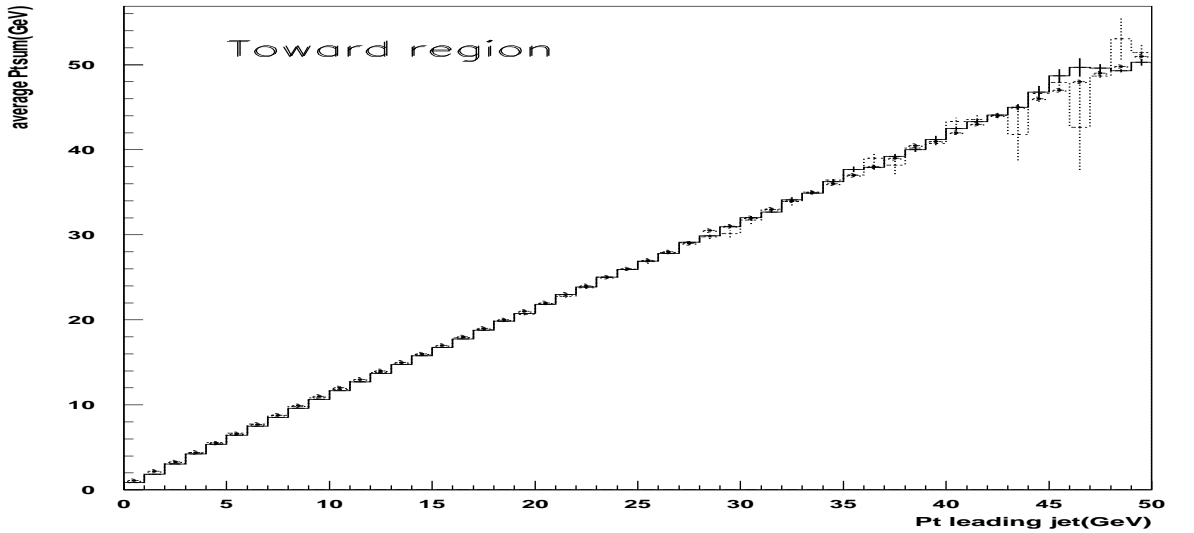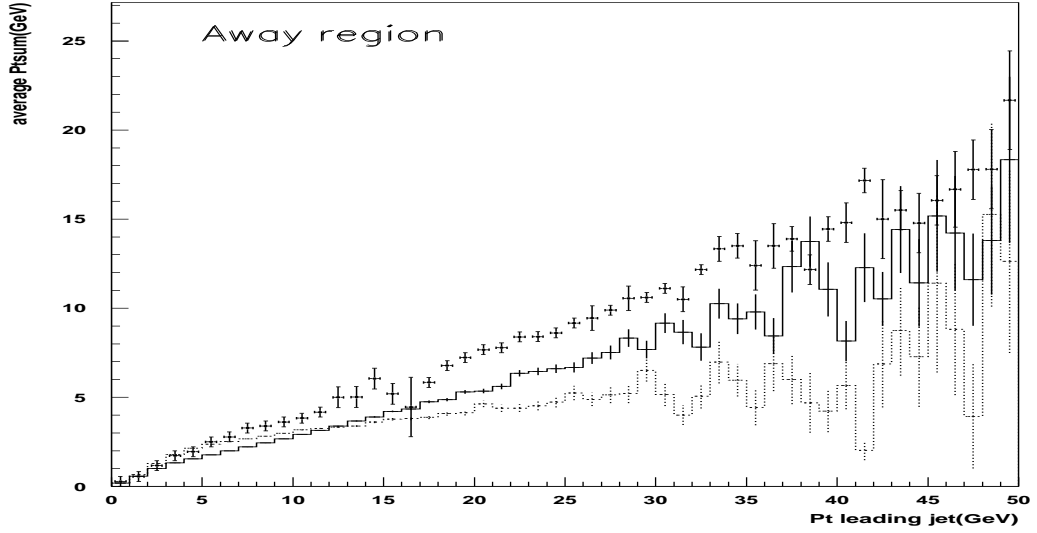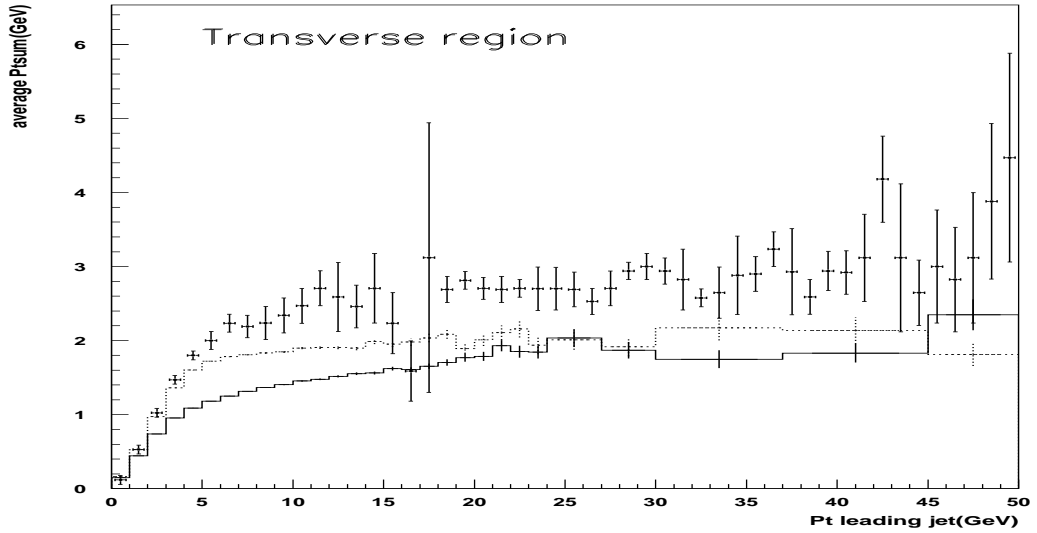
Figure 5.11: The average P_t sum of charged particles as a function of P_t (leading charged jet) in the transverse region. HERWIG + Hard Interaction model simulated data (solid line $p_{tmin} = 2.0$ GeV), (dotted line $p_{tmin} = 3.0$ GeV), HERWIG QCD hard two to two subprocess including initial and final state radiation (solid circles $p_{tmin} = 3.0$ GeV).

of the overlap function $A(b)$ to peak at a higher value for central collisions (i.e. low values of the impact parameter b) and to decrease faster for more peripheral ones as shown in fig.5.12. The result of this analysis indicates that partons can be pictured as being densely packed within small regions of the interacting hadrons as shown in fig.5.13. At this stage it is not clear what physical mechanism could explain such behaviour (although it is possible that some connection could be made with QCD hot spots ideas). We consider this result, therefore, as relevant only from a purely phenomenological point of view.

5.2.4   Conclusion

Substituting the Soft Underlying Event model by the Multiparton Hard model a clear improvement (although still not perfect) is noticed in the description of experimental data in the transverse region for the low value of $p_{tmin} = 2$ GeV. This result indicates that multiparton interactions can be considered as a step in the right direction for
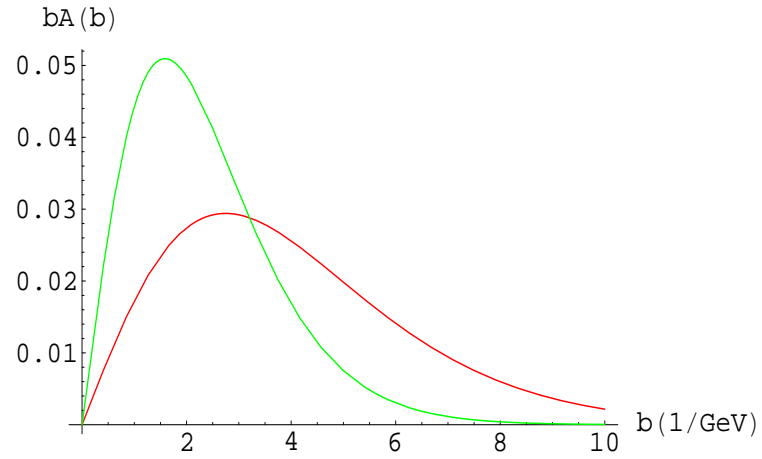
Figure 5.12: The plot of the overlap function $bA(b)$ for two values of proton radius $\mu^2 = 2.13\,\text{GeV}^2$ (green) and $\mu^2 = 0.71\,\text{GeV}^2$ (red).
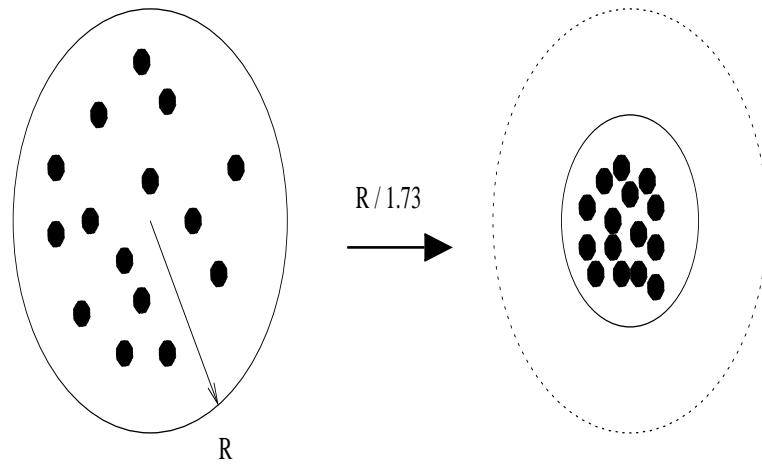
Figure 5.13: The decrease of the proton radius by the factor of 1.73 and its effect on the parton densities within the colliding hadrons at $b = 0$ (i.e. in a central collision).
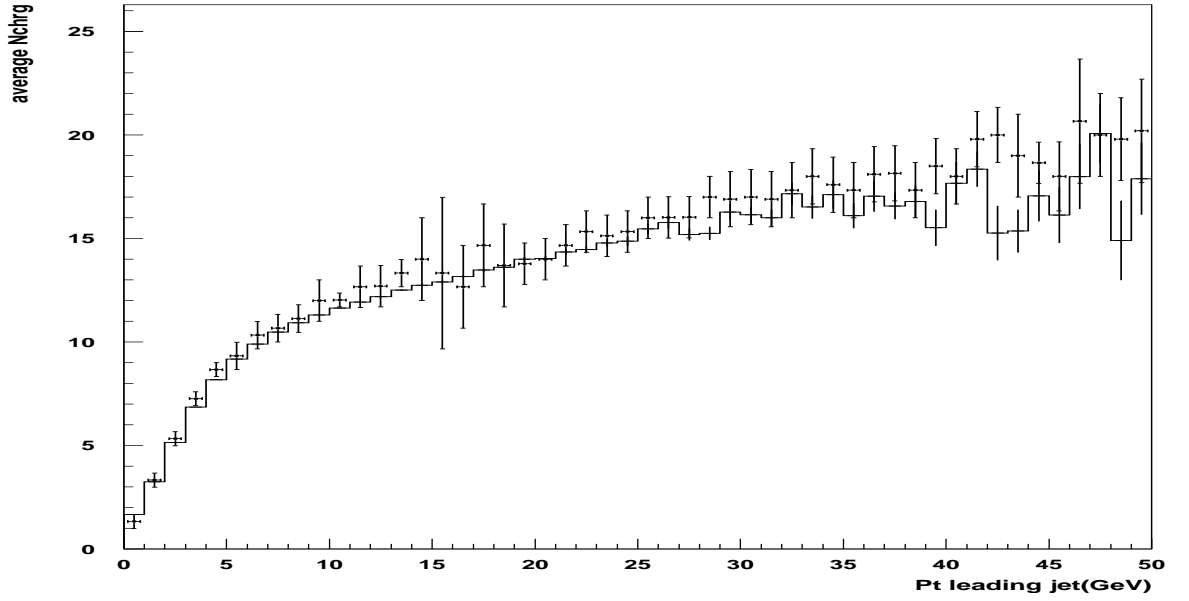
Figure 5.14: The average total number of charged particles in the event as a function of P_t (leading charged jet). HERWIG + Hard Interaction model (solid line) simulated data (with reduced proton radius), experimental CDF data [35] (data points).
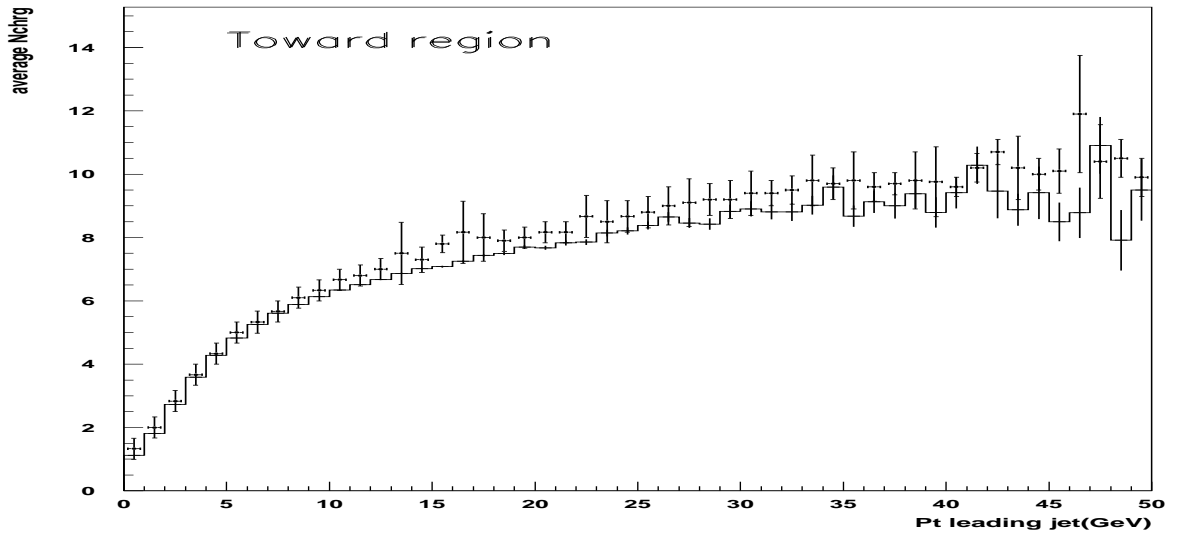
Figure 5.15: The average number of charged particles as a function of P_t (leading charged jet) in the toward region. HERWIG + Hard Interaction model (solid line) simulated data (with $p_{tmin} = 3$ GeV and reduced proton radius), experimental CDF data [35] (data points).
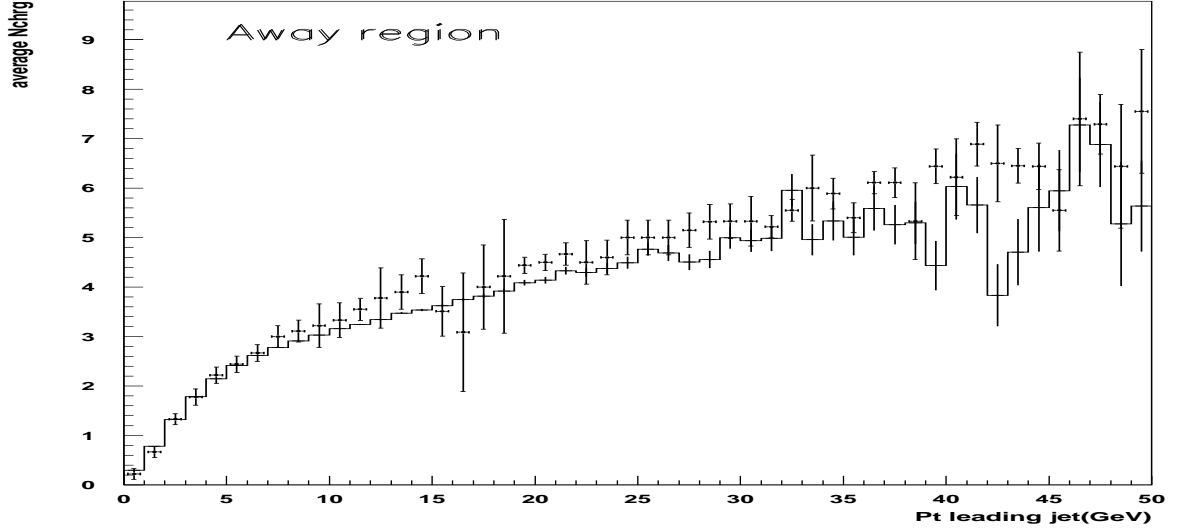
Figure 5.16: The average number of charged particles as a function of P_t (leading charged jet) in the away region. HERWIG + Hard Interaction model (solid line) simulated data (with $p_{tmin} = 3$ GeV and reduced proton radius), experimental CDF data [35] (data points).
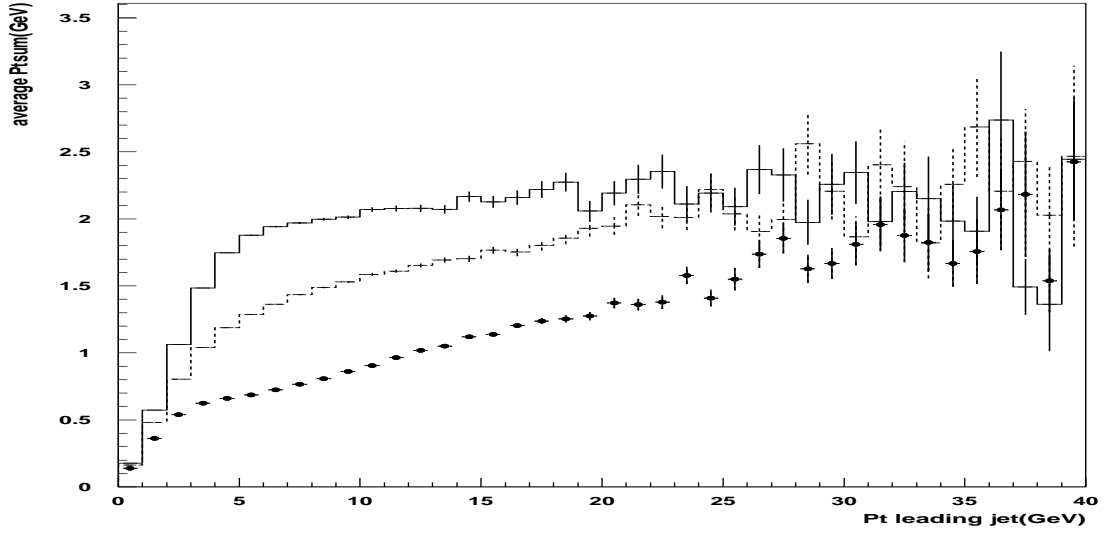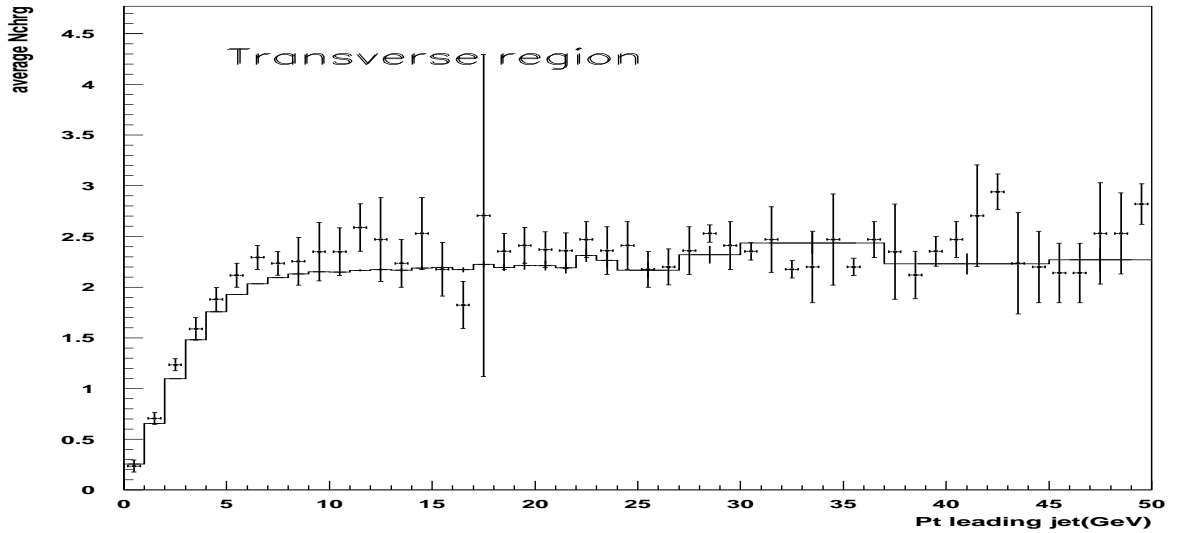

Figure 5.17: The average number of charged particles as a function of P_t (leading charged jet) in the transverse region. HERWIG + Hard Interaction model (solid line) simulated data (with $p_{tmin} = 3$ GeV and reduced proton radius), experimental CDF data [35] (data points).
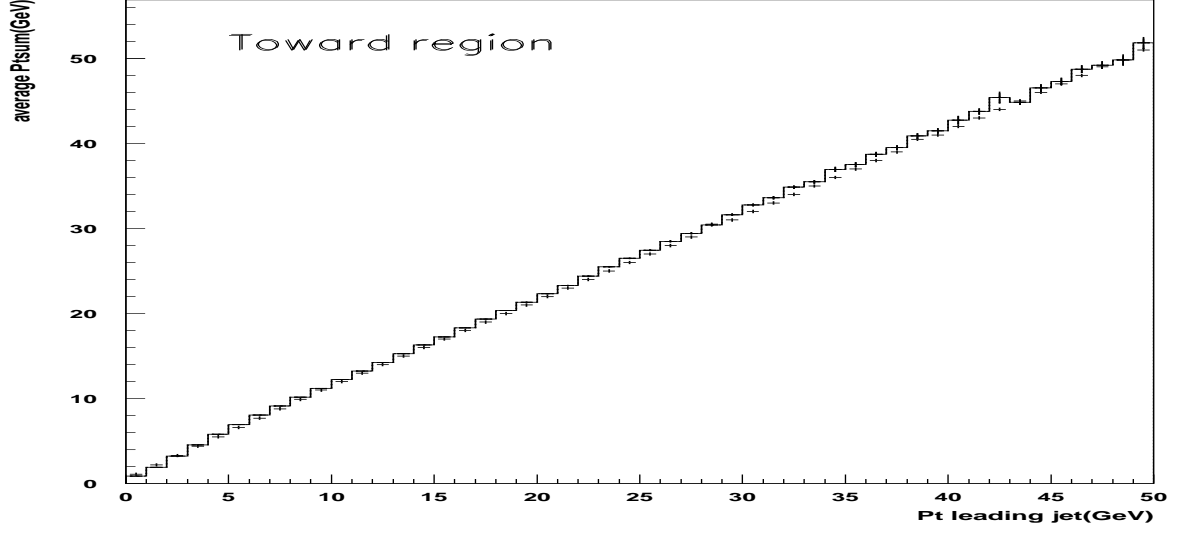
Figure 5.18: The average P_t sum of charged particles as a function of P_t (leading charged jet) in the toward region. HERWIG + Hard Interaction model (solid line) simulated data (with $p_{tmin} = 3$ GeV and reduced proton radius), experimental CDF data [35] (data points).
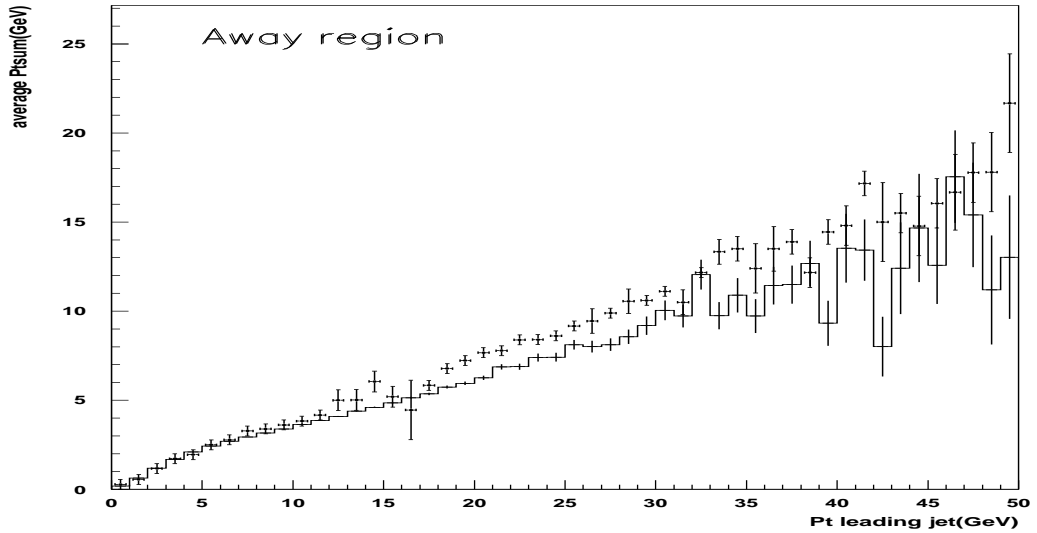
Figure 5.19: The average P_t sum of charged particles as a function of P_t (leading charged jet) in the away region. HERWIG + Hard Interaction model (solid line) simulated data (with $p_{tmin} = 3$ GeV and reduced proton radius), experimental CDF data [35] (data points).
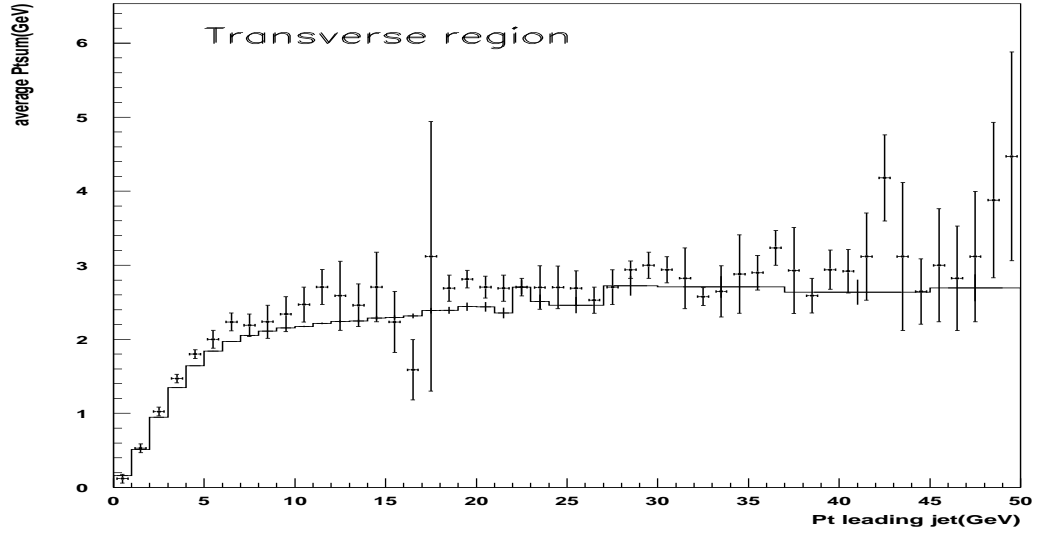
Figure 5.20: The average P_t sum of charged particles as a function of P_t (leading charged jet) in the transverse region. HERWIG + Hard Interaction model (solid line) simulated data (with $p_{tmin} = 3$ GeV and reduced proton radius), experimental CDF data [35] (data points).
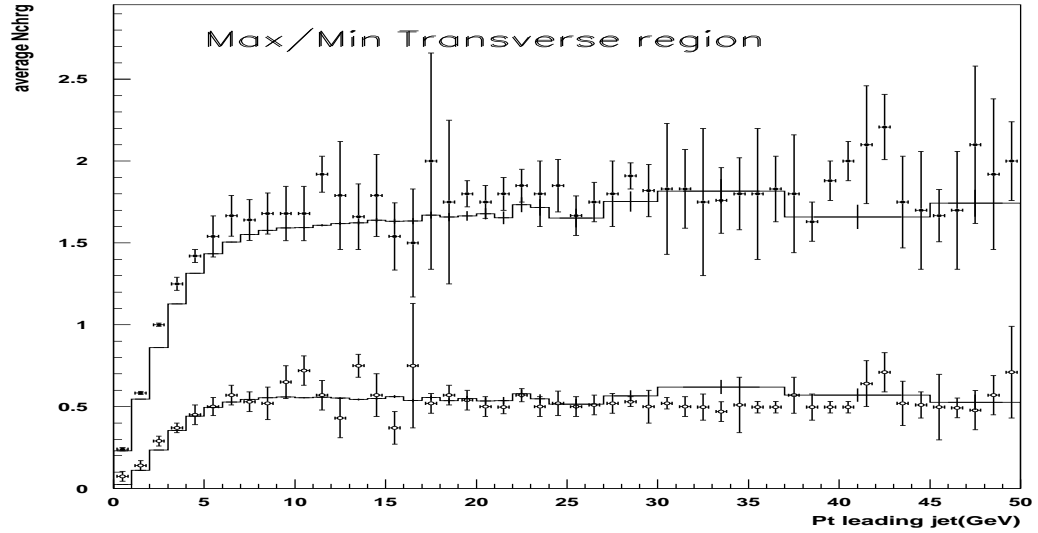
Figure 5.21: The average number of the trans-Max and trans-Min charged particles as a function of P_t (leading charged jet) in the transverse region. Solid (Max) and hollow (Min) circles experimental data, HERWIG + Hard Interaction model (solid line) simulated data (with $p_{tmin} = 3$ GeV and reduced proton radius), experimental CDF data [35] (data points).
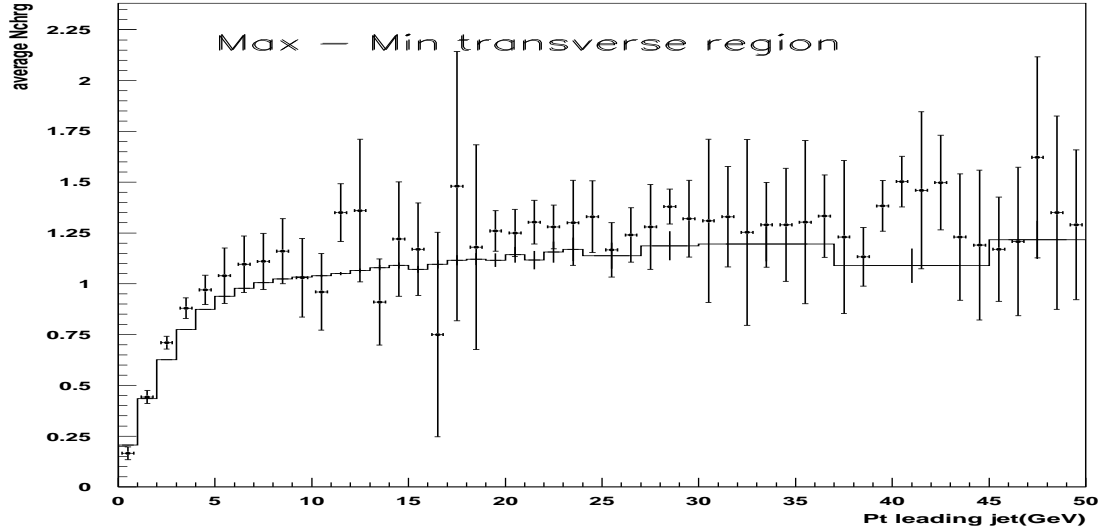
Figure 5.22: The average difference, trans-Max minus trans-Min, for the number of charged particles as a function of P_t (leading charged jet) in the transverse region. Solid points are the experimental data and the solid line the simulated data from HERWIG + Hard Interaction model (solid line) simulated data (with $p_{tmin} = 3$ GeV and reduced proton radius), experimental CDF data [35] (data points).

a better description of remnant-remnant interactions. For the same value of p_{tmin}, the model however does not describe correctly distributions of the average number of charged particles in the toward and away regions. The new proposed solution to this problem is to consider the radius of the proton as parameter. By decreasing the proton radius by a factor of 1.73 we have obtained a good description of the overall event structure as has been shown in Section 5.2.3. However the reason for changing the proton radius is not clear. Furthermore it is very doubtful that such an approach will lead to any successful predictive method for simulating hadron-hadron interactions at different centre-of-mass energies. In the next chapter we propose an alternative path to the one taken here. We propose a simple eikonal model which contains in its formalism both the Hard Multiparton model, described in this chapter, and a non-perturbative soft part. The main motivation for such a model is to obtain a predictive tool capable of describing the overall event structure in hadron-lepton and hadron-hadron collisions over a wide range of energies from the SPS experiments up to the LHC.

Chapter 6

Eikonal Model

6.1 Introduction

In Chapters 4 and 5 two different models for the simulation of particle production in remnant-remnant interactions were used as complement to the HERWIG QCD two to two parton-parton interaction subprocess (together with its full parton showering and hadronisation models). The performance of the two models was evaluated by comparison to experimental data on charged particle correlations in azimuthal angle. In this chapter (see Section 6.2) we introduce a new parameter free Eikonal Monte Carlo model (running in conjunction with HERWIG) [53] to simulate multiparticle production in hadron-hadron interactions. The new model contains only the value of the total cross section as a phenomenological input. In Section 6.5 we use the same analysis of charged particle correlation as was presented in Chapters 4 and 5 to evaluate the performance of our new model by comparison with the CDF experimental data. In Section 6.5.1 we compare the results obtained with the new Eikonal model to those in Chapters 4 and 5. Finally in Section 6.5.2 we use the new Eikonal model to predict the underlying event activity that should be expected at the LHC.

6.2 Introduction to the Eikonal Model

In this section we will review some well known expressions for cross sections within the eikonal approximation, which we will use as the basic framework for our model.

At high energies, particle scattering can be described using geometrical models since the wavelength of the particles is much smaller than their transverse size. The scattering angle θ_{CM} between two particles in their center-of-mass frame is given by

$$t = q^2 = -4k^2 \sin^2\left(\frac{\theta}{2}\right), \tag{6.1}$$

where q is the momentum transfer. Neglecting effects depending on the spin of the scattering particles and using the conservation of the angular momentum we can use

the partial wave expansion to express the scattering amplitude $A(s,t)$ as

$$A(s,t) = 16\pi \sum_{l=0}^{\infty} (2l+1)a_l(s)P_l(\cos\theta), \tag{6.2}$$

where $a_l(s)$ is the amplitude of the l-th partial wave. In the geometrical picture of scattering we can express the angular momentum l (large at high energies) as a function of the impact parameter b

$$l = \mid \mathbf{k} \times \mathbf{b} \mid . \tag{6.3}$$

Since $\mathbf{b}$ and $\mathbf{k}$ are perpendicular to each other, we have $l = kb$.

At high energies the number of partial waves contributing to the scattering increases and eq.6.2 can be approximated by its integral form

$$A(s,t) = 16\pi \int_0^{\infty} dl (2l+1)a_l(s)P_l(\cos\theta), \tag{6.4}$$

considering that $\sum_l \to \int dl \to \int kdb$, for large l.

Using
$$P_l\big(\cos(\theta)\big) \to J_0\big((2l+1)\sin\left(\frac{\theta}{2}\right)\big) \ \text{ for } \ l \to \infty, \tag{6.5}$$

and
$$J_0(z) = \frac{1}{2\pi} \int_0^{2\pi} d\varphi \exp\left(iz\cos\varphi\right) \ \text{ with } \ \mathbf{b.q} = \mathbf{b.q_\perp} = \mathbf{b.q_\perp}\cos\varphi, \tag{6.6}$$

we can rewrite eq.6.4 as

$$A(s,t) = 4\pi s \int db^2 a(\mathbf{b},s)e^{i\mathbf{q.b}}, \tag{6.7}$$

where $a(\mathbf{b},s) = a_l(s)\mid_{l=kb}$, is the impact parameter amplitude and $q_\perp$ is the transverse component of momentum transfer in the center-of-mass frame.

The optical theorem (see Chapter 1) relates the imaginary part of the elastic scattering amplitude $A(s,t=0)$ to the total cross section σ_{tot} through a unitarity relation :

$$\sigma_{tot} = \frac{1}{s}Im(A(s,t=0)). \tag{6.8}$$

Using the optical theorem, eq.6.8, we can express the cross sections as:

$$\sigma_{tot} = 4\pi \int db^2 Im(a(\mathbf{b}, s)), \tag{6.9}$$

$$\sigma_{ela} = 4\pi \int db^2 |a(\mathbf{b}, s)|^2, \tag{6.10}$$

$$\sigma_{inel} = \sigma_{tot} - \sigma_{ela}. \tag{6.11}$$

We express the elastic amplitude in terms of the eikonal function, $\chi(b, s)$, as [12]:

$$a(\mathbf{b}, s) = \frac{e^{-\chi(\mathbf{b}, s)} - 1}{2i}. \tag{6.12}$$

With the eikonal expression eq.6.12 we can write the cross sections as :

$$\sigma_{tot} = 2\pi \int_0^\infty db^2 [1 - e^{-\chi(b, s)}], \tag{6.13}$$

$$\sigma_{ela} = \pi \int_0^\infty db^2 \left| [1 - e^{-\chi(b, s)}] \right|^2, \tag{6.14}$$

$$\sigma_{inel} = \pi \int_0^\infty db^2 [1 - e^{-2\chi(b, s)}]. \tag{6.15}$$

We choose the total cross section in eq.6.13 as the only phenomenological input to our model. In the next section we will specify the expression for $\chi(b, s)$.

6.3   Expression for the eikonal

In this section, we will give an expression for the eikonal $\chi(\mathbf{b}, s)$ in eq.6.13 and provide some justification for it.

Comparing the eikonal expression in eq.6.15 with the expression in eq.5.9 we define the hard part of the eikonal as :

$$\chi_{QCD}(b, s) = \frac{1}{2} \langle n(b, s_{p\overline{p}}) \rangle, \tag{6.16}$$

where the expression for $\langle n(b, s_{p\overline{p}}) \rangle$ is given in eq.5.3.

The QCD perturbative 2-to-2 parton-parton differential cross section diverges as the transverse momentum of the scattering, p_t, goes to zero. One must then fix a

minimum value p_{tmin} for p_t large enough for perturbative QCD to be reliable. This dependence of the perturbative QCD differential cross section implies that the eikonalised hard inelastic cross section would also depend on the arbitrary value chosen for the minimum p_t.

6.3.1   The expression for $\chi_{total}(b, s)$

Our goal is to formulate a model which will be, to a certain degree, independent of the p_{tmin} cutoff. To this end, to $\chi_{QCD}(b, s_{p\overline{p}})$ which describes hard interactions with $p_t \geq p_{tmin}$, we will add $\chi_{soft}(b, s_{p\overline{p}})$, which will describe interactions with $0 \leq p_t \leq p_{tmin}$. The full eikonal can now be expressed as :

$$\chi_{total}(b, s) = \chi_{QCD}(b, s_{p\overline{p}}) + \chi_{soft}(b, s_{p\overline{p}}). \tag{6.17}$$

To specify $\chi_{soft}(b, s_{p\overline{p}})$ we will use a model introduced by Chou and Yang [55] and Durand and Pi [52], which postulates that the elastic scattering is the shadow of the absorption resulting from the passage of one hadronic mass distribution through another. The transverse distribution of the matter is assumed then to have the same shape as the charge distribution, as measured by the electromagnetic form factor, so that $\chi_{soft}(b, s)$ is of the form:

$$\chi_{soft} = C(s_{p\overline{p}})A(b), \tag{6.18}$$

where $C(s_{p\overline{p}}) = 1/2\sigma_{SOFT}^{inc}(s_{p\overline{p}})$, and $\sigma_{SOFT}^{inc}(s_{p\overline{p}})$ is a constant to be determined below, and $A(b)$ is given in eq.5.5.

The eikonal now consists of two parts, the hard,

$$\chi_{QCD} = \frac{1}{2}\sigma_H^{inc}(s_{p\overline{p}})A(b), \tag{6.19}$$

and the soft,

$$\chi_{soft} = \frac{1}{2}\sigma_{SOFT}^{inc}(s_{p\overline{p}})A(b). \tag{6.20}$$

If we now consider the total cross section in eq.6.13 with $\chi(b, s) = \chi_{total}(b, s)$ and assume $\chi_{total}(b, s)$ to be small, we can expand the exponential in eq.6.13. Integrating over the

impact parameter b we get:

$$\sigma_{total}(s_{p\bar{p}}) \approx \sigma_{SOFT}^{inc}(s_{p\bar{p}}) + \sigma_H^{inc}(s_{p\bar{p}}) \tag{6.21}$$

Following this approximation we will assume that our $\sigma_{SOFT}^{inc}(s_{p\bar{p}})$ is a bare non-perturbative cross section for a soft proton-antiproton interaction. Since $\sigma_{SOFT}^{inc}(s_{p\bar{p}})$, the bare soft cross section in eq.6.20, is not directly calculable in our model, its value can be determined from the experimental data, i.e. by using the total cross section measured by the CDF collaboration [54].

To give a prediction for future LHC data we will rely on the Donnachie-Landshoff model of the Pomeron [15] which fits successfully all the experimental data on total cross section for proton-proton scattering,

$$\sigma_{tot}(s_{pp}) = \sigma_{tot}(s_0) \left(\frac{s}{s_0}\right)^{\alpha_p(0)-1}, \tag{6.22}$$

where $\alpha_p(t) = 1 + \epsilon + \alpha_p' t$ with $\epsilon = 0.08$ and $\alpha_p' = 0.25$ GeV^{-2}. Assuming $\sigma_{tot}(s_{pp}) = \sigma_{tot}(s_{p\bar{p}})$ at high energy, the total cross section at the LHC can then be written as

$$\sigma_{tot}(s_{pp}) = \sigma_{tot}(s_{CDF}) \left(\frac{\sqrt{s_{pp}}}{1800}\right)^{2\times 0.08}. \tag{6.23}$$

We consider the value of the total cross section as the only phenomenological input to our model (in addition to those that are already in HERWIG [19] and the multiparton hard model [42], which we leave at their default values).

In addition the model contains the following assumptions :

• there can be more than one soft interaction in a soft proton-antiproton interaction.

• the probability distribution for having m and only m soft scatters in a given proton-antiproton interaction P_m obeys the Poissonian distribution (i.e. multiple soft scatters are uncorrelated),

$$P_m = \frac{(2\chi_{soft})^m}{m!} \exp{(-2\chi_{soft})}. \tag{6.24}$$

- the hard and soft scatters are assumed to be independent i.e the probability distribution for having h hard, and m soft, scatters is given by $P_{h,m}$:

$$P_{h,m}(b, s_{p\overline{p}}) = \frac{(2\chi_{QCD})^h}{h!} \frac{(2\chi_{soft})^m}{m!} \exp{(-2\chi_{total})}. \tag{6.25}$$

We can now express cross sections as:

$$\sigma_{inel}(s_{p\overline{p}}) = \pi \int db^2 \sum_{h+m\geq 1} P_{h,m}(b, s_{p\overline{p}}) = \pi \int_0^\infty db^2 (1 - e^{-2\chi_{total}(b,s_{p\overline{p}})}), \tag{6.26}$$

the inelastic cross section with at least one hard scattering:

$$\sigma_{h,inel}(s_{p\overline{p}}) = \pi \int db^2 \sum_{h\geq 1, m\geq 0} P_{h,m}(b, s_{p\overline{p}}) = \pi \int_0^\infty db^2 (1 - e^{-2\chi_{QCD}(b,s_{p\overline{p}})}), \tag{6.27}$$

and the total cross section:

$$\sigma_{tot}(s_{p\overline{p}}) = 2\pi \int_0^\infty db^2 (1 - e^{-\chi_{total}(b,s_{p\overline{p}})}). \tag{6.28}$$

The $\sigma_{SOFT}^{inc}(s_{p\overline{p}})$ in eq.6.20 is then determined by fixing its value so that the the total cross section in eq.6.28, at some p_{tmin}, is equal to the total cross section measured by the CDF collaboration ($\sigma_{total\ CDF} = 81.8\pm2.3$mb) (see Section 6.5 for different values of $\sigma_{SOFT}^{inc}(s_{p\overline{p}})$ and p_{tmin} used).

In order to have a realistic Monte Carlo event generator we have implemented our eikonal model as part of the HERWIG Monte Carlo program with the full use of its hadronisation model and parton showering properties.

6.4 The Monte Carlo implementation of hard and soft processes

In the following sections we will describe soft processes in detail. The hard processes are as in [42] (see Chapter 5). Before we start with the simulation of an event we need to fix $\sigma_{SOFT}^{inc}(s_{p\overline{p}})$, the bare soft cross section (as explained in Section 6.3.1). Then by drawing from the probability distribution eq.6.25 we decide the number of soft and hard interactions in a given event. The event simulation can then start with HERWIG generating a hard subprocess followed by multiparton ones (see Chapter 4). Once the multiple hard scatters have been exhausted the soft multiple scatters are generated.

6.4.1 Assumptions behind the soft subprocess

At high $s_{p\overline{p}}$ (center of mass energy) and low Q scale of interaction, i.e low-x, we might expect a proliferation of soft gluons. In order to simulate each soft subprocess we assume that the bare soft cross section $\sigma_{SOFT}^{inc}(s_{p\overline{p}})$, corresponds to a soft interaction between two incoming soft gluons. That is, we model the soft inelastic collision between two remnants as a soft elastic collision between two partons within them (see fig.6.1).

All soft gluons carry a colour charge and have an effective mass m_g (inspired by HERWIG's model of the hadronisation of the outgoing gluons). The two outgoing effective gluons in fig.6.1 are on mass shell and colour connected to the remnants and to each other, as shown in fig.6.1, each gluon colour(anticolour) is connected to its anticolour(colour) partner.

Because we wanted to keep the implementation of our model as simple as possible we have decided to sever the colour connections between the remnants and the outgoing soft gluons (see fig.6.2, dashed solid lines show severed colour connections). We expect this to be a reasonable approximation since the largest part of the phase space, in the
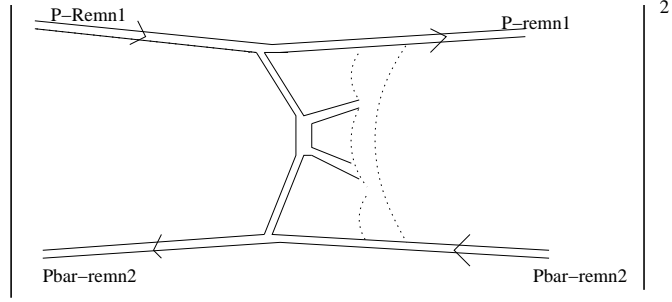
Figure 6.1: $\sigma_{SOFT}^{inc}(s_{p\overline{p}})$ corresponds to a soft collision between the two soft gluons (full color picture). Remnants are also connected to each other via t channel gluon line.
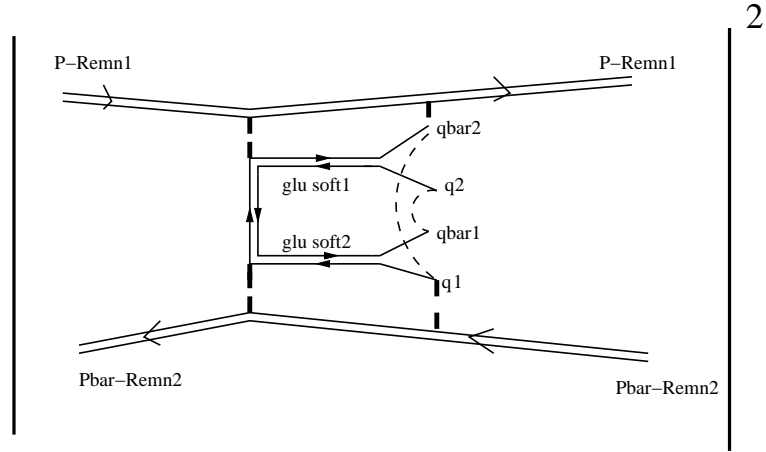
Figure 6.2: The soft collision between the two soft gluons, with dashed solid lines indicating the severed color connections between the remnants and the outgoing gluons, forming two clusters, $q_1\overline{q_2}$ and $q_2\overline{q_2}$.

gap between the two remnants, will be filled by final state hadrons produced by the colour field stretched in between the two outgoing soft gluons (note that in both figs 6.1 and 6.2, two colour lines stretch across the central region). In the hadronisation phase the two outgoing soft gluons form two clusters $(q_1\overline{q}_2, q_2\overline{q}_1)$ (see fig.6.2) which are decayed into final state hadrons (using HERWIG's cluster hadronisation model [19]).

6.4.2 Implementation of the soft process

Following fig.6.2, for each soft remnant-remnant interaction we generate two soft effective gluons, on mass shell, with previously tuned masses $m_g = 0.75$ GeV used in the HERWIG hadronisation model [19]. For each soft interaction we will go through the following chain of events; first the maximum fractional longitudinal momentum allowed for each soft gluon ($x_{glumax\ 1,2}$) is determined using the light-cone definition of the longitudinal momentum fraction x of the two remnants,

$$x_{glumax\ 1,2} = x_{remn\ 1,2} = \frac{E_{remn1,2} + P_{z_{remn1,2}}}{E_{p,\overline{p}} + P_{z_{p,\overline{p}}}}. \tag{6.29}$$

The longitudinal momentum fractions for each soft gluon is then sampled from an $f(x)^{sea\ partons} = \frac{1}{x}$ distribution (which we consider reasonable since we expect the effective gluons to be Regge-like) between some minimum value x_{min} (the cutoff) and the maximum value, $x_{glumax\ 1,2}$, allowed by eq.6.29. Once their fractional longitudinal momentum has been determined, a transverse momentum for each soft gluon is then sampled from a Gaussian distribution for values of p_t, $0 \leq p_t \leq p_{tmin}$, according to

$$\frac{d\sigma_{soft\ gluons}}{d^2 p_t} = D \exp\left(-\beta p_t^2\right), 0 \leq p_t \leq p_{tmin}. \tag{6.30}$$

Before sampling the transverse momentum of each soft gluon, we will have to determine the slope β of the particle p_t distribution in the central region and the normalisation constant D in eq.6.30. We impose then another condition on the p_t distribution, namely, that the transverse momentum distribution in p_t of soft and hard gluons should be continuous at the p_t cutoff eq.6.31 (the same procedure was implemented in [57]),

$$\frac{d\sigma_{soft\ gluons}}{d^2 p_t}\Big|_{p_t = p_{tmin}} = \frac{d\sigma_{hard\ gluons}}{d^2 p_t}\Big|_{p_t = p_{tmin}}. \tag{6.31}$$

We have then to solve two equations with two unknowns. The first condition is that the number of soft gluons should correspond to the soft cross section $\sigma_{SOFT}^{inc}(s_{p\overline{p}})$:

$$\int_0^{p_{tmin}} d^2 p_t D \exp\left(-\beta p_t^2\right) = \sigma_{SOFT}^{inc}(s_{p\overline{p}}), \tag{6.32}$$

the second condition is that of the smooth transition between the soft and hard perturbative gluons' transverse momentum distributions * at the value of p_t cutoff eq.6.31, re-expressed as:

$$D \exp\left(-\beta p_{tmin}^2\right) = \frac{d\sigma\left(s_{p\bar{p}}, p_{tmin}\right)}{dp_{tmin}^2},\qquad(6.33)$$

where $\frac{d\sigma(s_{p\bar{p}}, p_{tmin})}{dp_{tmin}^2}$ is the full differential parton-parton hard cross section calculated at the value of $p_t = p_{tmin}$.

In order to determine the four momentum of each outgoing remnant and each soft gluon, two additional conditions need to be satisfied simultaneously; that of the total energy-momentum conservation between the initial beam-beam remnants ($\text{remn}_{1,2}$) and final ($\text{remn}_{1,2}$ + soft gluons) states and that the outgoing soft gluons and remnants are on mass shell, with each remnant having the same mass before and after the soft interaction.

Once all four momenta of the outgoing remnants and soft gluons have been determined a new maximum longitudinal fractional momentum $x_{glumax\ 1,2}$ is calculated, according to eq.6.29, for the next pair of soft gluons. The same chain of events, as described above, is then iterated until all soft interactions have been generated. If energy-momentum conservation is violated the scattering is vetoed.

---

*As shown in figs.6.3-6.5, although hard $p_t > p_{tmin}$ and soft $p_t < p_{tmin}$, subsequent event processing smears them slightly. Nevertheless they seem to be well matched. Although the soft distribution has the functional form of a Gaussian distribution, the constraints on it actually require β to be negative (for small p_{tmin}), leading to a peaking at around p_{tmin}. This could provide an explination for why the Hard Multiparton model [42] performs better than might naively be expected
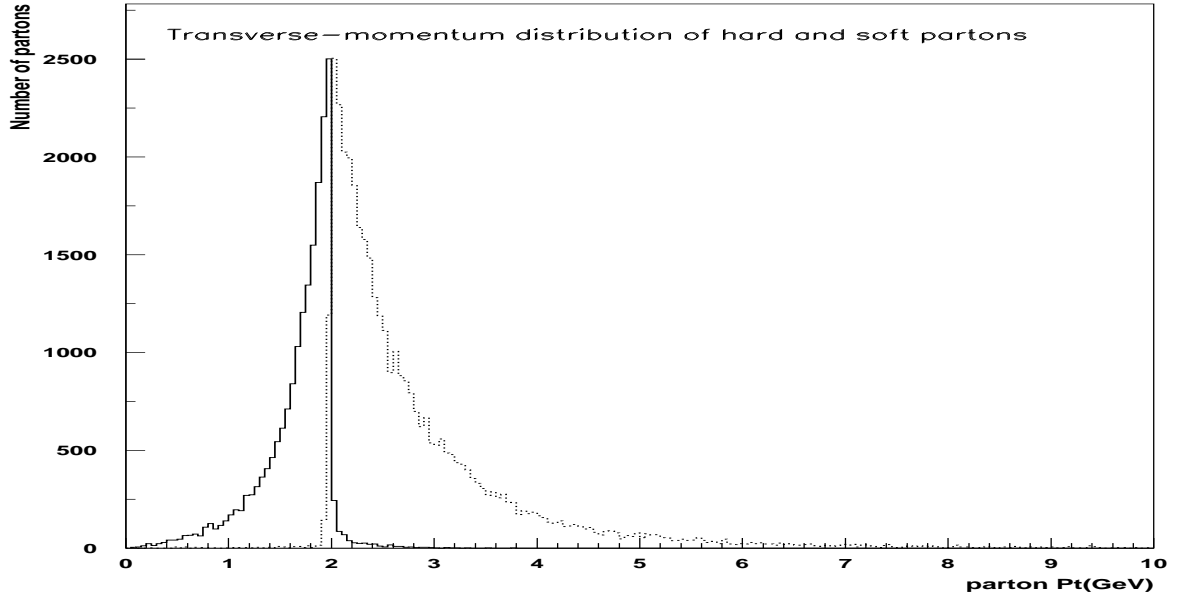
Figure 6.3: Transverse momentum distributions of the soft (solid line) and hard (dashed line) partons at p_{tmin}=2.0 GeV.

6.5 Study of particle correlations in azimuthal angle

In this section we use the same jet algorithm and analysis on charged particle correlations as was presented in Chapters 5 and 6 to evaluate the effect of the eikonal formalism on the particle correlation in azimuthal angle away in ϕ from the leading charged jet.

The toward and away region

Figs 6.6 and 6.12 show a good agreement between the eikonal model simulated and experimental data for the average total number of charged particles (including particles of the leading jet) as a function of the transverse momentum of the leading jet for values of p_{tmin} = 2.5 GeV and 3 GeV. However for a low value of p_{tmin} = 2 GeV the eikonal model does not generate enough charged particles as shown in fig.6.6. The
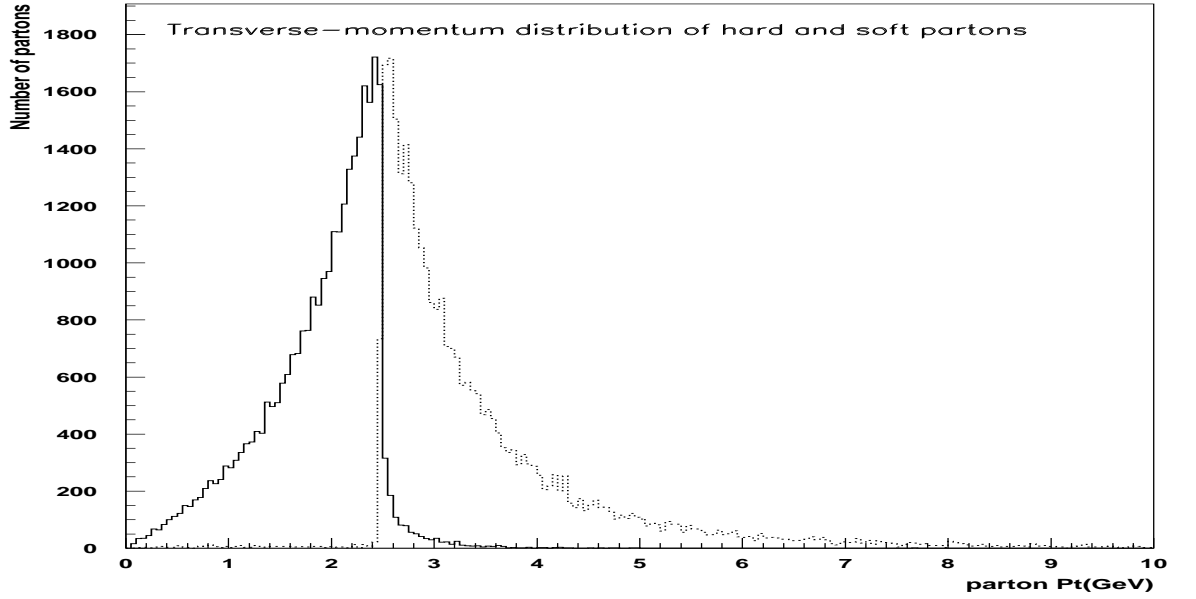
Figure 6.4: Transverse momentum distributions of the soft (solid line) and hard (dashed line) partons at p_{tmin}=2.5 GeV.

same pattern in simulated data (i.e. with low value of $p_{tmin} = 2$ GeV) is observed for the average number of charged particles in the toward and away regions (as shown in fig.6.7 and fig.6.8), and for the average p_t sum in the away region as shown in fig.6.11. This deficiency of the Eikonal model comes from the not so good performance of the Multiparton Hard part of the model for low value of $p_{tmin} = 2$ GeV as mentioned earlier in Chapter 5. However for values of $p_{tmin} = 2.5$ GeV and 3 GeV the eikonal model describes the experimental data in the toward and away region rather well as shown in figs 6.6 - 6.8 and figs 6.10 - 6.14.

The transverse region

A comparison between simulated (corrected) and experimental data is presented in fig.6.9, with $p_{tmin} = 2$ GeV and 3 GeV. The agreement shown in fig.6.9 and 6.19 is particularly important since the transverse region is the most sensitive to the under-lying event activity (we also show the agreement between the eikonal model ($p_{tmin} =$
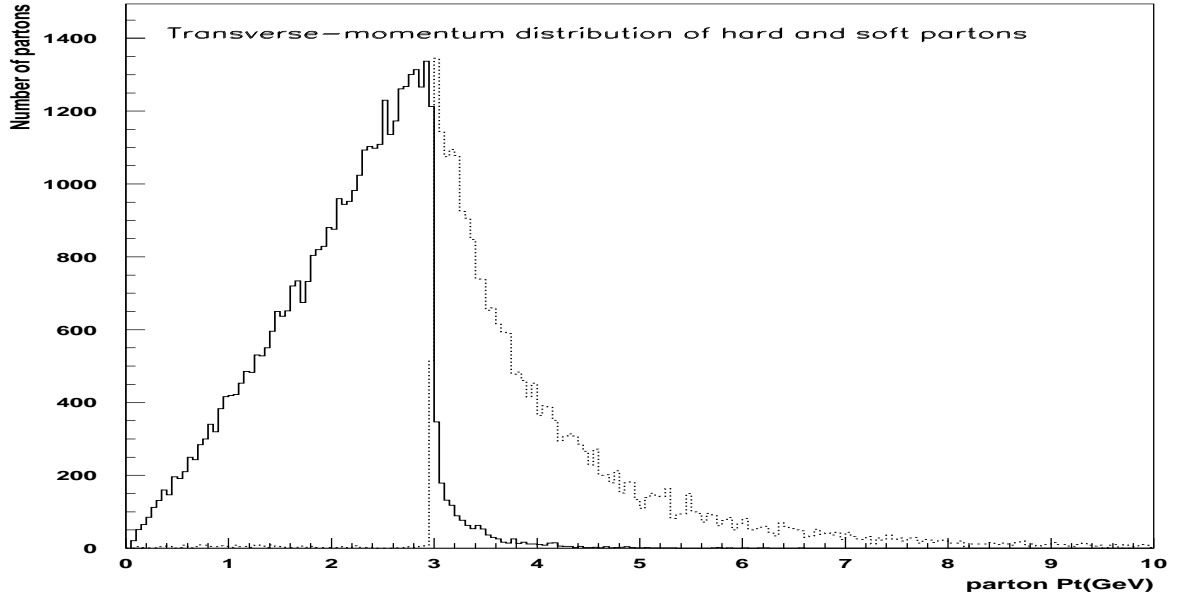
Figure 6.5: Transverse momentum distributions of the soft (solid line) and hard (dashed line) partons at p_{tmin}=3.0 GeV.

2.5 GeV) and experimental data in figs.6.15 and 6.16). In figs 6.20 - 6.22 we show a good agreement between the eikonal model (at p_{tmin} = 2.5 GeV) and experimental data in the two Max/Min regions. In figs.6.17 and 6.18 we compare our predictions in the transverse region with those of the two underlying event models (at p_{tmin} = 2.5 GeV), HERWIG + Underlying Event model [19], HERWIG + Multiparton Hard model [42]. As shown in figs.6.17 and 6.18, both HERWIG + Underlying Event model and HERWIG + Multiparton Hard model fail to produce enough activity for both the average number of charged particles and the average scalar p_t sum. In addition the HERWIG + Underlying Event model has a wrong (too steep) p_t dependence. Overall our eikonal model is in better agreement with the experimental data than either of the other two underlying event models. This result is even more significant since we did not fit to the experimental data but rather, make predictions based on the value of the total cross section used as phenomenological input to our model.

6.5.1   The invariance of the model to p_{tmin}

In the multiparton scattering model [42], the parameter p_{tmin} is a cutoff scale and plays a crucial role in determining the prediction of the model. In our eikonal model it is rather a matching scale between the hard and soft parts of the model. If the matching works perfectly, the results should be p_{tmin} independent.

To test the invariance of the eikonal model to its p_{tmin} parameter we simulate two sets of data, with two different values of $p_{tmin} = 2$ GeV and 3 GeV as shown in fig.6.19. The values of inclusive cross sections with the average number of soft and hard scatters are presented in table.1.

p_{tmin}(GeV)	$\sigma^{inc}_{SOFT}(s_{p\overline{p}})$(mb)	$\sigma^{inc}_{H}(s_{p\overline{p}})$(mb)	$\langle n_{soft}\rangle$	$\langle n_{hard}\rangle$
2.0	39.7	99.2	0.7	1.7
2.5	85.6	51.3	1.5	0.9
3.0	109.7	28.7	1.9	0.5

Table 6.1: Values of inclusive cross sections and average numbers of hard and soft scatters.

We show the results in comparision with the Hard Multiparton model in fig.6.19. We see that as expected the results in the multiparton hard model are strongly p_{tmin} dependent, with smaller values of p_{tmin} producing more activity. However, even the smallest value of p_{tmin} is well below the data and no value of p_{tmin} for which the hard part of HERWIG is reliable gives a good description of the data. In contrast, our eikonal model has a smaller p_{tmin} dependence, with the additional soft scatters providing extra activity to compensate for that lost from the hard scatters as p_{tmin} increases. However, we see that they actually overcompensate, with decreasing p_{tmin} leading to decreasing activity. This residual p_{tmin} dependence indicates that the matching of the soft and the hard parts of the model is still not perfect and can perhaps be improved with further refinements of the model. Nevertheless, we are satisfied that with such a simple, physically motivated and parameter free model, we have provided a significant improvement to the p_{tmin} dependence and the description of data.
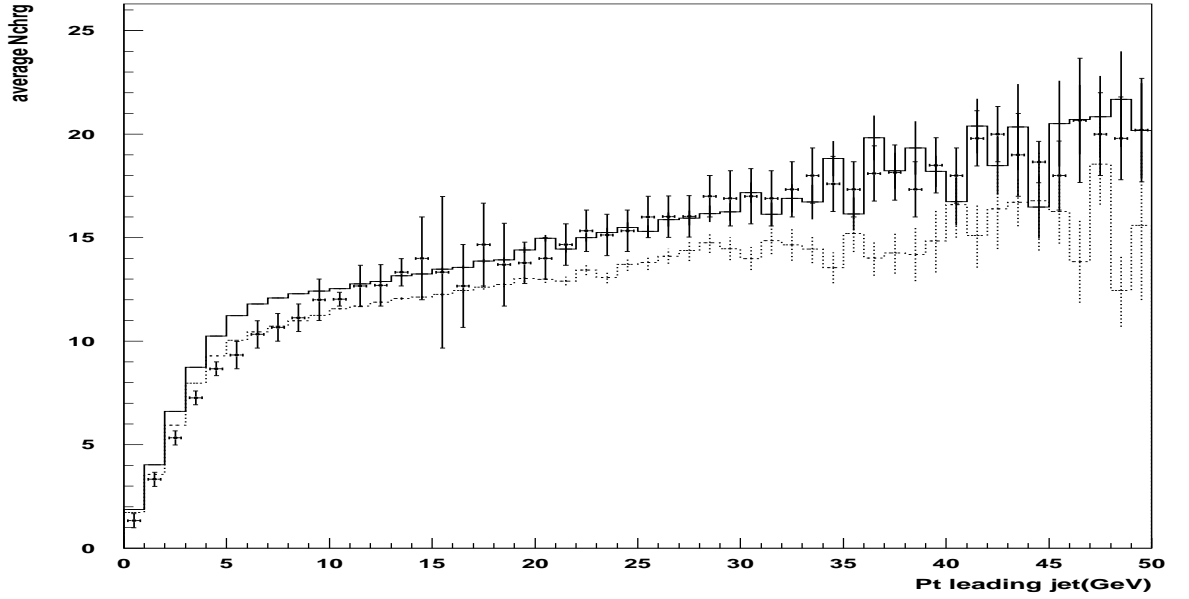
Figure 6.6: The average total number of charged particles in the event as a function of P_t (leading charged jet). HERWIG + Eikonal model simulated data $p_{tmin} = 3.0$ GeV (solid line) and 2.0 GeV (dotted line), experimental CDF data [35] (data points).

At this stage our model contains a single cutoff scale p_{tmin} set equal to the minimum hard scale (i.e. PTMIN) used in HERWIG for hard jet production. This limits the efficiency of our model to simulate the multiparton contribution to high p_t jets. Normally the two scales, one controlling the amount of multiple interactions and other the scale of parton-parton interactions, are independent. As shown in Chapter 5.2.2, we can avoid this efficiency problem by considering the hard-multiple part contribution to high p_t jets as small (at $p_{tmin} = 3$ GeV). We use this approximation to simulate higher p_t jet data by setting our p_{tmin} value respectively to 20, 40, 60 and 80 GeV thus making the contribution of the hard multiparton part negligible. In fig.6.23 we show the agreement of our simulated data with the CDF experimental data from [35, 41]. To test the validity of our approximation we show in fig.6.24 the contribution of full multiple hard and soft interactions for jets with $p_t <$ 50 GeV (at $p_{tmin} = 3$ GeV), which does not indicates a significant difference with data simulated for higher p_t using only the soft multiparton part of our model.
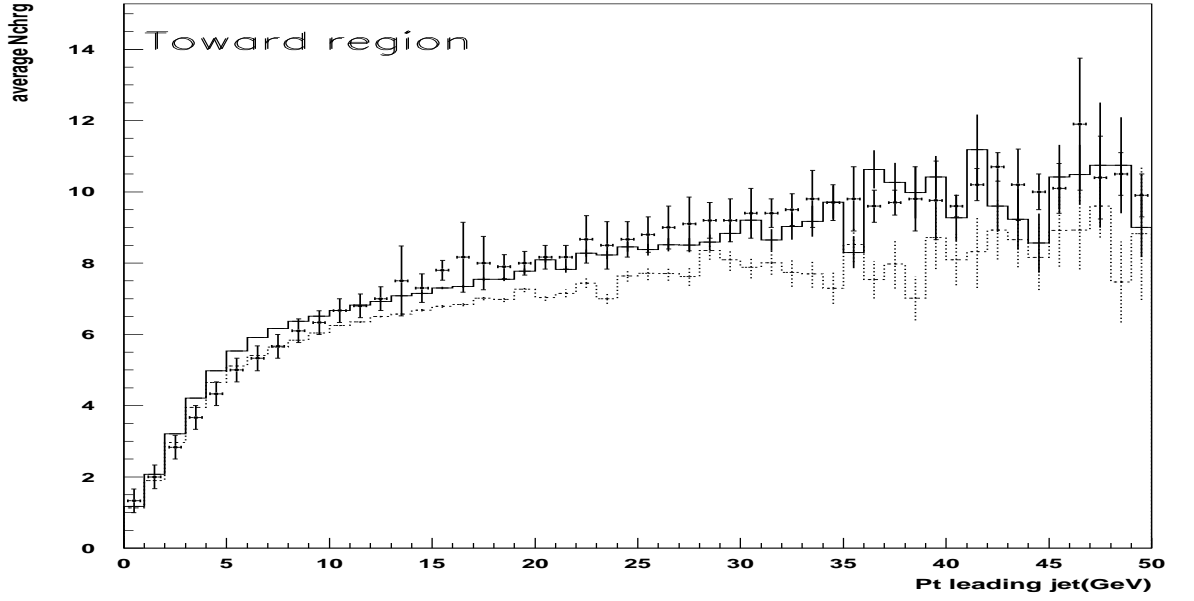
Figure 6.7: The average number of charged particles as a function of P_t (leading charged jet) in the toward region. HERWIG + Eikonal model simulated data $p_{tmin} = 3.0$ GeV (solid line) and 2.0 GeV (dotted line), experimental CDF data [35] (data points).
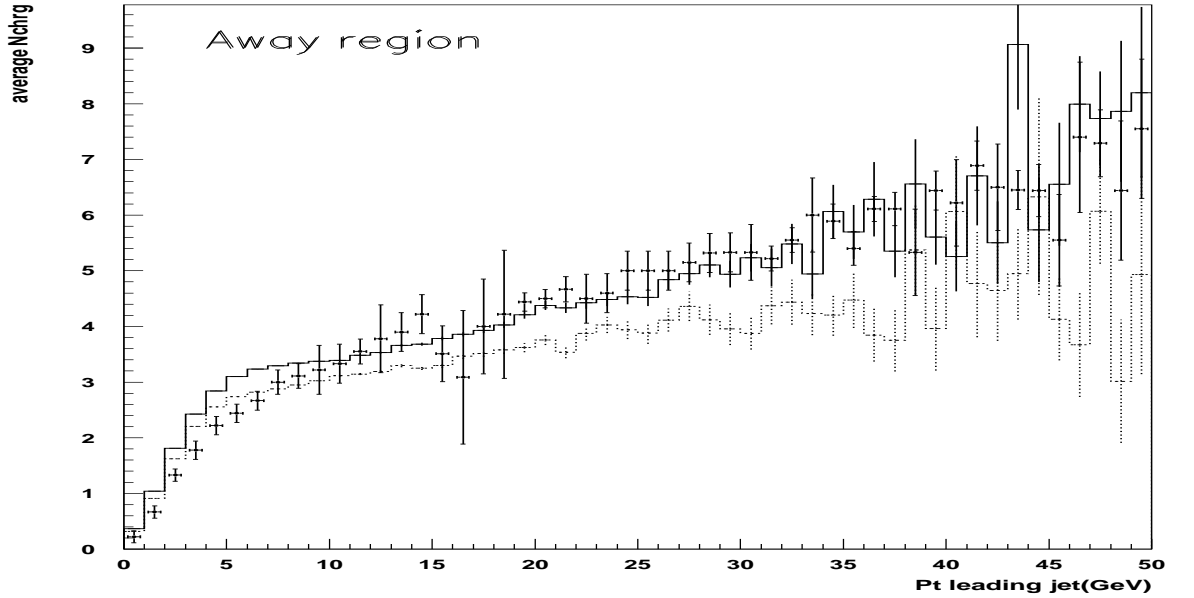

Figure 6.8: The average number of charged particles as a function of P_t (leading charged jet) in the away region. HERWIG + Eikonal model simulated data $p_{tmin} = 3.0$ GeV (solid line) and 2.0 GeV(dotted line), experimental CDF data [35] (data points).
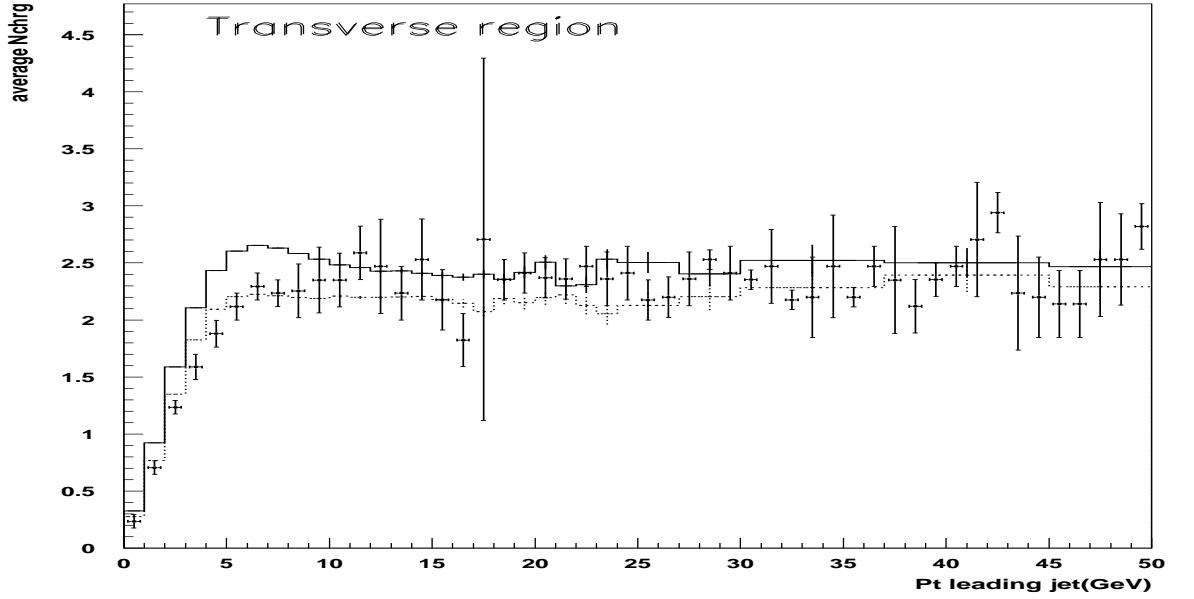
Figure 6.9: The average number of charged particles as a function of P_t (leading charged jet) in the transverse region. HERWIG + Eikonal model simulated data $p_{tmin} = 3.0$ GeV (solid line) and 2.0 GeV (dotted line), experimental CDF data [35] (data points).

Figure 6.10: The average P_t sum of charged particles as a function of P_t (leading charged jet) in the toward region. HERWIG + Eikonal model simulated data $p_{tmin} = 3.0$ GeV (solid line) and 2.0 GeV (dotted line), experimental CDF data [35] (data points).
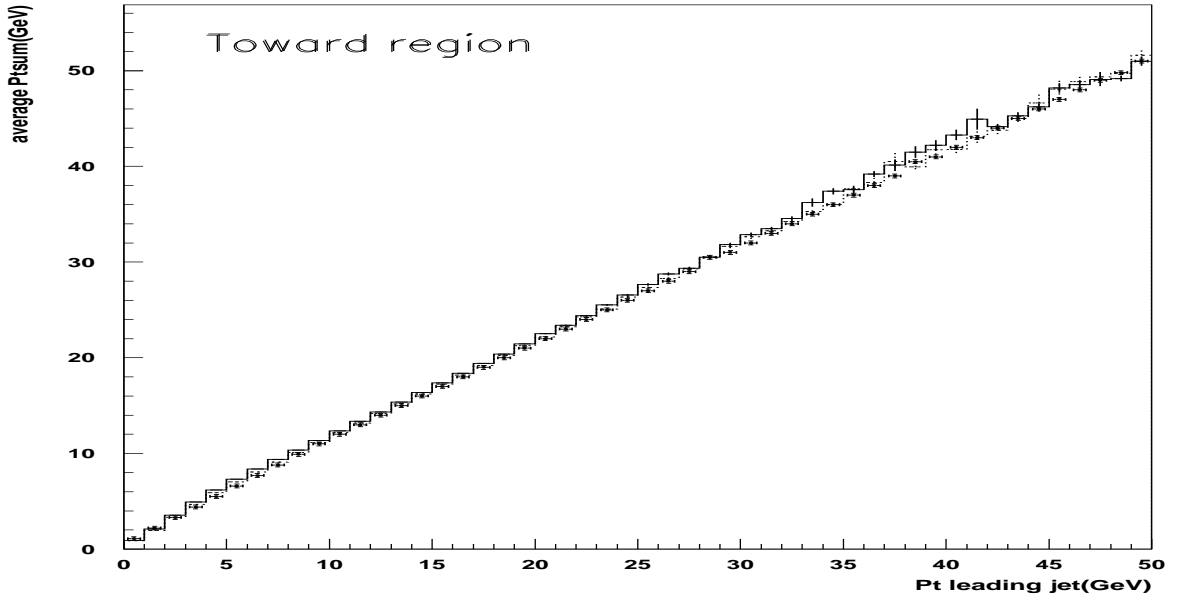
Figure 6.11: The average P_t sum of charged particles as a function of P_t (leading charged jet) in the away region. HERWIG + Eikonal model simulated data $p_{tmin} = 3.0$ GeV (solid line) and 2.0 GeV (dotted line), experimental CDF data [35] (data points).
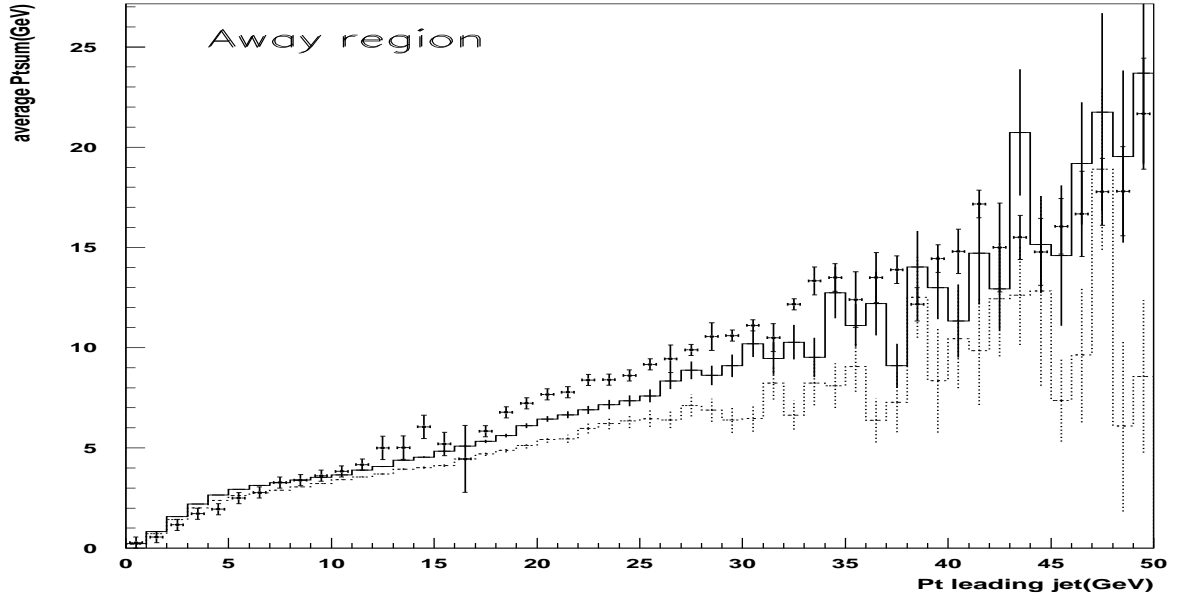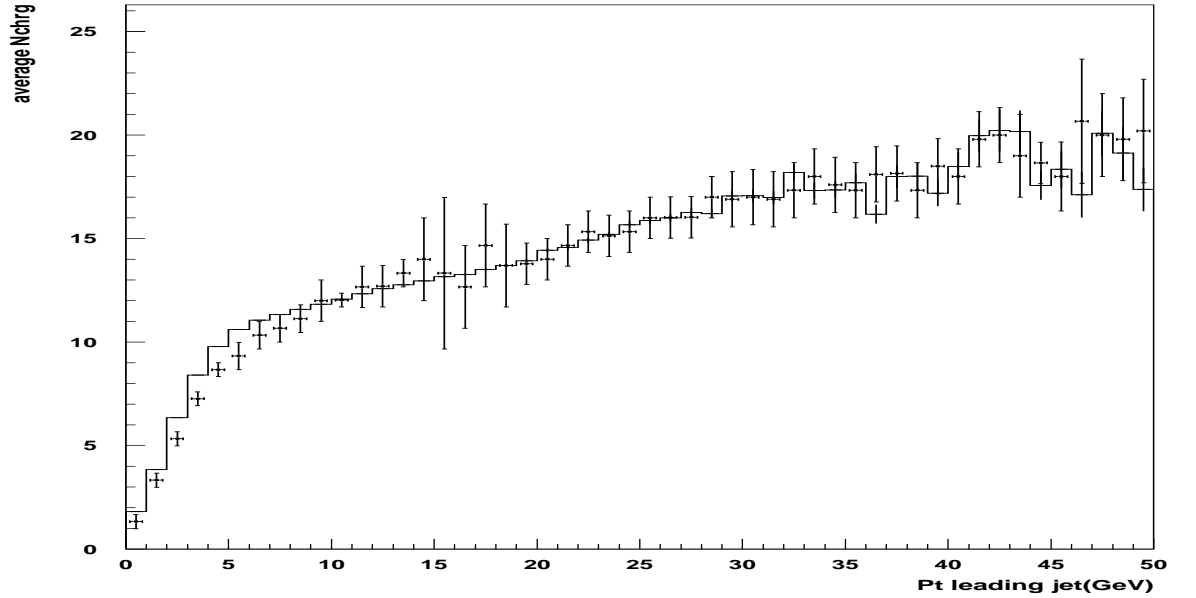

Figure 6.12: The average total number of charged particles in the event as a function of P_t (leading charged jet). HERWIG + Eikonal model, (solid line) simulated data ($p_{tmin} = 2.5$ GeV), experimental CDF data [35] (data points).
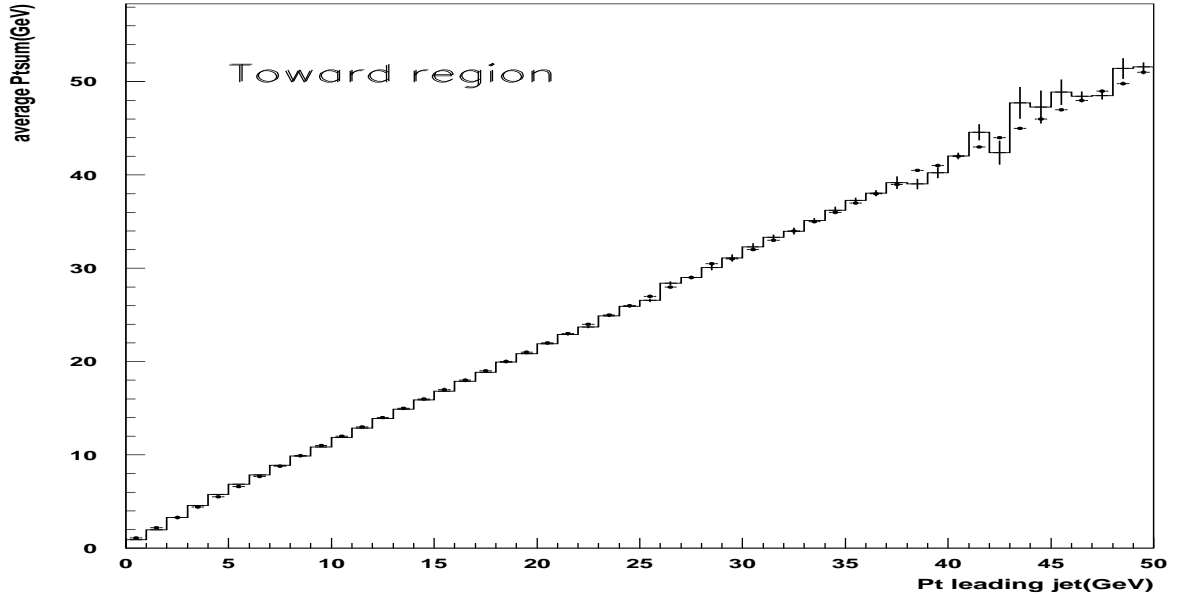
Figure 6.13: The average P_t sum of charged particles as a function of P_t (leading charged jet) in the toward region. HERWIG + Eikonal model (solid line) simulated data ($p_{tmin} = 2.5$ GeV), experimental CDF data [35] (data points).

Figure 6.14: The average P_t sum of charged particles as a function of P_t (leading charged jet) in the away region. HERWIG + Eikonal model (solid line) simulated data ($p_{tmin} = 2.5$ GeV), experimental CDF data [35] (data points).
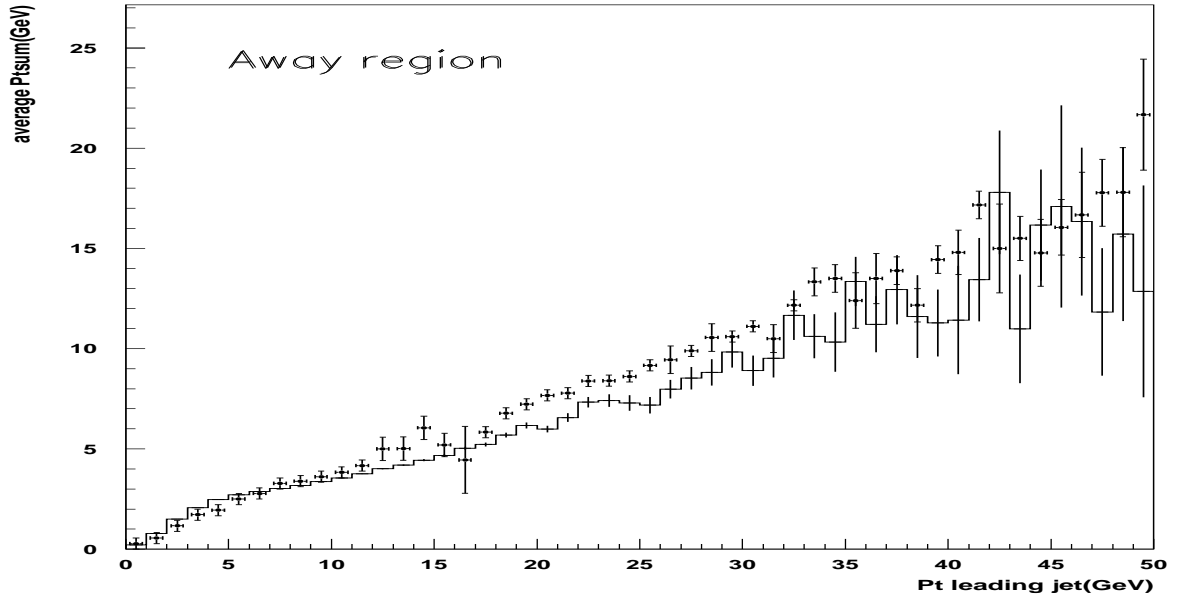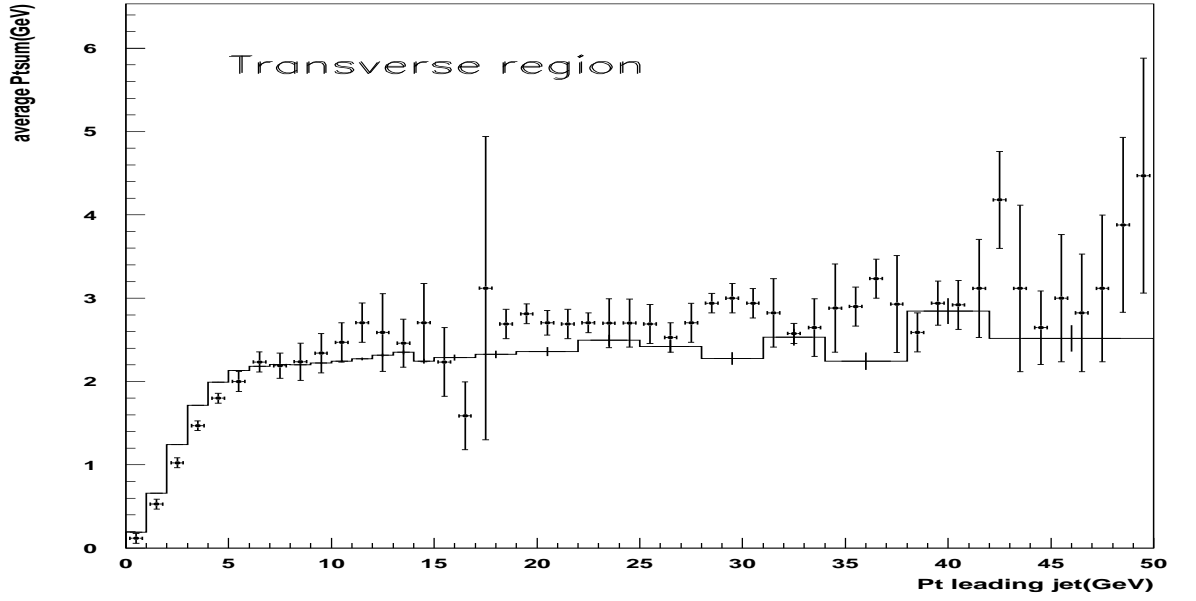
Figure 6.15: The average P_t sum of charged particles as a function of P_t (leading charged jet) in the transverse region. HERWIG + Eikonal model (solid line) simulated data (p_{tmin} = 2.5 GeV), experimental CDF data [35] solid circles.

Figure 6.16: The average number of charged particles as a function of P_t (leading charged jet) in the transverse region. HERWIG + Eikonal model (solid line) simulated data (p_{tmin} = 2.5 GeV), experimental CDF data [35] (data points).

Figure 6.17: The average P_t sum of charged particles as a function of P_t (leading charged jet) in the transverse region. HERWIG + Eikonal model (solid line), HERWIG + Underlying Event model (solid dashed), HERWIG + Multiparton Hard model (dotted), experimental CDF data [35] (data points).
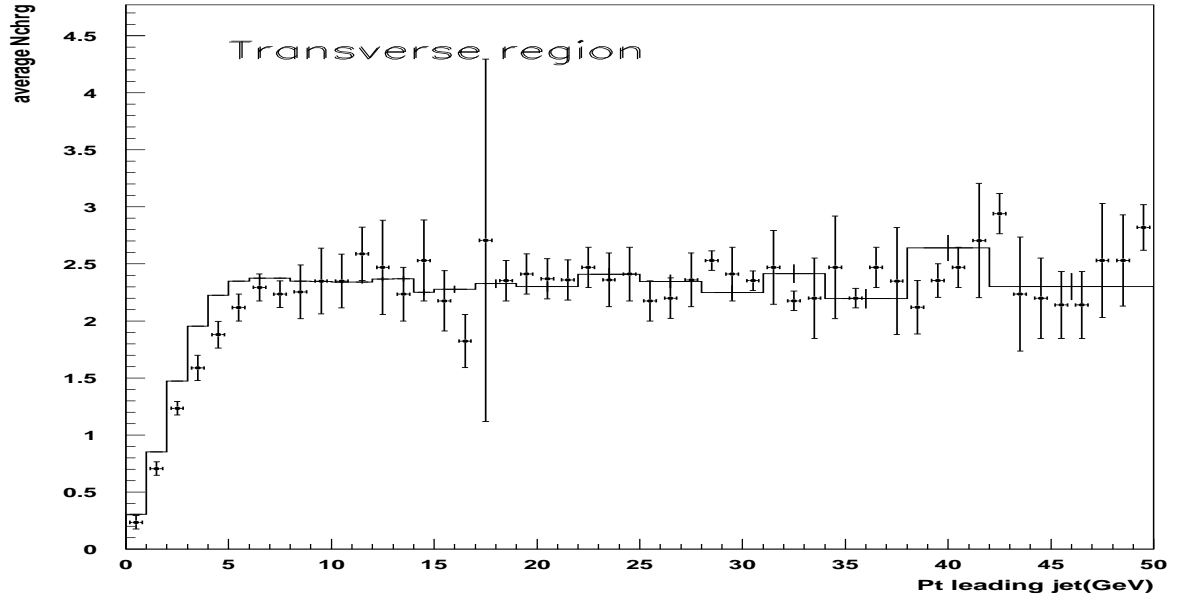
Figure 6.18: The average number of charged particles as a function of P_t (leading charged jet) in the transverse region. HERWIG + Eikonal model (solid line), HERWIG + Underlying Event model (solid dashed), HERWIG + Multiparton Hard model (dotted), experimental CDF data [35] (data points).
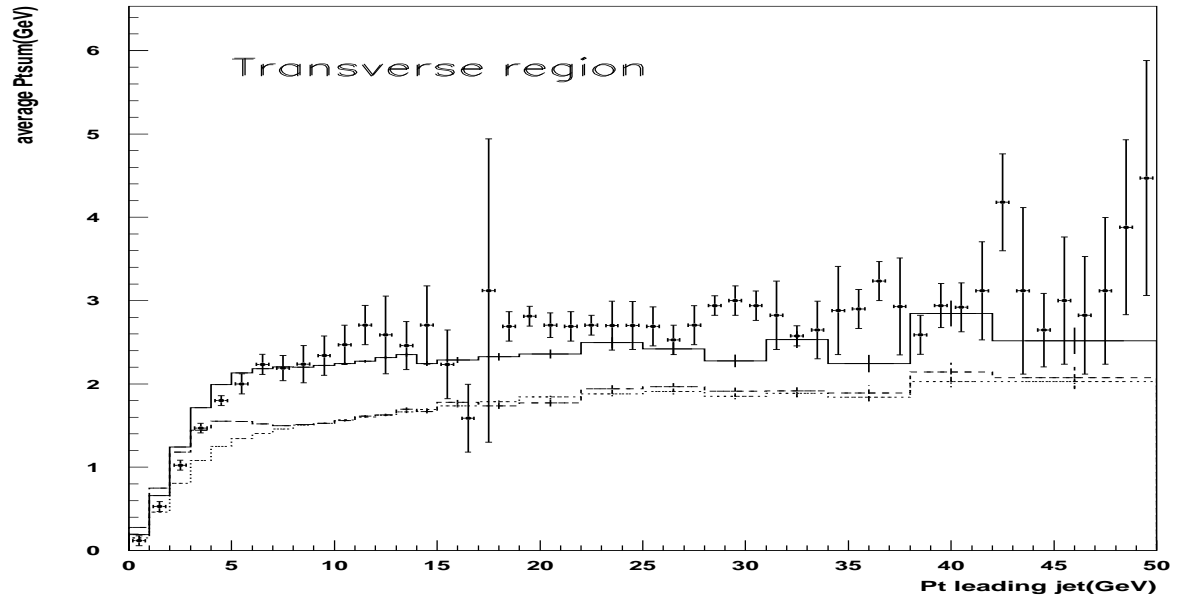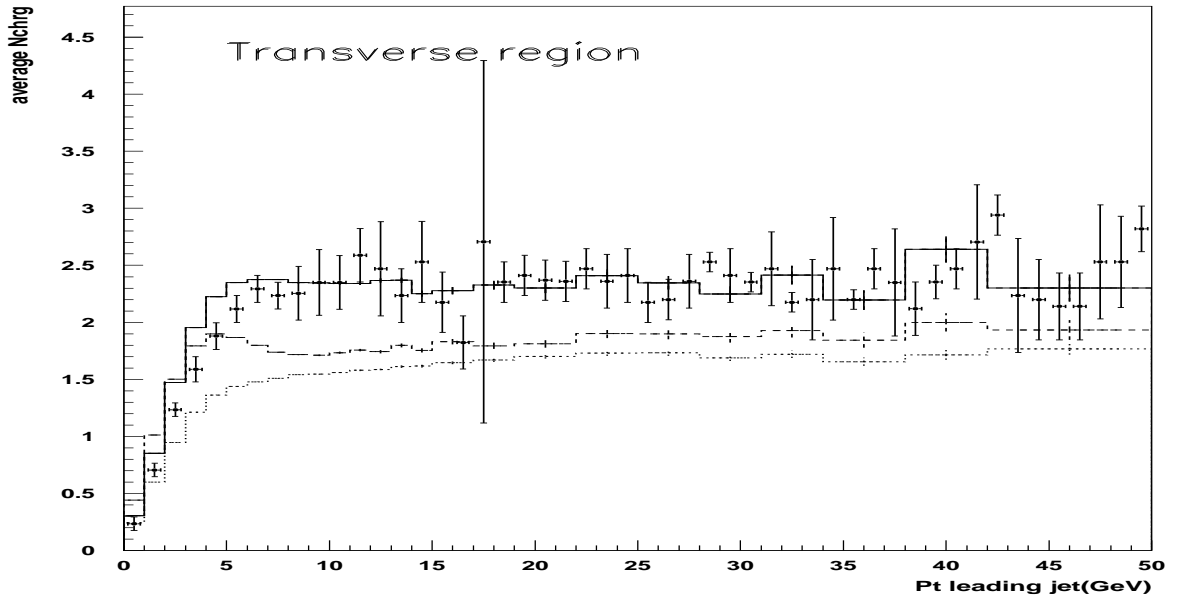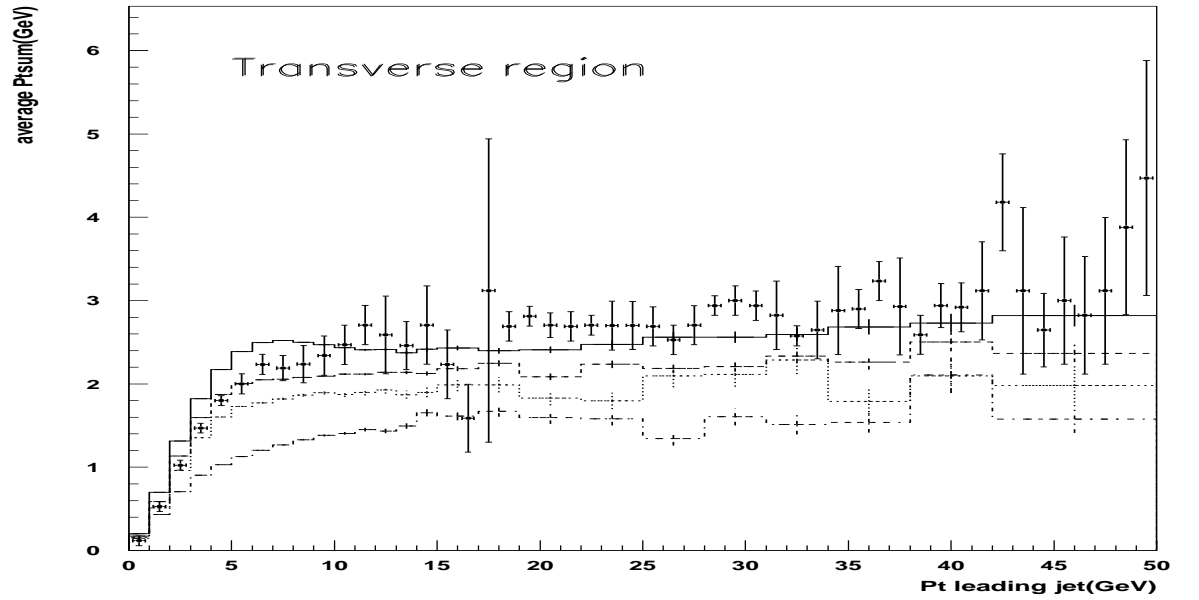
Figure 6.19: The average P_t sum of charged particles as a function of P_t (leading charged jet) in the transverse region. HERWIG + Eikonal Model for the two sets of $p_{tmin} = 3.0$ GeV (solid line) and 2.0 GeV (dashed), HERWIG + Multiparton Hard Model $p_{tmin} = 2.0$ GeV (dotted), $p_{tmin} = 3.0$ GeV (dotted dashed), experimental CDF data [35] (data points).

Figure 6.20: The average number of trans-Max and trans-Min charged particles as a function of P_t (leading charged jet) in the transverse region. Solid (Max) and hollow (Min) circles experimental CDF data [35], (solid line) simulated data.
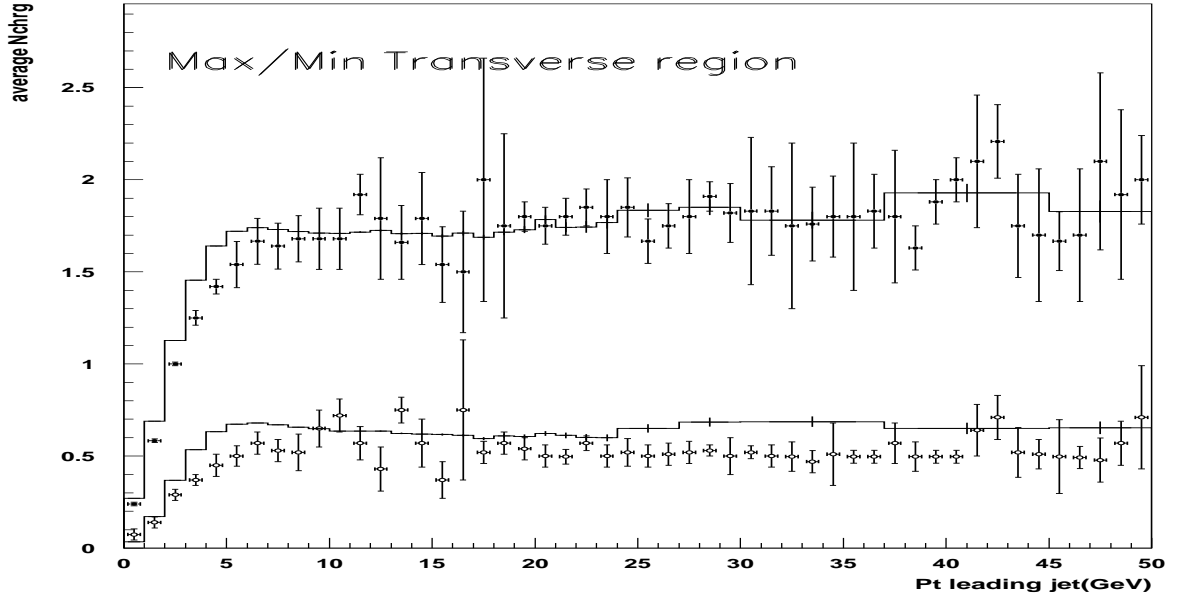

Figure 6.21: The average scalar P_t sum of the trans-Max and trans-Min charged particles as a function of P_t (leading charged jet) in the transverse region. Solid (Max) and hollow (Min) points are the experimental CDF data [35], (solid line) simulated data.
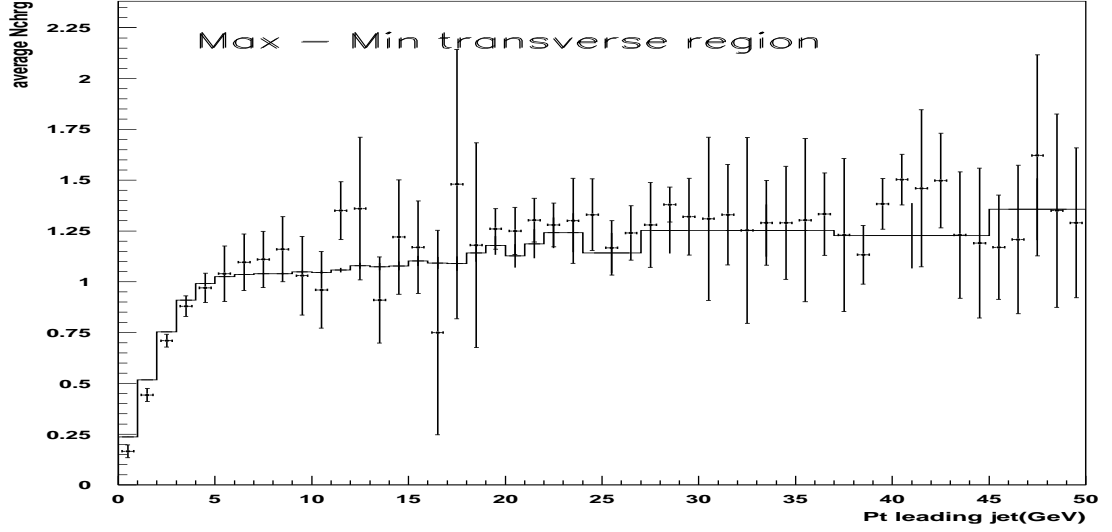
Figure 6.22: Data on the average difference, trans-Max minus trans-Min, for the number of charged particles as a function of P_t (leading charged jet) in the transverse region. Data points experimental CDF data [35], (solid line) simulated data.

6.5.2   UA1 and LHC data.

In this section we test the prediction of our model with data from the UA1 collaboration and give a prediction for the amount of underlying event that should be expected at the LHC. In our simulation of the UA1 data we closely follow the work presented in [39]. We simulate the pedestal transverse energy $\langle \omega_t^{ped} \rangle$ for a jet of given transverse energy E_t. The $\langle \omega_t^{ped} \rangle$ is the transverse-energy distribution $dE_t/d\eta$ integrated over the azimuthal angle ϕ on the same side of the jet axis $\mid \Delta\phi \mid \leq \pi/2$ and where $\Delta\eta$ is the difference in pseudo-rapidity with respect to the jet axis as shown in fig.6.25. The pedestal transverse energy is then defined as

$$\omega_t^{ped} = \frac{1}{2}(\omega_t^L + \omega_t^R) \tag{6.34}$$

where ω_t^L and ω_t^R are the transverse energy in the rapidity intervals $1 < \mid \Delta\eta \mid < 2$ on the two sides. The $\langle \omega_t^{ped} \rangle$ quantity is then the average transverse energy per unit rapidity measured in the region, 1.5 units of rapidity away from the jet axis. Integrating over
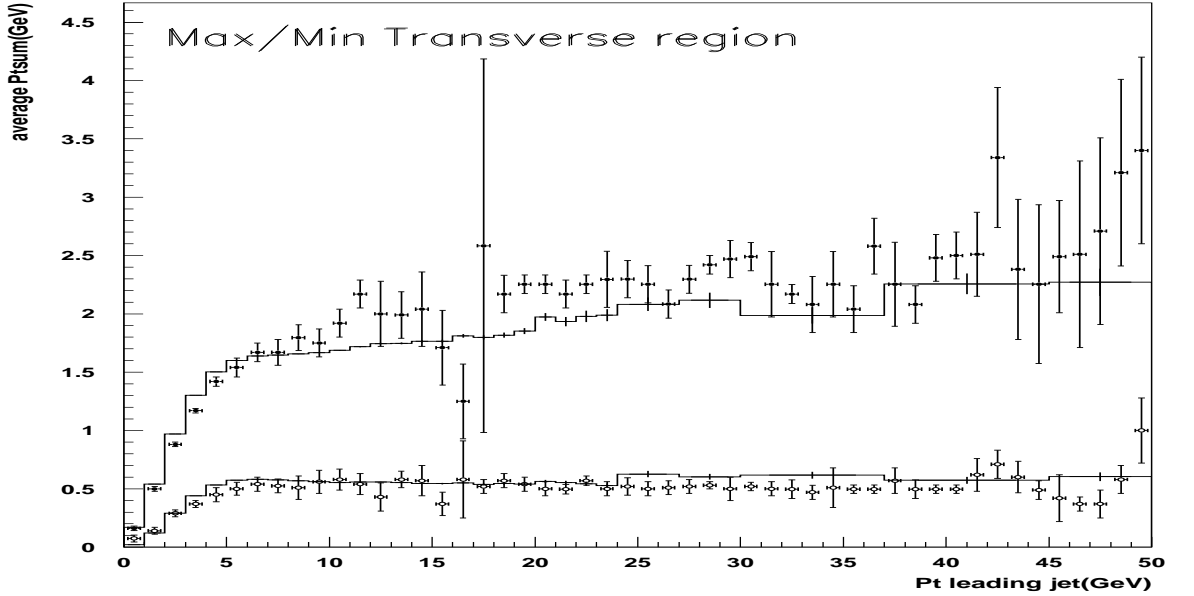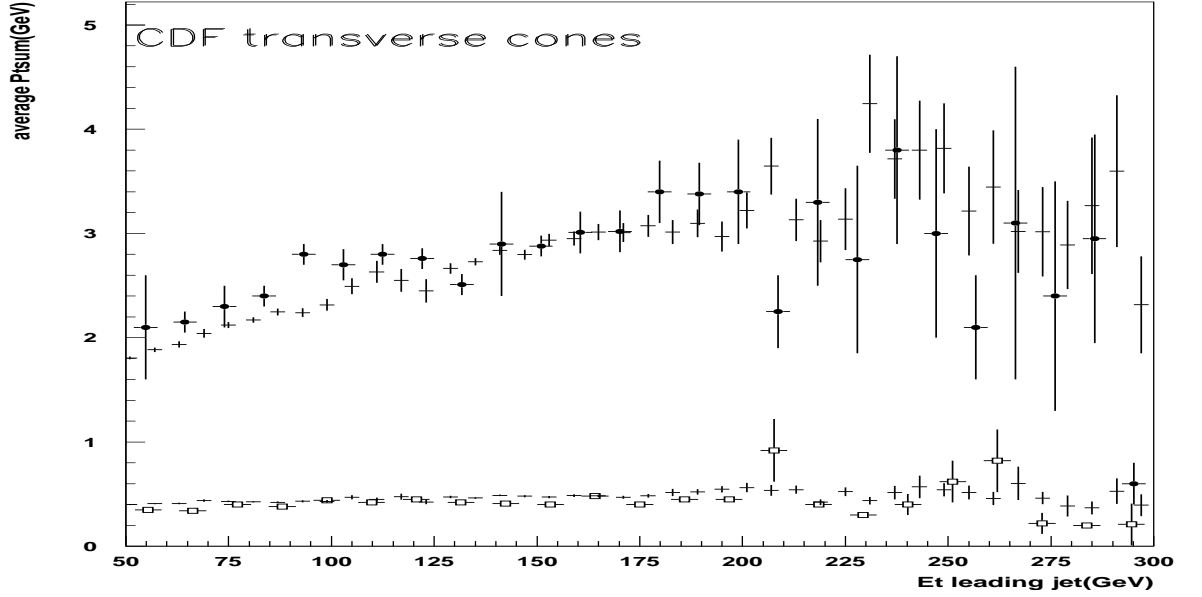
Figure 6.23: The average scalar P_t sum of the trans-Max and trans-Min charged particles as function of E_t (leading charged jet) in transverse cones. Solid (Max) and hollow (Min) circles experimental CDF data [35], HERWIG + Eikonal model (crosses) simulated data.

the azimuthal angle ϕ in the region ($\mid \Delta\phi \mid \leq \pi/2$) avoids contributions to $\langle \omega_t^{ped} \rangle$ from the recoiling jet. To construct jets in our simulation we have used the standard UA1 jet finding algorithm (including all final state particles, charged + neutral) with an opening angle $R = 1.0$. We point out that our simulation does not take into account details such as the detector effects. The jet algorithm searched for the cell with highest remaining E_t greater then 1.5 GeV, then formed a jet from this and all surrounding cells with $E_t > 0.5$ GeV within radius $R = 1.0$. The only phenomenological input to our model i.e. the total cross section ($\sigma_{tot} = 63.3$ mb) was calculated using eq.6.22. In fig.6.26 we show the agreement between simulated and experimental UA1 data at $\sqrt{s}$ = 630 GeV with $p_{tmin} = 2.5$ GeV. We point out (see fig.6.26) that the Eikonal model shows a better consistency with experimental data, as $\sqrt{s}$ is varied, than both the Hard Interaction model or HERWIG Soft Underlying Event model (i.e. if compared to CDF experimental data (see Section 4) since the Soft Underlying Event model was tuned to 546 GeV UA5 data [56]). We thus expect that if we are to consider eq.6.22
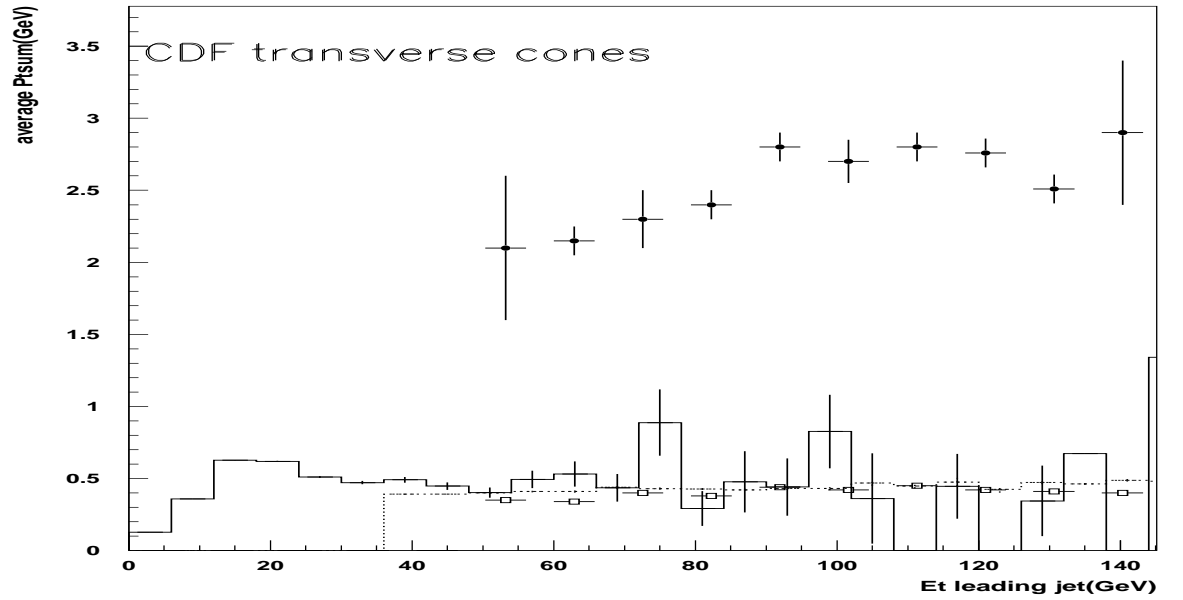
Figure 6.24: The average scalar P_t sum of the trans-Max and trans-Min charged particles as function of E_t (leading charged jet) in transverse cones. Solid (Max) and hollow (Min) circles experimental CDF data [35], HERWIG + Eikonal model $p_{tmin} = 3$ GeV (solid line), HERWIG + Eikonal model $p_{tmin} = 20, 40, 60, 80$ GeV (dashed line) simulated data.

at higher energies as correct we should predict the right amount of underlying event produced at the future LHC collider. In figs 6.27 - 6.31 we show that the underlying event activity (i.e. both the average number of charged particles and average scalar p_t sum in the transverse region) at $\sqrt{s} = 14$ TeV is expected to be roughly double that at $\sqrt{s} = 1.8$ TeV for jets with $p_t < 50$ GeV.

6.6   Conclusion

In this chapter we have introduced a new eikonal model for simulating particle production in hadron-hadron interactions. The goal of this model is to propose an alternative method to already existing ones to simulate remnant-remnant interactions in hard hadron-hadron and lepton-hadron interactions. Our new model is composed of two parts the perturbative hard multiparton interaction part and the non-perturbative interaction multiparticle soft part. The new Eikonal model implements a smooth transition between the soft and hard perturbative gluons' transverse momentum distributions in order to minimize the dependence of the model on its p_{tmin} parameter. The main constraint of the model is given by the total cross section which determines the amount of soft scatters in each collision. In this chapter we have shown a better consistency of the new Eikonal model with experimental data at $\sqrt{s} = 1800$ GeV and 630 GeV than that of the Hard Interaction model or HERWIG Soft Underlying Event model. We have also shown that the new Eikonal model is less dependent on the value of p_{tmin} than both of the above underlying event models. Finally we have given a prediction for the amount of underlying event activity that should be expected at the LHC. We believe that the model can still be improved by a better matching of the soft and hard part.
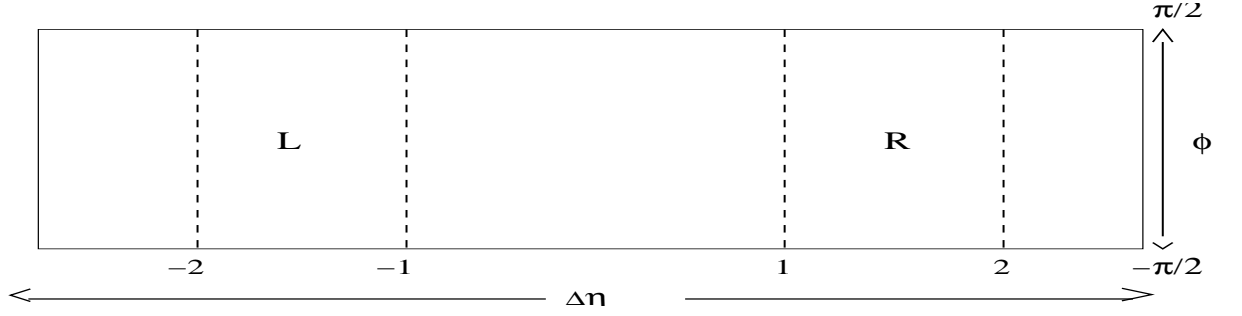
Figure 6.25: Illustration of the transverse regions in the η - ϕ space with $|\Delta\phi| \leq \pi/2$ in the rapidity intervals $1 < |\Delta\eta| < 2$ on the two sides (i.e. left (L) and right (R)).

Figure 6.26: Average transverse energy $\langle dE_t/d\eta \rangle$ in $1 \leq |\eta - \eta_{jet}| \leq 2$, $|\phi - \phi_{jet}| < \pi/2$ as a function of the E_{tjet} trigger. Data points UA1 at 630 GeV [39], solid line represents HERWIG + Eikonal model, dashed line represents HERWIG + Hard Interaction model (with reduced proton radius), dotted line represents HERWIG + Hard Interaction model with $p_{tmin}=2.0$ GeV.

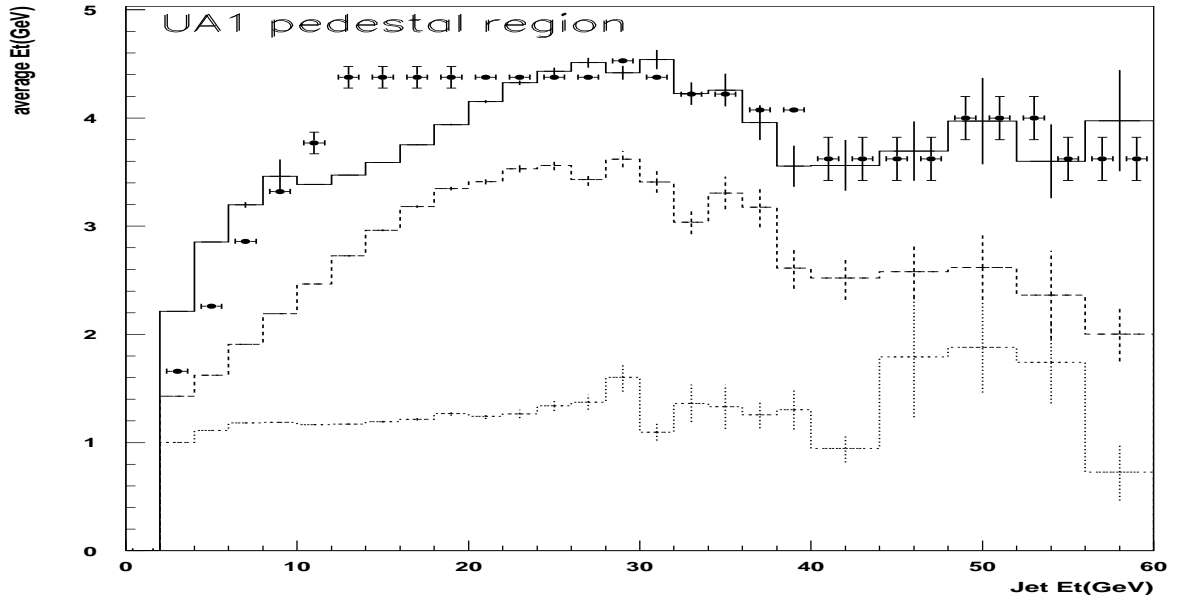Figure 6.27: The average P_t sum of charged particles as a function of P_t (leading charged jet) in the transverse region. HERWIG + Eikonal model at $\sqrt{s}$ = 14 TeV (solid line), HERWIG + Eikonal model at $\sqrt{s}$ = 1.8 TeV (dashed line).
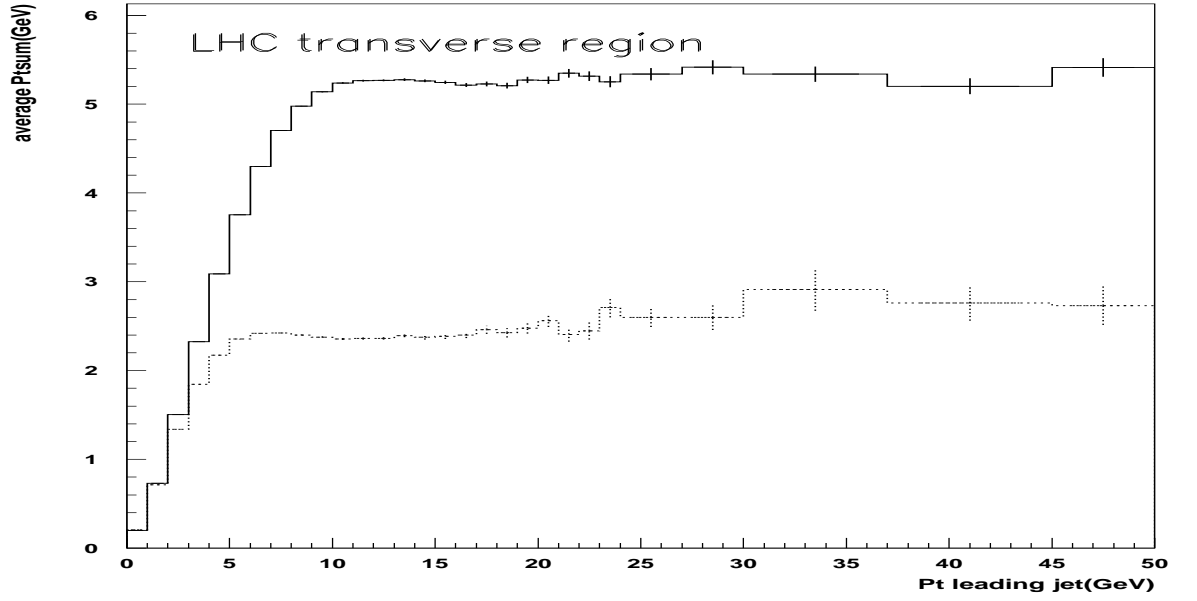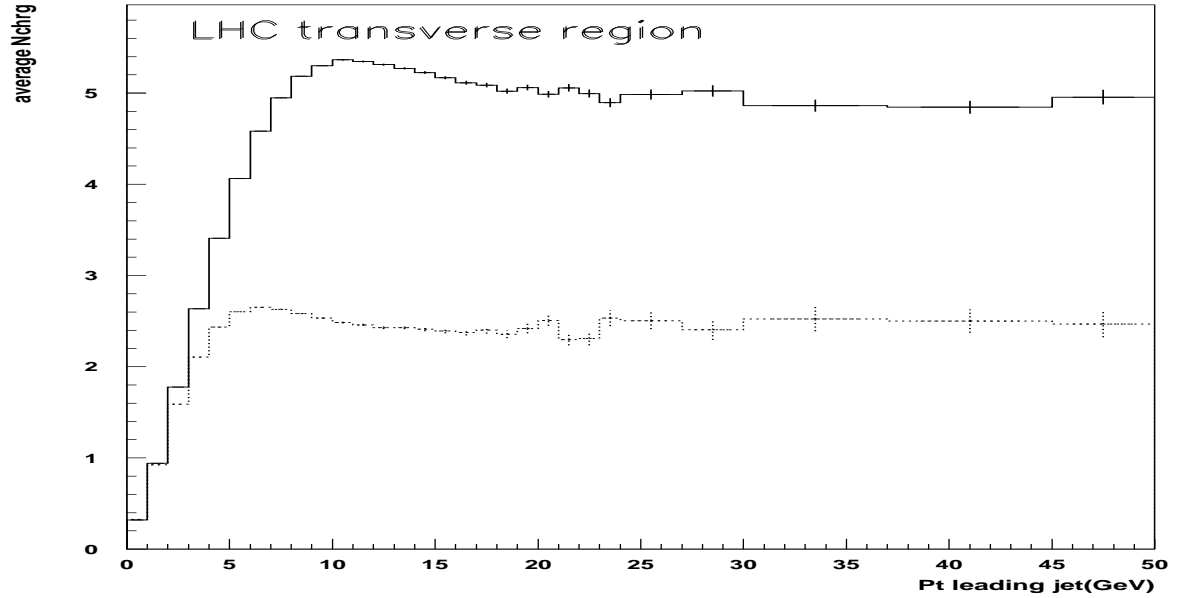

Figure 6.28: The average number of charged particles as a function of P_t (leading charged jet) in the transverse region. HERWIG + Eikonal model at $\sqrt{s}$ = 14 TeV (solid line), HERWIG + Eikonal model at $\sqrt{s}$ = 1.8 TeV (dashed line).
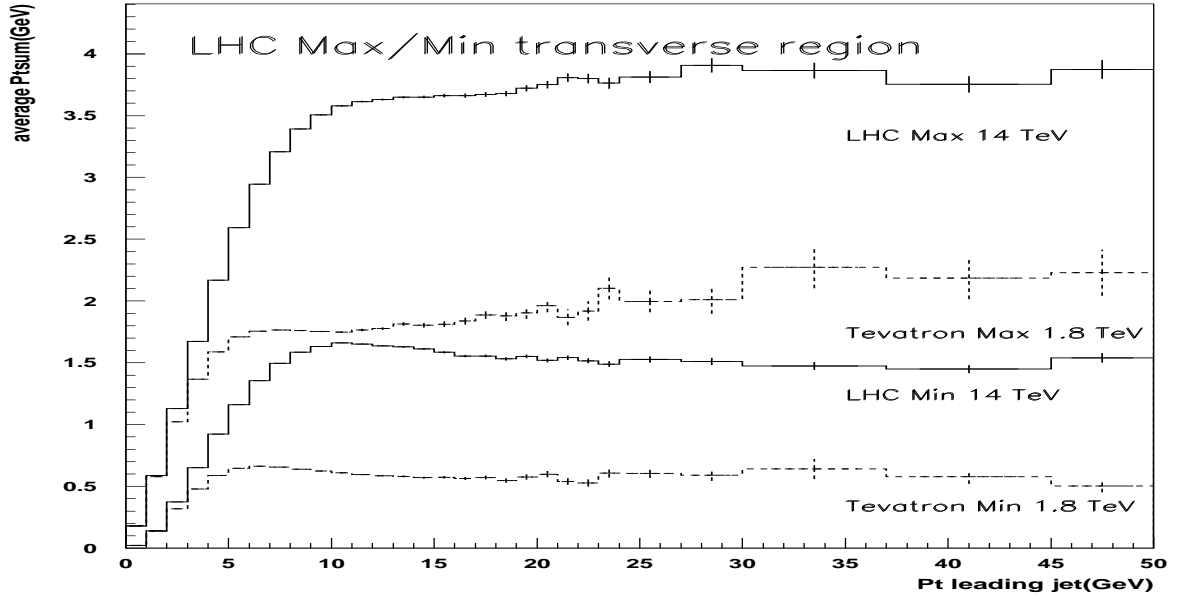
Figure 6.29: The average scalar P_t sum of the trans-Max and trans-Min charged particles as a function of P_t (leading charged jet) in the transverse region. HERWIG + Eikonal model at $\sqrt{s} = 14$ TeV (solid line), HERWIG + Eikonal model at $\sqrt{s} = 1.8$ TeV (dashed line).
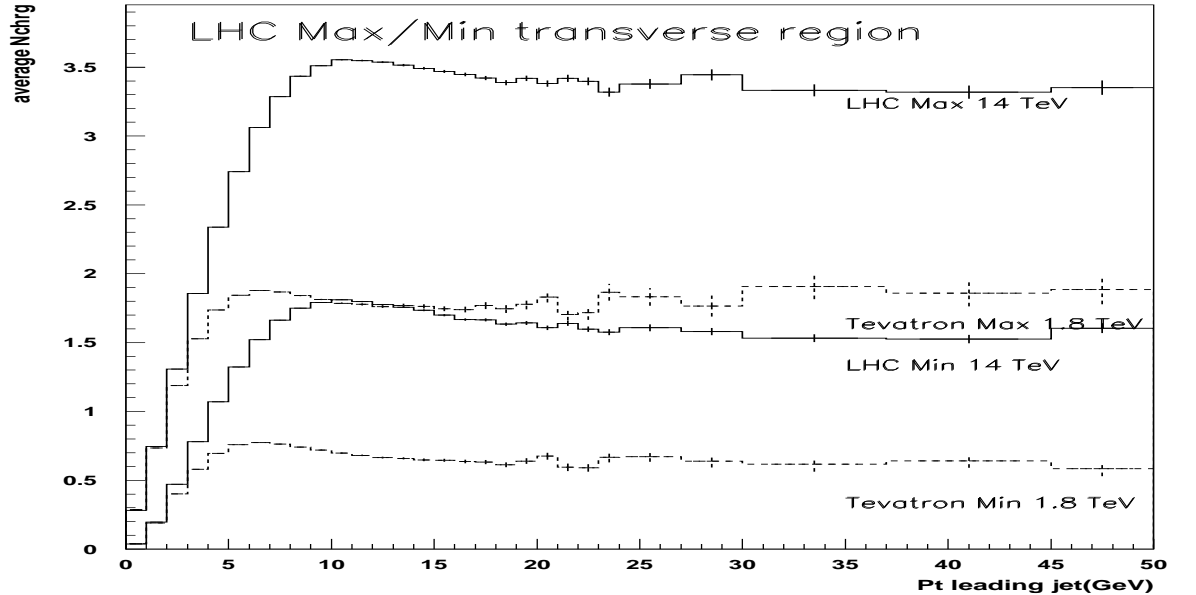
Figure 6.30: The average number of trans-Max and trans-Min charged particles as a function of P_t (leading charged jet) in the transverse region. HERWIG + Underlying Eikonal model at $\sqrt{s} = 14$ TeV (solid line), HERWIG + Eikonal model at $\sqrt{s} = 1.8$ TeV (dashed line).

Figure 6.31: Data on the average difference, trans-Max minus trans-Min, for the number of charged particles as a function of P_t (leading charged jet) in the transverse region. HERWIG + Eikonal model at $\sqrt{s} = 14$ TeV (solid line), HERWIG + Eikonal model at $\sqrt{s} = 1.8$ TeV (dashed line).
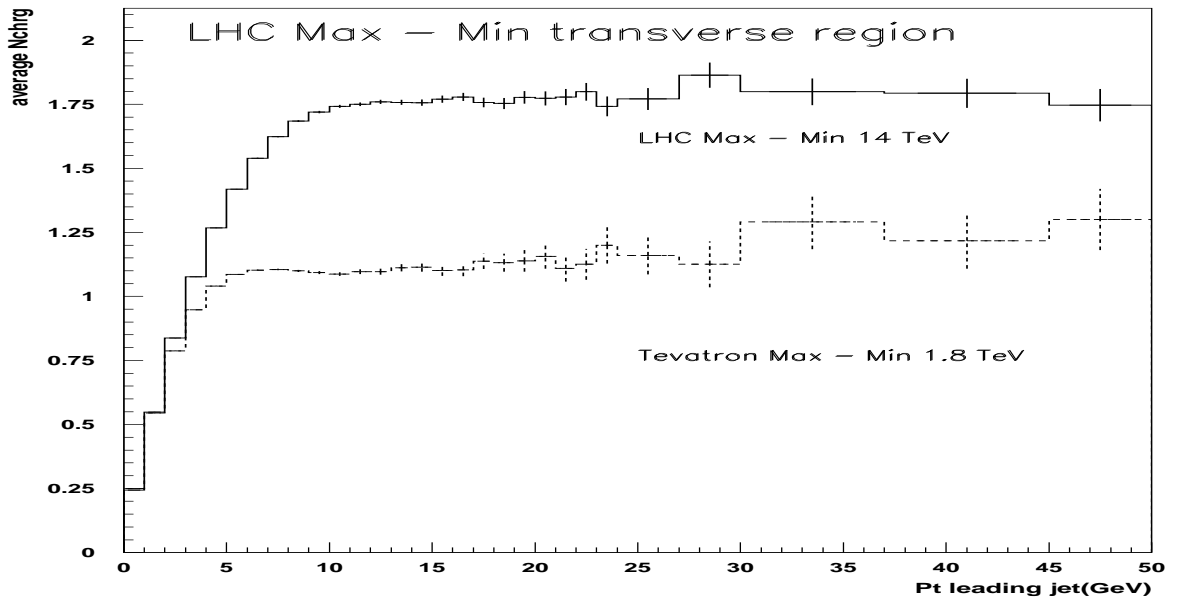
Chapter 7

Conclusions and future work

7.1 Conclusion

We have began this thesis by looking at the structure of the underlying event in proton-antiproton collisions at $\sqrt{s} = 1.8$ TeV. The underlying event is an interesting object not very well understood since it contains a mix of perturbative and non-perturbative physics. The two outgoing hard scattering partons from two to two hard parton-parton scattering form jets which receive additional contributions from initial and final state radiation and remnant-remnant interactions. Although the physics along the axis of the two outgoing jets seems to be well described by perturbative QCD (i.e. the hard part of interactions including initial and final state radiation) the region away from the jet axis is dominated by interactions of perturbative and non-perturbative nature which are not very well understood. These additional interactions also contribute to the energy underneath jets, which needs to be accounted for and subtracted from jet energies before they are compared to NLO QCD perturbative calculations. In order to simulate remnant-remnant interactions we have introduced a new Monte Carlo model, based on a simple eikonal model, for multiparticle production in hard proton-antiproton collisions. The new model contains two parts, the hard part, which was already implemented [42] (running in conjunction with HERWIG [19]), to which we have added a soft part, which uses HERWIG's showering and hadronisation models and allows us to extend our simulations to the non-perturbative soft region (i.e. particles with $0 \leq p_t \leq p_{tmin}$). One of our goals was to produce a simple new model (with a minimum number of parameters) which would be reasonably independent of the value chosen for the p_{tmin}. Furthermore, the eikonal multiparticle approach to hadron-hardon scattering is particularly interesting since it prevents the calculated cross sections from violating unitarity at high energies. Using a single phenomenological input to our model, namely the total cross section, we provide a good description of the measured data from [35] for low p_t jets with a reasonably small p_{tmin} dependence. We also provide a reasonable good description of data on the underlying event measured for higher p_t jets (see [41]). In addition we have shown that our new model gives a better prediction of the experimental data (CDF [35] and

UA1 [48]) than either the HERWIG + Underlying Event [19] or HERWIG + Hard Multiparton [42] model as the center of mass energy is varied from 1.8 TeV to 630 GeV. Finally we also provide a prediction for the amount of the underlying event which should be expected at the LHC. Although we are satisfied with the overall results of our model we point out that its efficiency needs to be improved particularly for the simulation of higher p_t jets by introducing two separate scales (i.e. one for controlling the amount of secondary scatters and another the scale of hard interactions) which for now are identical. We also believe that the invariance of our model to its p_{tmin} scale can be improved further by a better matching of the soft and hard scale.

References

[1] M. E. Peskin and D. V. Schroeder, *Reading, USA: Addison-Wesley (1995) 842 p.*

[2] R. K. Ellis, W. J. Stirling and B. R. Webber, "QCD and collider physics," *Cambridge, UK: Univ. Pr. (1996) 435 p. (Cambridge monographs on particle physics, nuclear physics and cosmology: 8).*

[3] R. G. Roberts, "The structure of the proton," *Cambridge, UK: Univ. Pr. (1990) 182 p. (Cambridge monographs on mathematical physics).*

[4] D. E. Groom *et al.*, Eur. Phys. J. **C15** (2000) 1.

[5] S. Bethke, J. Phys. G **G26** (2000) R27 [hep-ex/0004021].

[6] V. N. Gribov and L. N. Lipatov, Yad. Fiz. **15**, 781 (1972).

[7] L. N. Lipatov, Sov. J. Nucl. Phys. **20**, 94 (1975).

[8] G. Altarelli and G. Parisi, Nucl. Phys. **B126**, 298 (1977).

[9] Yu. L. Dokshitzer, Sov. Phys. JETP **46** (1977) 641.

[10] A. D. Martin, W. J. Stirling and R. G. Roberts, Phys. Rev. D **50**, 6734 (1994) [arXiv:hep-ph/9406315].

[11] A. D. Martin, R. G. Roberts, W. J. Stirling and R. S. Thorne, Eur. Phys. J. **C4** (1998) 463 [hep-ph/9803445].

[12] P. D. Collins, "An Introduction To Regge Theory And High-Energy Physics," *Cambridge 1977, 445p.*

[13] A. V. Barnes *et al.*, Phys. Rev. Lett. **37** (1976) 76.

[14] J. R. Forshaw and D. A. Ross, "Quantum chromodynamics and the pomeron," *Cambridge, UK: Univ. Pr. (1997) 248 p. (Cambridge lecture notes in physics. 9)*.

[15] A. Donnachie and P. V. Landshoff, Phys. Lett. **B296** (1992) 227 [hep-ph/9209205].

[16] M. Froissart, Phys. Rev. **123** (1961) 1053.

[17] F. James, Rept. Prog. Phys. **43**, 1145 (1980).

[18] F. James, Comput. Phys. Commun. **60**, 329 (1990).

[19] G. Marchesini, B. R. Webber, G. Abbiendi, I. G. Knowles, M. H. Seymour and L. Stanco, Comput. Phys. Commun. **67**, 465 (1992).

[20] F. James, Ann. Rev. Nucl. Part. Sci. **37**, 383 (1990).

[21] B. L. Combridge, J. Kripfganz and J. Ranft, Phys. Lett. B **70**, 234 (1977).

[22] D. W. Duke and J. F. Owens, Phys. Rev. D **26**, 1600 (1982).

[23] G. Marchesini and B. R. Webber, Nucl. Phys. B **238**, 1 (1984).

[24] B. R. Webber, Nucl. Phys. B **238**, 492 (1984).

[25] G. Marchesini and B. R. Webber, Nucl. Phys. B **310**, 461 (1988).

[26] V. V. Sudakov, Sov. Phys. JETP **3**, 65 (1956) [Zh. Eksp. Teor. Fiz. **30**, 87 (1956)].

[27] A. Bassetto, M. Ciafaloni and G. Marchesini, Phys. Rept. **100**, 201 (1983).

[28] Yu. L. Dokshitzer, V. A. Khoze, S. I. Troian and A. H. Mueller, Rev. Mod. Phys. **60**, 373 (1988).

[29] R. K. Ellis, G. Marchesini and B. R. Webber, Nucl. Phys. B **286**, 643 (1987) [Erratum-ibid. B **294**, 1180 (1987)].

[30] T. Sjostrand, Phys. Lett. B **157**, 321 (1985).

[31] D. Amati and G. Veneziano, Phys. Lett. B **83**, 87 (1979).

[32] Y. I. Azimov, Yu. L. Dokshitzer, V. A. Khoze and S. I. Troian, Phys. Lett. B **165** (1985) 147.

[33] M. H. Seymour Ph.D Thesis.

[34] G. J. Alner *et al.* [UA5 Collaboration], Nucl. Phys. B **291**, 445 (1987).

[35] T. Affolder *et al.* [CDF Collaboration], Phys. Rev. D **65**, 092002 (2002); R. D. Field, arXiv:hep-ph/0201192.

[36] B. Abbott *et al.* [D0 Collaboration], Nucl. Instrum. Meth. A **424**, 352 (1999) [arXiv:hep-ex/9805009].

[37] J. Huth *et al.*, In proceedings of Research Directions for the Decade, Snowmass 1990, Editor E. L. Berger, (World Scientific, Singapour, 1992).

[38] M. H. Seymour, Nucl. Phys. B **513**, 269 (1998) [arXiv:hep-ph/9707338].

[39] G. Marchesini and B. R. Webber, Phys. Rev. D **38**, 3419 (1988).

[40] J. Pumplin, Phys. Rev. D **57**, 5787 (1998) [arXiv:hep-ph/9708464].

[41] V. Tano, arXiv:hep-ex/0205023.

[42] J. M. Butterworth, J. R. Forshaw and M. H. Seymour, Z. Phys. C **72**, 637 (1996) [arXiv:hep-ph/9601371].

[43] T. Sjostrand and M. van Zijl, Phys. Rev. D **36**, 2019 (1987); T. Sjostrand, Phys. Lett. **B157**, 321 (1985); M. Bengtsson, T. Sjostrand and M. van Zijl, Z. Phys. **C32**, 67 (1986).

[44] F. Abe *et al.* [CDF Collaboration], Phys. Rev. D **56**, 3811 (1997).

[45] F. Abe *et al.* [CDF Collaboration], Phys. Rev. Lett. **79**, 584 (1997).

[46] T. Akesson *et al.* [Axial Field Spectrometer Collaboration], Z. Phys. C **34**, 163 (1987).

[47] J. Alitti *et al.* [UA2 Collaboration], Phys. Lett. B **268**, 145 (1991).

[48] C. Albajar *et al.* [UA1 Collaboration], Jets," Nucl. Phys. B **309**, 405 (1988).

[49] J. C. Collins and G. A. Ladinsky, Phys. Rev. D **43**, 2847 (1991).

[50] J. R. Forshaw and J. K. Storrow, Phys. Lett. B **268**, 116 (1991) [Erratum-ibid. B **276**, 565 (1992)].

[51] R. S. Fletcher, T. K. Gaisser and F. Halzen, Phys. Rev. D **45**, 377 (1992) [Erratum-ibid. D **45**, 3279 (1992)].

[52] L. Durand and P. Hong, Phys. Rev. Lett. **58** 303 (1987).

[53] I. Borozan and M. H. Seymour, JHEP **0209** (2002) 015 [arXiv:hep-ph/0207283].

[54] F. Abe *et al.* [CDF Collaboration], Phys. Rev. D **50**, 5550 (1994).

[55] T. T. Chou and C. N. Yang, Phys. Rev. **170** 1591 (1968).

[56] G. J. Alner *et al.* [UA5 Collaboration], Phys. Rept. **154**, 247 (1987).

[57] R. Engel, Z. Phys. C **66** 203 (1995); and private communication.